UNIVERSITÉ DE SHERBROOKE
Faculté de Lettres et de Sciences humaines
Département de Géomatique Appliquée

ACCURACY IN STARPHOTOMETRY

Liviu Ivănescu

Thesis submitted in partial fulfilment of the requirements for the degree of philosophiæ doctor (Ph.D.) in physics of the remote sensing

April 2020
Sherbrooke, Québec, Canada

JURY

Supervisor: Prof. Norman T. O'Neill

Internal Member: Prof. Yannick Huot

Internal Member: Adj. Prof. Martin Aubé

External Member: Prof. Gilles Couture, UQAM

Sommaire

La photométrie ou spectrophotométrie stellaire, est une méthode de télédétection passive pour mesurer l'épaisseur optique spectrale de l'atmosphère. Ceci est accompli en comparant le signal mesuré avec le rayonnement extra-atmosphérique d'une étoile de référence. La photométrie stellaire a été introduite au début des années 1980 [1, 17], en tant que contrepartie nocturne de la photométrie solaire [6] afin d'obtenir une surveillance continuelle sur 24 h de l'épaisseur optique des aérosols. Malgré toutes les avancées technologiques, une photométrie stellaire robuste, avec exactitude de mesure, reste un défi [5, 2], qui a limité son évolution.

L'objectif général de ce travail est de susciter la confiance et l'intérêt pour la photométrie stellaire en améliorant sa fiabilité, son exactitude de mesure et en identifiant les cas particuliers où elle surpasse la photométrie solaire (qui est en fait une photométrie stellaire dont l'étoile est notre Soleil). Pour atteindre cet objectif, nous devons mieux comprendre, en détails, la nature des attributs spécifiques de la photométrie stellaire: les différentes classes spectrales des étoiles, les propriétés des sources de référence plus faibles, les conséquences d'une plus grande ouverture de télescope, un champ de vision (en anglais, Field Of View - FOV) moindre etc.

L'amélioration de la fiabilité de la photométrie stellaire (qui est ultimement associée à son taux de collecte de données) devrait être abordée à la fois par des améliorations matérielles, ainsi que par des meilleures stratégies d'observation pour atténuer les défis environnementaux. L'exactitude de mesure de l'épaisseur optique reste critique pour certaines méthodes d'extraction de caractéristiques de particules, qui nécessitent une erreur d'épaisseur optique inférieure à 0.01 [14], ou une erreur photométrique équivalente de 1%. Bien qu'une telle cible soit généralement atteinte en photométrie solaire [18], elle représente toujours un défi en photométrie

stellaire. Afin de répondre à une telle exigence d'exactitude, il est essentiel d'identifier toutes les principales sources d'erreurs, de faciliter la quantification de l'exactitude et, éventuellement, d'atténuer les divers mécanismes d'erreur.

Un avantage clé de la photométrie stellaire, en plus de fournir des observations nocturnes en complément à la photométrie solaire, est son efficacité d'observation de 100% en présence de ciel clair. En revanche, l'autre alternative d'observation nocturne, la photométrie lunaire [4], est limitée à une efficacité de 50% (soit, entre le premier et le dernier quart de lune). La photométrie stellaire est particulièrement pertinente près des pôles, pendant la longue nuit polaire. Elle permet des mesures scientifiques à partir d'une région et durant une période pour laquelle on dispose généralement de très peu d'informations. A part cela, la disponibilité de nombreuses sources stellaires garantit l'acquisition d'observations dans presque toutes les directions. Cela facilite l'acquisition synergétique de données provenant d'autres instruments: les exemples clés incluent les lidars terrestres (généralement orientés vers zénith) ([8], les lidars satellitaires, tels que CALIOP pointant vers nadir, à bord du satellite CALIPSO [11] et le lidar Doppler ALADIN à pointage oblique, à bord de l'ADM-Aeolus [7]. De plus, étant donné que la diffusion frontale dans le cas des FOV larges des photomètres solaires et des photomètres lunaires peut induire une sous-estimation importante de l'épaisseur optique [12], les FOV significativement moindre des photomètres stellaires garantissent un avantage distinct de la photométrie stellaire à cet égard.

Un aspect important de l'objectif du projet est d'identifier et quantifier des sources inconnues d'erreurs d'exactitude. Un attribut particulièrement frustrant de la photométrie stellaire est que même les erreurs connues sont difficiles à estimer. En fait, même si elles sont estimées par comparaison avec d'autres instruments (lidars, d'autres photomètres stellaires ou lunaires), ces erreurs peuvent également varier en fonction de différentes conditions d'observation. Le niveau de confiance dans ces systèmes reste par conséquent faible. Si l'utilisation de masse est un avantage pour la maturation des instruments, alors la photométrie stellaire est désavantagée: il n'y a actuellement que 2–3 photomètres stellaires opérationnels dans le monde. En outre, le degré plus élevé de complexité technique et le taux de panne par rapport aux photomètres solaires et lunaires, leurs exigences élevées en matière de maintenance et de dépannage, peuvent les rendre peu attrayants pour les observatoires opérationnels.

Sommaire

En raison de la faible demande de photomètres stellaires qui en résulte, Dr. Schulz & Partner GmbH (la seule entreprise fabriquant des photomètres stellaires en série) a cessé ses activités avant de pouvoir résoudre correctement certains des problèmes techniques identifiés par les utilisateurs (par exemple, surchauffe interne, revêtement antireflet inapproprié de lentilles, accès indisponible à certains paramètres critiques etc.). Cela conduit à un cycle de méfiance: il faut de nombreuses observations et études pour améliorer la fiabilité et l'exactitude, alors que nous n'avons pas assez d'instruments opérationnels en raison de leurs problèmes techniques et de leur exactitude discutable.

Les photomètres stellaires ont également leur lot de défis spécifiques reliés au site d'observation. Un problème courant est le dépôt de poussière, de rosée, de givre ou de particules de glace sur le télescope (avec des effets associés sur l'atténuation optique). Un site polaire, comme Eureka, pose plusieurs défis supplémentaires: turbulence de l'air plus élevée près du niveau de la mer (avec des effets sur la taille de l'image de l'étoile), scintillation plus élevée à grande masse d'air (affectant la précision de la mesure), température ambiante très basse (affectant le matériel, notamment les pièces mécaniques en mouvement et le câblage électrique), le pergélisol (empêchant une bonne mise à la terre électrique), le bien-être des instruments à proximité (sensibles aux interférences électromagnétiques, ou EMI), l'emplacement en région éloignée (ce qui signifie de longs retards dans l'expédition des pièces pour les réparations), air très sec (dégazage de composants électroniques), assistance limitée sur le site (pour l'opération et la maintenance), accessibilité dangereuse (environnement non-protégé contre les animaux sauvages: loups, bœufs musqués, ours polaires), internet très lent (pour le transfert de données ou l'opération à distance). Nos photomètres stellaires ont subi plusieurs pannes matérielles, chaque année au cours de leurs 11 années de fonctionnement. Cela a entraîné un risque élevé de ne pas pouvoir terminer les études prévues en temps opportun. Nous décrivons ici nos contributions techniques et scientifiques issues du projet de thèse.

Article 1: Bien que cet article initial ait été rigoureusement examiné en vue de publication par le comité des SPIE Proceedings, il n'était néanmoins pas ciblé comme un article scientifique évalué par les pairs, mais plutôt comme une introduction à la photométrie stellaire arctique et à ses défis techniques. Il décrit en détail les

développements que nous avons faits pour surmonter les principaux problèmes techniques et logistiques liés à l'exploitation d'un photomètre stellaire dans un endroit éloigné et à environnement hostile, tel qu'Eureka. Réussir dans ce cas extrême pourrait, espérons-le, fournir la confiance nécessaire dans la fiabilité de la photométrie stellaire. Ces travaux ont notamment identifié: les problèmes de mise à la terre électrique dus au pergélisol, le dégazage dû à l'air sec, les problèmes de débit optique dus au revêtement des lentilles, le problème majeur du dépôt de cristaux omniprésent sur le télescope et la nécessité d'une opération à distance. Pour plus d'informations, l'article est présenté au Chapitre 1.

Article 2: Le deuxième article est le principal travail scientifique de télédétection de la thèse, dans la mesure où ils partagent le même titre. Dans le Chapitre 2, il développe en détail le cadre théorique de la photométrie stellaire, conduisant à l'identification de tous les paramètres susceptibles d'induire des erreurs importantes. Il identifie en particulier l'avantage d'effectuer un étalonnage indépendant de l'étoile, mais néanmoins dépendant de l'instrument. Ensuite, il explore en profondeur et, espérons-le, identifie les principales sources d'erreurs d'exactitude spécifiques à la photométrie stellaire et fournit des solutions d'atténuation. Une investigation aussi approfondie, particulièrement impliquant un site éloigné de l'Arctique, nécessitait beaucoup de ressources matérielles et intellectuelles. Bien que j'aie effectué tout le travail décrit dans l'article, au-delà des précieuses contributions de mes collègues coauteurs, les conseils constants, les contre-vérifications scientifiques rigoureuses et la vérification approfondie du texte par mon superviseur ont été déterminants. Enfin, la disponibilité constante pour assurer la maintenance, par les fabricants du photomètre stellaire, du dôme et de la monture de télescope, a été primordiale.

Article 3: Alors que nous travaillons simultanément sur une analyse complète des procédures d'étalonnage, la courte communication présentée au Chapitre 3 vise à atteindre plus rapidement la communauté scientifique en soulignant qu'un étalonnage multi-étoiles, indépendant d'étoile, peut être effectué sur place, même près du niveau de la mer. On y commence par présenter statistiquement les périodes de ciel clair typiques pour Eureka. Ensuite, on souligne la rapidité de l'étalonnage multi-étoiles, évitant des variations importantes de transparence du ciel et lissant certaines des inexactitudes du catalogue extra-atmosphérique de magnitudes d'étoiles. La possi-

bilité d'un tel étalonnage multi-étoiles n'apparaît qu'à la suite de l'accent mis sur l'utilisation d'un étalonnage indépendant d'étoile dans l'article 2. De plus, il est démontré qu'une méthode d'étalonnage particulière, appelée « inverse », réduit davantage les erreurs d'étalonnage, approchant notre cible d'exactitude. Cet objectif principal est confirmé par une analyse de répétabilité.

Bien que d'importants développements en photométrie stellaire aient été réalisés au cours de la dernière décennie, principalement par Perez-Ramirez [16, 15], une analyse complète des erreurs d'exactitude n'a pas été effectuée depuis les travaux de Young [19] dans les années 1970, dans le contexte de l'astronomie professionnelle. Notre travail le met à jour et le complète avec la réalité technologique actuelle et la spécificité de la photométrie stellaire pour la télédétection atmosphérique. Cela nous a permis d'évaluer quantitativement les principales sources d'erreurs et de songer comment y remédier. Parmi nos trouvailles originales sont les lignes gênantes d'absorption d'O_4, jusqu'à présent non considérées dans le contexte de la photométrie stellaire. Elles empêchent une élimination exacte de la bande d'ozone, conduisant à une distorsion du spectre d'aérosol déduit. Nous avons identifié un FOV de 45″, optimisé pour une utilisation en photométrie stellaire, comme compromis pour préserver le débit optique, ainsi que limiter les erreurs de diffusion frontale lors de l'observation des nuages. On a également identifié pour la première fois l'avantage de la photométrie stellaire par rapport à la photométrie solaire dans un tel contexte. Nous avons souligné pour la première fois l'importance de l'utilisation de classes spectrales des étoiles froides (par exemple, la classe F) lors de l'observation des nuages, et généralement l'utilisation des étoiles B précoces ou A tardives quand une meilleure exactitude est requise. Le dépôt de cristaux sur la fenêtre d'entrée du télescope dans l'Arctique a longtemps semblé être un gros et insurmontable problème. Après plusieurs essais, nous avons identifié l'utilisation d'une bande chauffante autour du télescope, en tant que solution efficace dans la plupart des situations environnementales. Toutes ces améliorations suggèrent que l'atteinte de la cible d'exactitude de 1% pourrait devenir enfin possible. De plus, notre mise en œuvre de l'opération et de la maintenance à distance, pouvant être effectuée même à partir d'un téléphone intelligent, c'est-à-dire à tout moment et de n'importe où dans le monde, est unique au moins dans la communauté de photométrie stellaire. Cela ouvre enfin, pour la première fois, la possibilité de gagner la confiance

dans ce type d'instruments.

Une telle analyse approfondie aurait plutôt dû être élaborée par des efforts concertés de la communauté scientifique, sur plusieurs sites. La disponibilité limitée de photomètres stellaires opérationnels et la nécessité aiguë de briser le cercle de méfiance nous ont amenés à y faire face dans toute sa complexité. Cependant, le fait que nous ayons principalement basé notre analyse sur un seul type de photomètres stellaires et principalement sur la spécificité d'un seul observatoire au niveau de la mer en Arctique, peut conduire à passer à côté de certaines sources potentielles d'erreurs spécifiques à d'autres sites. On peut supposer, par exemple, des problèmes liés à l'humidité dans les tropiques, le dépôt de poussière dans les environnements arides ou l'estimation erronée de la brillance de fond de ciel dans les sites fortement pollués par la lumière, comme les villes. Au-delà de celles-ci, il est également possible que nous ayons négligé certaines erreurs importantes, car nous avons continuellement, et parfois de manière inattendue dans des situations spécifiques, révélé leur grande ampleur. Nous recommandons alors que, pour valider les résultats identifiés ici, on devrait régulièrement participer à des campagnes d'observation sur d'autres sites et comparer l'exactitude attendue avec d'autres instruments colocalisés.

En plus de ce travail, nous sommes également très avancés dans la finalisation d'une analyse complète des erreurs de photométrie stellaire non systématiques, de précision. Ces résultats servent ensuite à développer une analyse complète des méthodes d'étalonnage (ultimement, affectant l'exactitude aussi), qui est également à un niveau avancé de développement. Nous construisons actuellement un nouveau catalogue spectrophotométrique extra-atmosphérique d'étoiles, basé sur les mesures du satellite GOMOS, qui est essentiellement un photomètre stellaire spatial. De plus, nous essayons de construire un modèle de luminosité du ciel, basé sur les positions du soleil et de la lune, de l'épaisseur optique atmosphérique et des mesures de fond de ciel du photomètre stellaire. De manière inattendue, cela semble conduire à une autre façon de mesurer l'épaisseur optique dans des conditions de ciel brillant, offrant un moyen de quantifier toute dégradation du débit optique du photomètre stellaire, par exemple en raison du dépôt de cristaux.

Mots-clés: photométrie stellaire, justesse de mesure, étalonnage, aérosols, Arctique.

Acknowledgments

Since the start of my PhD project, several unforeseen challenges appeared: continuous hardware failures, starphotometer manufacturer closing business, main funding sources not being extended, hostile environments and, not less important, a new baby. However, the support of my supervisor, Norm O'Neill, remained unshakeable. He didn't hesitate to get deeply involved in a humongous effort of analysing every single bit of my results. He also knows how to build and maintain student confidence and motivation, by continuously giving credit for the smallest achievement. Actually, we appeared to be in a colleague-colleague, rather than a professor-student relationship. Looking back, I would say that a good scientific supervisor should share a lot with a tennis coach, sport that both of us enjoy watching: hard worker and fine psychologist. In addition, I was lucky enough to have not only one good supervisor, but unofficially two, since my MSc supervisor, Jean-Pierre Blanchet, was always ready to help, scientifically, logistically, and even financially. I'm grateful to both of them for their support, for believing in me and for always encouraging me to create and develop new ideas.

Finishing up this PhD project from the family perspective looked like a far fetched endeavour, while other down to Earth family needs have to be fulfilled with priority. Obviously, this would have not been even possible to start without the unconditional support of my wife Letiția - my friend, my confidant and my love. I'm grateful to her and I consider it to be a truly family project. Lastly, it would have been the honour of my life to invite my parents to my PhD defence. For such an accomplishment my father would have been overjoyed and my mother would have mention it for years. Unfortunately they left us too soon for a better world. I miss them very much and I'm grateful to them for what I am today.

to my beloved wife, Letiția

to my parents, Virgil & Vasilica

Contents

Framework

0.1 Starphotometry

Starphotometry, or stellar spectrophotometry, is a passive remote sensing method for retrieving the spectral optical depth of the atmosphere. This is accomplished by comparing the measured signal with the extra-atmospheric radiance of a reference star. Starphotometry was introduced in the early 1980's [1, 17] as a night counterpart to sunphotometry [6] in order to obtain continuous 24 h aerosol optical depth monitoring coverage. Despite all the technological advances, robust and accurate starphotometry remains a challenge [5, 2] that has limited its evolution.

The general objective in this work is to inspire trust and interest in starphotometry by improving its reliability, its measurement accuracy and by identifying particular cases where it outperforms sunphotometry (which is in fact starphotometry with the star being our Sun). In order to achieve such an objective we need to better understand the detailed nature of specific starphotometry attributes: the different spectral classes of stars, the properties of weaker reference sources, the consequences of a larger telescope aperture, a smaller Field of View (FOV) etc.

Improving starphotometry reliability (which is associated with its data collection rate) should be addressed through both, hardware improvements and better observing strategies for mitigating environmental challenges. The accuracy of optical depth retrieval remains critical for particle feature extraction methods which require sub 0.01 optical depth error [14], or equivalently, 1% photometric accuracy. While this target is generally achieved in sunphotometry [18], it still represents a challenge in starphotometry. In order to fulfill such an accuracy requirement, it is essential to identify all the major sources of errors, facilitate the quantification of measurement

accuracy and, eventually, mitigate the diverse error mechanisms.

One key advantage of starphotometry, aside from providing nighttime observations to complement sunphotometry, is its 100% duty cycle in the presence of clear skies. In contrast, the other nighttime alternative, moonphotometry [4], is limited to a 50% duty cycle, (i.e. between the first and last quarters of the moon). Starphotometry is particularly relevant near the poles, during the long polar night. It enables remote sensing measurements from a region and period for which one generally has very little information. Beyond that, the availability of numerous stellar sources ensures the acquisition of observations in almost any direction. This facilitates the synergistic acquisition of data from other instruments: key examples include (generally zenith-pointing) ground-based lidars ([8], satellite-based lidars, such as the nadir-pointing CALIOP onboard the CALIPSO satellite [11] and the slant-path-looking ALADIN Doppler lidar onboard ADM-Aeolus [7]. In addition, because forward scattering into the broad FOVs of sunphotometers and moonphotometers can induce significant optical depth underestimation [12], the much smaller FOVs of starphotometers ensure a distinct advantage of starphotometry in this regard.

0.2 Observing challenges

An important aspect of the project was to identify and quantify unknown sources of accuracy errors. A particularly frustrating attribute of starphotometry is that even the known error types are difficult to estimate. Even if assessed by comparison with other instruments (lidars, other starphotometers, moonphotometers), those errors may also vary as a function of different observing conditions. The level of trust in such systems consequently remains low. If mass usage is a benefit to instrument maturation then starphotometry is at a disadvantage : there are currently only 2–3 operational starphotometers worldwide. In addition, the higher degree of technical complexity and failure rate relative to sunphotometers and moonphotometers, their high maintenance and troubleshooting requirements, can make them unattractive for operational observatories. As a consequence of the attendant low demand for starphotometers, Dr. Schulz & Partner GmbH (the only company fabricating starphotometers as a serial product) went out of business before being able to properly fix some

of the technical issues identified by current users (e.g. internal overheating, inappropriate lens coating, missing access to some critical parameters etc). This leads to a cycle of mistrust: one needs many observations and studies to improve reliability and accuracy, while we don't have enough operational instruments due to their technical issues and their debatable accuracy.

Starphotometers also have their share of specific challenges related to the observing site. One common problem is the deposition of dust, dew, frost, or ice particles on the telescope (with attendant effects on its optical throughput). A polar site, such as Eureka, poses several additional challenges: greater near sea-level air turbulence (with effects on the star spot size), higher scintillation induced variations at large airmasses (affecting the measurement precision), very low ambient temperature (affecting the hardware, notably the mechanical moving parts and electrical wiring), permafrost (preventing a good electrical grounding), the impact on nearby instruments (sensitive to electromagnetic interference, or EMI), the remote location (meaning long delays in shipping of parts for repairs), very dry air (outgassing of electronic components), limited on-site support (for operation and maintenance), dangerous accessibility (open surroundings with risks of frostbite and extreme wind chill, not mention the dangers of wild animals: wolves, muskoxen, polar bears), very slow internet (for data transfer or remote control). Our starphotometers have undergone numerous hardware failures, every year of their 11 years of operation. This led to a high risk of not being able to complete the planned studies in a timely manner.

0.3 Data collection

Due to the aforementioned technical issues and challenges, data collection in Eureka (our only operational site) has, as made evident in Figure 1, sustained frequent gaps throughout the 11 years of operation at that site. On that figure, OSM and TSM represent One-Star Measurement and Two-Star Measurement operating modes, respectively. The OSM mode is principally used under cloudy skies to capture their higher temporal optical depth variability or over a longer unsupervised period of clear and/or partially cloudy conditions by observing Vega (a high star allowing more robust observations in the case of high optical depth). The TSM mode is principally

0.3. Data collection

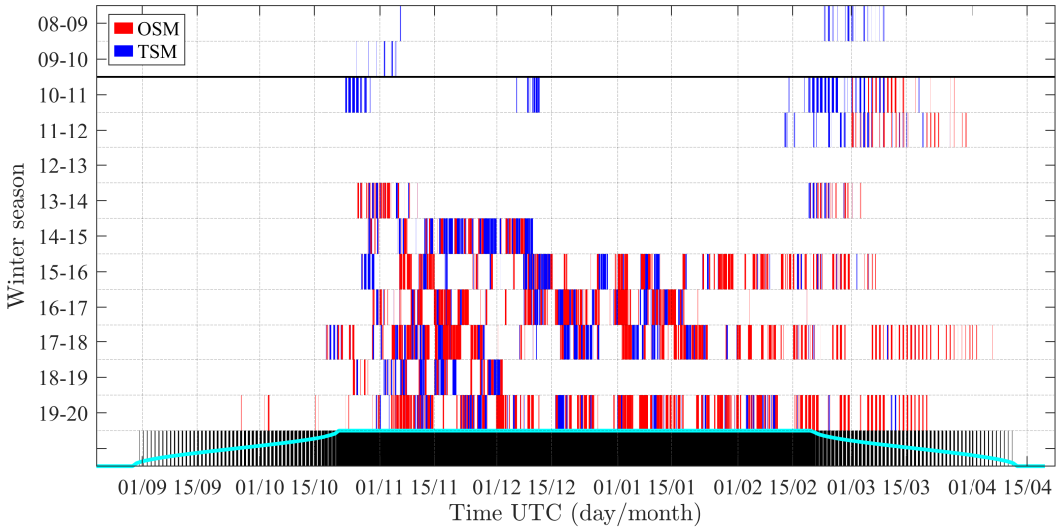

Figure 1 – Starphotometer data collection duty cycle. OSM and TSM stand for One-Star Measurement (red vertical bars) and Two-Star Measurement (blue vertical bars) operating modes, respectively. The width of the black vertical bars represent the nighttime duration from sunset to sunrise (they merge into a single black mass during the polar night), while the height of the cyan curve is indicative of nighttime duration (see text for details on the nighttime duration).

used in clear sky conditions (for calibration check), or during aerosol events. The bottom dark bands of Figure 1 represent the nighttime from sunset to sunrise, i.e. up to 50′ below the horizon (a number that accounts for the refractive bending of the solar disk). The height of thee cyan curve represents the nighttime duration where the end of the night is marked by the sun being 6° below the horizon rather than the refractive horizon (6° below the horizon being the start of the civil twilight period for which one generally cannot make observations). More details on the observation modes are presented in the second article of the thesis.

The first two winter measurement seasons (2008-2010), during which we worked with older versions of the starphotometer and mount/dome, were carried out on a campaign basis. This was principally because the telescope mount and dome were not ruggedized for continuous Arctic operation, and because of the limited availability of supervised operation. Starting in 2010 we installed the latest starphotometer version and a specially built dome along with a mount for Arctic conditions (see

details in the first article). During the first four winter observing seasons we had several concurrent hardware failures and had to deal with the frustrating impact of starphotometer EMI emissions on nearby meteor radar measurements along with the data collection compromises that had to be implemented to temporarily sidestep the issue. After mitigating the EMI issue by relocating the compromised meteor radar array, the data collection rate improved. A starphotometer overheating issue, once identified, was worked around simply by implementing another layer of protection: an analogue thermostat that turns off the internal computer when the software-based internal temperature control fails. In order to limit such abrupt observation shut-downs, we also reverse engineered the main electronic control board since the original design was no longer available (we re-designed it in India and manufactured it in Romania). This led to a significant improvement in data collection (starting with the 2015-2016 season). Another issue occurred however in the second half of the 2016-2017 season, by the filling up of the small amount of space initially allocated to the starphotometer operating system (the problem was fixed the following summer in an UQAM laboratory). Another notable issue in the second half of the 2018-2019 season was a damaged telescope-mount OS card (replaced by the manufacturer with a more robust OS card).

0.4 Main results

Our technical and scientific contributions resulting from the PhD project are described in the following three articles.

0.4.1 Article 1

While this initial article was refereed according to the proceedings standards of SPIE Proceedings board, it was nevertheless not targeted as a peer reviewed scientific paper, but rather as an introduction to Arctic starphotometry and its technical challenges. It describes in detail, the challenges we had to overcome in addressing the technical and logistical issues related to operating a star-photometer in a remote and environmentally hostile location such as Eureka. The success that we achieved in this

extreme environment should, we hope, inspire trust in the reliability of starphotometry in general. In this paper we addressed a number of important problems: electrical grounding issues due to permafrost, outgassing due to dry air, optical throughput issues due to the lens coating, the major issue of the omnipresent crystal deposition on the telescope and the necessity for remote operation. For more detailed information, the article is presented in Chapter 1.

0.4.2 Article 2

The second article (Chapter 2), of the same title as this thesis, contains the principal remote sensing research results of the PhD project. It elaborates on the theoretical starphotometry framework and identifies the parameters susceptible to inducing significant errors. It notably identifies the advantage of performing a star independent (instrument dependent) calibration. Most major sources of accuracy errors specific to starphotometry are identified and analyzed with a view to providing mitigation avenues. A singular emphasis was placed on achieving an optical depth error of less than 0.01. The main contributions are summarized below:

- The inaccuracies of star catalogs (absolute reference sources) was determined to be a major problem, particularly in the case of bandwidth mismatch between the catalog and the instrument. One way of avoiding star catalogs is to frequently calibrate a given instrument relative to a given star (or stars) at a high altitude observatory: this is, however, impractical due to technical challenges related to, for example, frequent installation, de-installation and transport impacts on instrument stability and the availability of the same stars at the home and calibration sites. A more practical solution is to build a more accurate high resolution spectrophotometric catalog for bright stars that would enable a star independent calibration (a catalog whose member magnitudes would preferably be measured from space). Such flexibility would enable on-site calibration.
- Detector spectral drift may generate major accuracy errors related to the large slope of the stellar spectra. On-site spectral calibration can be frequently performed by taking advantage of stellar and telluric (atmospheric trace gas) absorption lines.

- The spectral location of the standard starphotometer channels must avoid the deep stellar and telluric absorption lines. This is more critical for some spectral classes of stars (B4 to A6) with deeper absorption lines. In this context, we notably identified problematic O_4 telluric absorption lines and proposed an optimised channel allocation.
- Airmass inaccuracy may become important at large airmasses, if they are calculated from time stamp data, so it requires accurate GPS time recording. In this context we demonstrated the advantage of acquiring data from a higher altitude site.
- The forward scattering error is a major issue when observing through semi-transparent clouds. We demonstrated that our starphotometers readily attained the 0.01 error target with the exception of certain large-particle ice clouds. This result underscored the distinct advantage of starphotometry over large-FOV sun or moonphotometry.
- The high brightness and associated variability of the near infrared spectrum of the sky background may be a limitation for accurate identification and parameterization of coarse mode particles such as coarse mode aerosols and clouds. The problem may be mitigated with a colder F class star such as Procyon which is brighter in the near infrared (the spectral class essentially being related to the effective surface temperature of the star).
- Several issues specific to our type of starphotometers were identified and quantified. These were mostly limited to optical alignment, linear detection range, temperature control and other shortcomings that could potentially have significant impacts. In this context, we identified a minimum required FOV that ensures the integrity of the stellar flux detection, i.e. the preservation of the optical throughput.
- An issue of particular importance in the Arctic is the deposition of ice crystals on the telescope. This problem significantly affects the optical throughput: it was investigated and a mitigation solution that employed heating bands around the telescope tube was successfully implemented.

This comprehensive investigation, involving the notable complications of a remote

Arctic site, necessitated the bringing to bear of considerable material and intellectual resources. While I performed virtually all the field and lab work described in the article, the input I received from my co-author colleagues and the constant advice, rigorous scientific cross-checks and in-depth text proofing of my supervisor were determining factors. Lastly, the constant availability of the Eureka operations staff and the instrument manufacturers in providing maintenance assistance and advice for the starphotometer, dome and telescope mount was paramount.

0.4.3 Article 3

While we are concomitantly working on a comprehensive analysis of the calibration procedures, the letter presented in Chapter 3 was intended to more rapidly communicate the innovative notion that a star independent calibration may be performed on-site (even at near sea-level elevations). The paper starts with a statistical analysis of typical clear sky periods for Eureka. The rapidity of the multi-star calibration and the avoidance of significant sky transparency variations is then underscored. The possibility of such a multi-star calibration is a direct consequence of concepts presented in Article 2 on the advantages of using a star independent calibration. We also demonstrated that a particular "Reversed" calibration method further reduced the calibration errors to values approaching the 0.01 accuracy target of Article 2. The achievement of this target was confirmed by means of a repeatability analysis.

0.5 Originality

While important starphotometry advances were achieved over the last decade, notably by Perez-Ramirez [16, 15], a comprehensive analysis of accuracy errors has not been carried out since the astronomy studies of Young [19] in the 1970's. Our work updates and complements those investigations to the current technological reality and specificity of starphotometry for atmospheric remote sensing. This allowed us to quantitatively asses the main sources of errors and how to address them. We identified the contaminating effects of the O_4 absorption lines, an artefact that has not been reported in the starphotometry literature. These features inhibit accurate

ozone optical depth removal and accordingly lead to a distortion of the retrieved aerosol spectrum. We identified an optimised 45″ FOV for use in starphotometry: this number represented a compromise between preserving the optical throughput and limiting the forward scattering errors when observing clouds. We also identified, for the first time, the starphotometry advantage over sunphotometry in the context of the forward scattering errors. Another original contribution was to promote the importance of employing the cold star spectral class (e.g. F class) when observing clouds and generally the use of early B stars or late A stars if better accuracy is required. The crystal deposition on the telescope entry window seemed, for a long time, to be an impossible issue to solve. After several trials, we found that a heating band was a successful solution for most environmental situations. All of these above-mentioned improvements suggested that achieving the 1% accuracy mark was finally feasible. In addition, our implementation of remote control and maintenance procedures that could be carried out using a smart phone (i.e. anytime and from anywhere in the world) are unique, at least in the starphotometry community. This finally opens up, for the first time, the possibility for building trust in this type of instruments.

0.6 Conclusion

Such comprehensive analysis should have been supported by concerted community efforts across several sites. The limited availability of operational starphotometers and the acute necessity to mitigate the level of mistrust in these instruments, motivated our efforts to address this problem in all its complexity. However, the fact that we based our analysis principally on only one type of starphotometer and largely on one Arctic sea-level observatory, may have lead to the neglect of potential errors specific to other sites: for example, humidity related issues in the tropics, dust deposition in arid environments, or sky background biases at sites suffering from urban light-pollution. Beyond those examples, we may still have neglected other important errors, as we continuously, and sometimes unexpectedly, encountered large magnitude signal anomalies in specific situations. Accordingly, in order to validate the findings identified here, we recommend regular participation in observing campaigns at other

sites in order to compare and validate the expected accuracy with other collocated instruments.

In addition to this work, we are finalising a comprehensive analysis of non-systematic starphotometry errors (errors in precision). Those results further advance our goal of a comprehensive analysis of calibration methods (ultimately affecting the accuracy too). We are currently generating a new extra-atmospheric spectrophotometric star catalog, based on measurements of the GOMOS sensor, which is basically a space-based starphotometer. In addition, we are formulating a sky brightness model that is based on the sun and moon positions, atmospheric optical depth and starphotometer sky background measurements. This has tentatively lead to an alternative way of measuring the optical depth in bright background conditions and thereby, a tool for flagging and quantifying any starphotometer optical throughput degradation (due to crystals deposition, for example).

0.7 Other published work

1. **Ivănescu L.**: Une application de la photométrie stellaire à l'observation de nuages optiquement minces à Eureka, NU, MSc thesis, UQAM, 2015* [8].

   - *Contribution*: My Masters in Science (MSc) thesis in Atmospheric Sciences (* "An application of starphotometry to the observation of optically thin clouds in Eureka, NU") overlapped the work of the PhD project due to a seemingly endless stream of technical difficulties. It includes an original remote sensing method for retrieving particle size and number concentration from the synergy of radar and lidar profiles. In addition, it helped in understanding the optical coherency of lidar-starphotometer measurements.

   I also made contributions to and have been a co-author of several other peer-reviewed articles during my PhD work.

2. Baibakov K., N. T. O'Neill, **L. Ivănescu**, T. J. Duck, C. Perro, A. Herber, K.-H. Schulz, O. Schrems: Synchronous polar winter starphotometry and lidar measurements at a High Arctic station, Atmospheric Measurement Techniques, vol. 8, issue 9, 3789-3809, 2015 [3].

- *Contribution*: It was partly based on data I acquired from Eureka, for which I partly did data processing, as well as for the Alaska campaign. Several theoretical developments were inspired by my MSc thesis.

3. O'Neill N. T., K. Baibakov, S. Hesaraki, **L. Ivănescu**, R. V. Randall, C. Perro, J. P. Chaubey, A. Herber, T. J. Duck: Temporal and spectral cloud screening of polar winter aerosol optical depth (AOD): impact of homogeneous and inhomogeneous clouds and crystal layers on climatological-scale AODs, Atmospheric Chemistry and Physics, vol. 16, issue 19, 12753-12765, 2016 [13].

   - *Contribution*: I provided the processed starphotometer data from Eureka and helped analysing it.

4. Libois Q., C. Proulx, **L. Ivănescu**, L. Coursol, L. S. Pelletier, Y. Bouzid, F. Barbero, E. Girard, J.-P. Blanchet: A microbolometer-based far infrared radiometer to study thin ice clouds in the Arctic, Atmospheric Measurement Techniques, vol. 9, issue 4, 1817-1832, 2016 [10].

   - *Contribution*: It was based on the development of an instrument (FIRR) that I helped characterising through measurements in the lab and in the field.

5. Libois Q., **L. Ivănescu**, J.-P. Blanchet, H. Schulz, H. Bozem, W. R. Leaitch, J. Burkart, J. P. D. Abbatt, A. B. Herber, A. A. Aliabadi, É. Girard: Airborne observations of far-infrared upwelling radiance in the Arctic, Atmospheric Chemistry and Physics, vol. 16, issue 24, 15689-15707, 2016 [9].

   - *Contribution*: It was based on the data acquired during my participation with the FIRR to the pan-arctic Pamarcmip 2015 Polar 5/6 AWI/NETCARE airborne campaign. I also did data processing and the contextual satellite analysis.

6. Ranjbar K., N. T. O'Neill, **L. Ivănescu**, J. S. King, P Hayes: Remote sensing of a high-Arctic, local dust event over Lake Hazen (Ellesmere Island, Nunavut, Canada), Atmospheric Environment Journal of Elsevier, to be submitted in 2020.

   - *Contribution*: I did meteorological data analysis and interpretation, based on ground weather data, and from Polar 6 measurements during Pamarcmip 2015.

Chapter 1

Challenges in operating an Arctic telescope

Foreword

Article published on 22 July 2014 in the Proceedings of SPIE (Society of Photo-Optical Instrumentation Engineers), Ground-based and Airborne Telescopes V!

Challenges in operating an Arctic telescope

Liviu Ivănescu[a,b], Konstantin Baibakov[a], Norman T. O'Neill[a], Jean-Pierre Blanchet[b], Yann Blanchard[a], Auromeet Saha[a], Martin Rietze[c] and Karl-Heinz Schulz[d]

[a]Centre d'applications et de recherches en télédétection (CARTEL), Département de Géomatique Appliquée, Université de Sherbrooke, 2500, boul. de l'Université, QC, J1K 2R1, Sherbrooke, Canada;
[b]Department of Earth and Atmospheric Sciences, Université du Québec à Montréal (UQÀM), Case postale 8888, Succursale Centre-ville, QC, H3C 3P8, Montréal, Canada;

[c]Baader Planetarium GmbH, 82291, Mammendorf, Germany;

[d]Dr. Schulz & Partner GmbH, Falkenberger Str. 36, 15848, Buckow, Germany

ABSTRACT

We describe our seven year experience and the specific technical and environmental challenges we had to overcome while operating a telescope in the High Arctic, at the Eureka Weather Station, during the polar winter. The facility and the solutions implemented for remote control and maintenance are presented. We also summarize the observational challenges encountered in making precise and reliable star-photometric observations at sea-level.

Keywords: star-photometry, Arctic, telescope, operation, site testing, astronomy, remote sensing, atmosphere.

1. INTRODUCTION

The utilization of optical telescopes in the polar environment has been explored for several decades, particularly for astronomical observations and the remote sensing of the Earth's atmosphere. In Antarctica, the concept of stellar observations at visible wavelengths, was declared in 1987 as being impractical[1].[2] After finding in 1999 that the observing conditions are actually greatly improved beyond the first tens of meters above the ground,[3] the quest for astronomy in Antarctica gained a new momentum.[4] Aiming at more ambitious facilities on top of 20-30 m towers,[5] small optical telescopes are currently providing[6] some insight into operational challenges particular to Antarctica.[7]

The Arctic was perceived as being less amenable to astronomical observations, based mainly on Low Arctic ($< 75\,^{\circ}$N) Inuit knowledge,[8] or the weather reports of summertime ships.[9] Starting in 1993, the first sea-level, wintertime, visible starlight observations, were in fact dedicated to atmospheric remote sensing[10].[11] Assessments of the Arctic as being also appropriate for astronomy came only after 2002[12][13],[14] based on satellite or radiosonde data. Site testing in the High Canadian Arctic, based on ground observations, confirmed its excellent potential[15] at high elevations.[16]

Optical stellar observations at ice-level in Antarctica, or at sea-level in the Arctic, are especially difficult. Drawbacks of particular note are the air turbulence and the almost omnipresent ice crystals. In spite of these factors, there is a strong scientific motivation for the investigation of low altitude atmospheric constituents, such as the low to mid-tropospheric aerosols of the Arctic haze. We report the challenges encountered in operating a sea-level optical telescope in the High Arctic, at the Eureka Weather Station (80 °N, 86 °W). The objective of this instrument was to perform accurate star pointing and photometry for remote sensing applications. A similar facility is located in Ny-Alesund, Spitsbergen (79 °N, 12 °E),[17] while a third site, planned for Dome C in Antarctica, is currently on hold.[7] The challenges uncovered here may hopefully lead to the development of more

Further author information:
Send correspondence to Liviu Ivănescu: E-mail: Liviu.Ivanescu@usherbrooke.ca, Telephone: +1 514 779 2708.

robust pointing and measurement techniques for future telescopes that will eventually be deployed at higher elevations.

In the context of atmospheric science, star-photometry is commonly known as the only current nighttime remote sensing approach for directly measuring the optical depth (OD) of the Earth's atmosphere. By measuring the starlight attenuation, it provides multi-wavelength OD from the near-UV to the near-IR. This allows for the investigation of the optical properties of atmospheric particles, notably aerosols and clouds. Aerosol and cloud optical depth represents the largest source of uncertainty in the assessment of the global radiation budget,[18] with consequences in terms of the North-South atmospheric balance. Radiation budget considerations are critical during the Polar winter when monitoring capabilities are severely constrained. This reality renders star-photometry all the more important as a remote sensing methodology.

2. SITE CHALLENGES

2.1 Accessibility and facilities

The Eureka Weather Station (79 °59′N, 85 °56′W), which has been operated by Environment Canada (EC) since 1948, is the northernmost year round civilian facility (Fig. 1). It is located on the Foshiem Peninsula, Ellesmere Island, Qikiqtaaluk Region, on the north shore of the Slidre Fjord, which connects with the Eureka Sound to the west. Access is allowed only after obtaining a visitor permit from EC, or being part of a research team from CANDAC (Canadian Network for Detection of Atmospheric Change), which has a partnership with EC. For other researchers, the NRCan Polar Continental Shelf Program (PCSP), which maintains a large scale facility at Resolute Bay, usually provides accessibility support anywhere in the High Arctic, including Eureka.

The Eureka station is accessible all year round. Most of the Inuit communities located on the flight paths from the south, currently have modern and well maintained airports that serve as transit points and refueling depots. There are two main routes for traveling to Eureka by air. The first, 4 200 km long, is from Montreal or Ottawa, via Iqaluit (the Nunavut capital), all the way to Resolute with commercial scheduled flights (Fig. 1), at a cost of about 6 000 $/person for a round trip. From Resolute to Eureka one has to rent a private charter, usually Kenn Borek Air, located in Resolute. As there is only one commercial flight from Iqaluit to Resolute every few days, there are two main drawbacks with this trip option. One concerns the eventual loss of luggage, which may arrive in Resolute a few days later, with the next scheduled flight. Secondly, if the weather is bad in Eureka, one might have to stay several days in Resolute, as the Eureka airport doesn't have radar for non-visual landings.

The second option, 3 200 km long, is from Edmonton or Calgary, to Yellowknife, followed by a rented charter all the way to Eureka (Fig. 1). The flight has to make a stop or two, depending on the payload weight, for refueling. Most of the Arctic airports are not equipped for non-visual landings. Starting from Yellowknife, the first stop is usually not a problem, as there are alternative locations for avoiding the bad weather. The flight departure is then scheduled mostly as a function of the second stop local weather, usually Resolute Bay. With respect to the drawbacks of the Iqaluit flight option, this is more reliable and probably cheaper, even for people coming from Eastern Canada. There are several regular flights per day to Yellowknife and one can wait there at a moderately priced hotel, in case the weather is not appropriate for flying. There are also several competing charter companies in Yellowknife (Summit Air, Air Tindi etc.), from which one can rent a Twin-Otter (or a bigger charter, if necessary). A Twin-Otter can carry about 2 tones of load and about 10 people, is reliable for Arctic operations and can land on shorter runaways. Two round trips to Eureka (one for bringing people in, and one for taking them out) cost around 15 000 $/person.

Yellowknife is a modern, fast developing city, which benefits from an increasing Arctic mining activity, particularly in the diamond industry. One can find there all major North-American tools and equipment providers. If something is forgotten or broken in Eureka, it can be easily ordered and shipped with the next available charter. In addition, as is the case for CANDAC, local companies can provide logistical support, i.e. holding shippings and bringing them to the charter hangar etc.

During the charter part of the trip, from September to May, people must wear an Arctic gear, in case of an emergency landing in a remote area. The Eureka airport, at 78 m elevation and about 3 km inland from the residences, is even able to accommodate the landing of a Boeing 747. The station was recently upgraded with

Figure 1: Accessibility map to Eureka (map credit: Northern Transportation Company Limited).

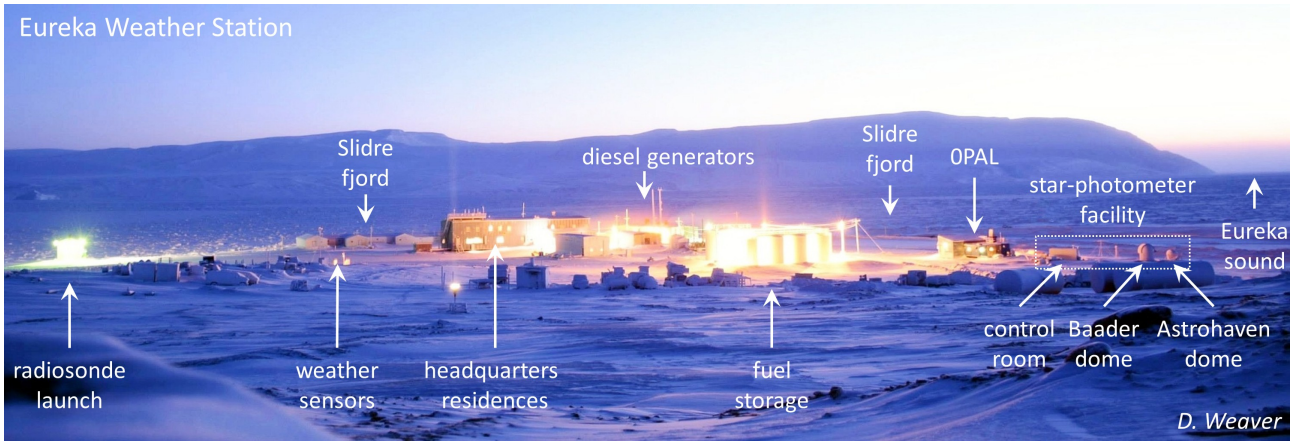

Figure 2: Eureka Weather Station (80 °N, 86 °W), emphasizing the star-photometer facility, near 0PAL Lab.

a modern residence capable of hosting about 50 people (Fig. 2). The cost of services provided by Eureka, as of April 2010,[19] are: bed 250 $/day, three meals (professional cook, two choices) 230 $/day, electricity 1.143 $/kWh, workshop labor 150 $/h, small vehicle with driver 150 $/h, airport fees to land/takeoff a small aircraft 140 $. The land on which one wants to install any equipment is also an object of negotiation with EC and the station.

Electricity is currently provided by three 410 kWh Cummings diesel generators. Blackouts, during which, heating is cut off, can occur several times per year. In winter this is a life threatening event and, if longer than 12 h, the manager is compelled to order an evacuation, which in fact never happened. The fuel used by vehicles and generators is −40 °C rated, but it seems to work just fine down to −50 °C, which is about the lowest ground temperature. The station is serviced all year round by air, once a month, with food and other necessities. Taking advantage of being on the shore of the Slidre Fjord, the station is re-supplied almost every summer by an ice-breaker with construction materials, fuel, vehicles and other heavy items. Arrangements have to be made several months in advance in order to use this service. Depending on weight, the shipping of a sea container from Montreal to Eureka could cost a few thousands dollars. Eureka is also the last re-supplying point for North Pole expeditions, usually starting from the summertime-only research station on Ward Hunt Island,

Figure 3: PEARL Ridge Lab & C-band antenna (left, credit J. Drummond); 2 Ka- & C-band antennae (right).

at the northernmost tip of Canada (83 °06′N, 74 °10′W).[20]

Our organization, CANDAC, was formed in 2005 as a network of Canadian university and government researchers for investigating and monitoring the Arctic atmosphere. It currently operates PEARL (Polar Environment Atmospheric Research Laboratory), a complex of three facilities in the Eureka area: the Zero Altitude PEARL Auxilary Laboratory (0PAL) (Fig. 2), the PEARL Ridge Lab (Fig. 3, left) and the Surface and Atmospheric Flux, Irradiance and Radiation Extension (SAFIRE) laboratory. The PEARL ridge lab, formerly EC's Arctic Stratospheric Ozone Observatory (Astro), is located 14 km from Eureka, at the summit of a 610 meter high ridge. The 0PAL site is located near the EC meteorological station while the SAFIRE station, which includes a 10 m measurement tower, is located near the airport. There are currently more than 25 CANDAC instruments in operation. Among them, the star-photometer facility is just near the 0PAL laboratory (Fig. 2), at 15 m elevation.

Until March 2012, CANDAC was operational all year long, with a permanent, on-site operator for maintaining all instruments. After this date, funding issues required that operations be limited to controlling instruments remotely (for those instruments that could be controlled remotely) accompanied by servicing missions (usually in October) and financed field campaigns (Polar sunrise campaign in the February to March period). Most recently, a moderate increase in operations funding has meant that a part time on-site operator could be employed and that measurement rates could be improved (the funding shortfall after March 2012 had a severe impact on measurement duty cycle).

In order to have adequate control of its instruments, CANDAC developed its own communication system, providing the most northern high speed internet connection. Actually, Eureka is about the northernmost location from where one can still see a geosynchronous satellite, which will be just few degrees over the horizon. Two connections are currently used: a C-band (4-8 GHz) link, at a cost of about 6 000 $/month for a "high speed" traffic (∼380 kb/s) and several Ka-band (27-40 GHz) "low speed" links for non real-time traffic, like data transfer. Until March 2014 the Ka-band links were provided for free by the Canadian Space Agency under the Government of Canada Capacity initiative. Having two connection options is useful for the reliability of the link (and the security of the equipment). There are problems during the summer months, especially in the high frequency band (Ka),[21] when the air moisture and cloudiness increase. As the antennae are pointed close to the horizon, the signals traverse a very long atmospheric path and are susceptible to absorption and scattering.

2.2 Observing conditions

Being near the North Pole, the night sky is characterized by particular conditions that affect measurement strategies inasmuch as the sun is never too far from the horizon. The position of the sun and the planets on or near the ecliptic plane means they share a common constrained geometry (Fig. 4, left) and motion in the sky. The moon is also never too high in the sky, as its orbiting plane is only 5 ° off the ecliptic. Probably here, more than anywhere on Earth, it would have been easer for our ancestors to figure out the heliocentric system. The Polaris star is near the zenith, meaning that all the main solar system objects and most of the stars never rise or

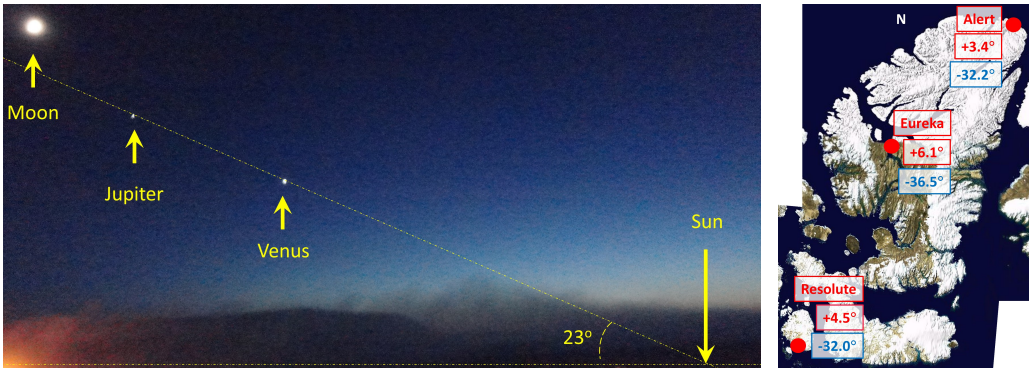

Figure 4: Left: Sun, Moon and stars quasi-aligned on the ecliptic plane; fog on the fjord triggered by diesel generators exhaust. Right: July (red) & January (blue) daily mean surface temperature around Ellesmere Island.

set, rather they move almost parallel to the horizon. The site is also located near the magnetic North Pole, being practically in the center of the auroral oval. This means that auroras are very rarely seen on the horizon, so their contribution to the sky background brightness is not a significant issue in terms of star signal contamination.

The physical environment of Eureka results in anomalously colder winters and warmer summers in comparison with the rest of the Arctic. Fig. 4, right, shows the July (red) and January (blue) daily mean surface temperatures at Eureka and the two nearest stations. One could argue that the reason for this anomaly is a combination of the greater heat capacity of the sea (affecting more the coastal stations in summertime) and the caldera shape of the landscape around Eureka (a topographical condition that is suggested by the general features in the satellite image of Fig. 4). This would arguably allow for the accumulation of heat during the summer and prevent the mixing of the atmospheric boundary layer during the winter. Such a cold environment might help to lower the infrared sky brightness and open up new spectral windows for observing the stars.

The wintertime (December, January, February) upper air radiosonde climatology (1994-2007) above Eureka is depicted in Fig. 5 & Fig. 6. The vertical scale is the square root of the altitude, which emphasizes parametric variations at both, low and high altitudes. The median (50% percentile) profiles, over the whole period, are represented with continuous lines (blue or black), while the 1^{st} (25%) and 3^{rd} (75%) percentiles are shown with dashed lines (red or green). Cloud occurrence (the blue curve of the Max cloudiness graph of Fig. 5) is computed only as an upper limit, inasmuch as the ice nucleation was considered here to start at 100% relative humidity over ice (RH_i). In reality, due to aerosol acidification,[22] cloud formation may be limited to values higher than 150% RH_i.[23] The relative humidity over dew (RH_d) is almost never 100% and pure water droplet clouds are accordingly rare. Therefore, we express the cloud occurrence profile as the percentage of time one has ice nucleation at RH_i >100%. The cloud cover profile (the solid black curve of the Max cloudiness graph of Fig. 5) is computed then as the percentage of time one has any cloud occurrence above the current altitude. Cloud identification from the ground, based on an empirical OD threshold as low as 0.03, found 55% wintertime cloud cover at Eureka,[24] so about 2/3 of our upper limit of 80% (Fig. 5). As an initial estimation, one may then extrapolate such a 2/3 correction factor for the whole profile, which actually agrees very well with the observations.[25]

In order to better compare Eureka observing conditions with other astronomical sites, or the South Pole (as a reference for Antarctica, at 2 835 m elevation), we have also indicated two significant altitudes on the profiles of the Fig. 5 and Fig. 6: the PEARL Ridge Lab (610 m), near Eureka, and the highest peak on the Ellesmere Island (Barbeau, 2 616 m). This shows that the Ridge Lab is almost on top of the thermal inversion (Fig. 5, Temperature) and above the largest values of cloud occurrence (Fig. 5, Max cloudiness). On the other hand, Barbeau peak is above most of the moisture (Fig. 5, Water vapor). In addition, applying the 2/3 correction factor to the upper limit of 47% cloud cover, one may expect about 70% clear (photometric) sky in Barbeau, which is about what one finds at the best astronomical sites.[26]

The wind speed is generally very low, from almost negligible at sea level, to up to few m/s at the elevation

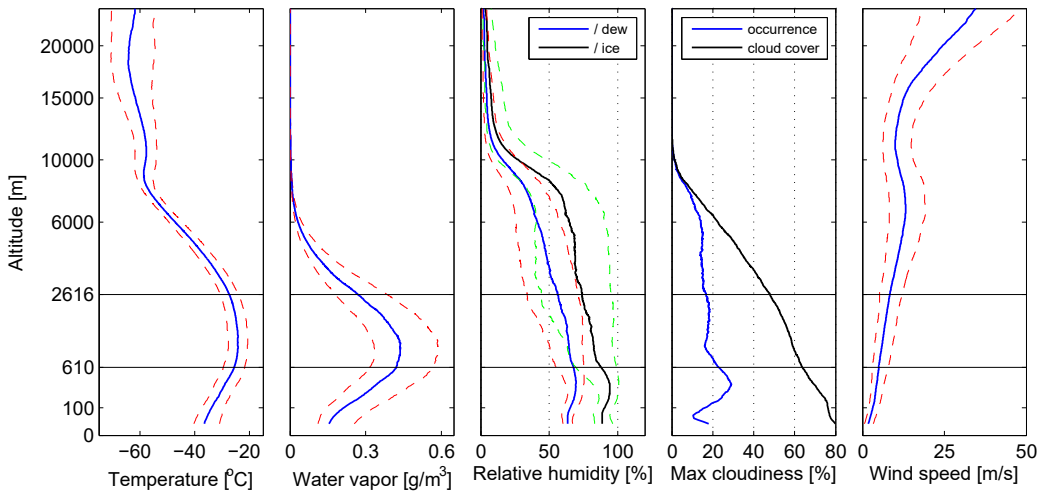

Figure 5: Radiosonde profiles above Eureka: winter median (DJF), 1994-2007; dashed lines: 1^{st} & 3^{rd} percentiles.

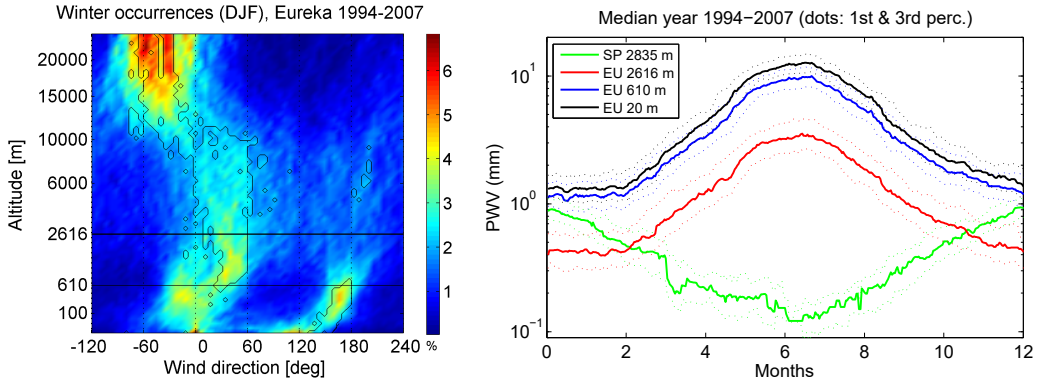

Figure 6: Radiosonde measurements above Eureka: wintertime (DJF) wind direction occurrences over a period extending from 1994 to 2007 (left); vertical integration of Precipitable Water Vapor (PWV): median for the same period (right). EU & SP stand for Eureka & South Pole, respectively.

of the Ridge Lab and Barbeau peak (Fig. 5, Wind speed). The air circulation above Eureka is presented in the left-hand chart (65×65 pixels) of Fig. 6. The color scale shows the percentage of radiosonde samples when the wind, of any speed, arrives from the directions and altitudes covered by a pixel ($\sim 6°$/pixel). In order to emphasize the main air circulation pattern, one also limits our analysis to the high speed winds (>10 m/s). Their 50% occurrence (from all the radiosonde samples) are enclosed within the black contours.

One can then identify stable, high speed, northwesterly winds in the stratosphere, most probably part of the polar vortex, at altitudes higher than about 10 000 m. From polar (Hadley) cell air circulation considerations, one should expect upper tropospheric southerlies and lower tropospheric northesterlies. While one can identify northesterlies in the whole troposphere, down to the Ridge Lab elevation (wind direction at $\sim 45°$ in the chart of Fig. 6), the high altitude southerlies are less obvious. On the other hand, one can observe evident high speed southerlies (enclosed in the black contours) below the Ridge Lab elevation. It may mean that Eureka is too close to the pole for experiencing the expected air circulation pattern, or so close to the pole that one might have an additional inverted polar cell. On the other hand, upper tropospheric northesterlies (instead of southerlies) may also be due to local semi-permanent synoptic features, like the cyclones traveling north along the Baffin Bay, between Canada and Greenland, and east of Eureka.[27] Bellow the Ridge Lab elevation, those northeasterlies are quenching down, having a less stable direction, most probably due to the landscape, inasmuch as Eureka is downhill and south of the Ridge Lab. In addition, the low elevation southerlies tend to turn left, to become

Figure 7: Events of typical cloudy filaments in Eureka coming from the south: every picture is a different event, both raws show similar time of day, while left to right show various times from morning to after-noon (views from south-east to south-west).

easterlies, when approaching sea level. According to the Ekman theory, this means that they are associated with occasional low pressure systems west of Eureka and above the Canadian archipelago, where one usually finds the highest presence of high pressure systems during the winter.[27] From our experience, wintertime cloudy events are generally also from the south (Fig. 7), probably due to such systems. The generally calm atmosphere of the winter is abruptly changed in spring, usually during the month of March, by northwesterly blizzards of more than 10 m/s wind speed at the surface.

The vertically integrated water content, expressed as Precipitable Water Vapor (PWV) in the right-handed graph of Fig. 6, emphasizes a very dry winter atmosphere. This is computed from the twice daily radiosonde measurements, as a 30 day running median, so occasional high frequency events of short duration and high moisture content are likely filtered out. At an altitude comparable with other astronomical sites, one finds values of PWV $\sim$0.4 mm for Barbeau peak. This is comparable with the South Pole (0.1-0.2 mm) and drier than the current estimation for Summit, Greenland (0.9 mm).[28] Even the Ridge Lab, at $1.5 - 2$ mm, is comparable with the best astronomical sites in their dry season[29,30].

Semi-transparent ice clouds, mainly found at mid-latitudes as high altitude cirrus, are often neglected in cloud cover calculations. They are actually present more than 40% of the time.[31] During the polar night they have a pan-polar presence 50-60% of the time and occur at any altitude, including ground level.[22] Such optically thin ice clouds (TIC), OD < 3, are a major motivation for star-photometry observations at Eureka. From our experience, TICs usually originate in the south, probably driven by low pressure systems west of Eureka (Fig. 7 shows their South-North filamentary pattern). As shown in Fig. 5, one also has an increased cloud occurrence near sea level. Low laying TICs, or occasional supercooled liquid fog, are mostly found along the fjords (Fig. 8, a), but the northeasterly winds may sometimes advect them uphill to the Ridge Lab.

While being vital for the station, the diesel generators also vent exhaust fumes into the air. The exhaust triggers cloud nucleation and can produce fog just above the station (Fig. 8, b), particularly at very low temperatures ($< -40\,^{\circ}$C), a phenomenon that occurs often during the polar winter at Eureka. The lowest temperatures occur during clear sky scenes, with northeasterly winds moving the fog southwest, towards the fjord. A lesser exhaust, produced by the generators at the airport, also moves above the station and star-photometer, towards the fjord, at a higher elevation ($\sim$ 100 m). Beyond adding an unwanted contribution to the optical depth, such fog also backscatters the streetlight, contributing therefore to the sky background pollution. Fig. 8 (b) shows the Eureka complex light pollution, below $-40\,^{\circ}$C. Some of the clear sky scenes, appropriate for aerosol observations, are accordingly affected by the local pollution.

Snow cover is basically everywhere on the ground, generally being dry (no mixed phase), made up of small crystals, with the consistency of a powder (Fig. 8, c). This means that even the mildest air currents can induce blowing crystals. For this reason, the ground snow preserves a fresh consistency, which could be an explanation of the high albedo. Actually the albedo is so high, that even starlight is sufficiently bright to visually perceive the

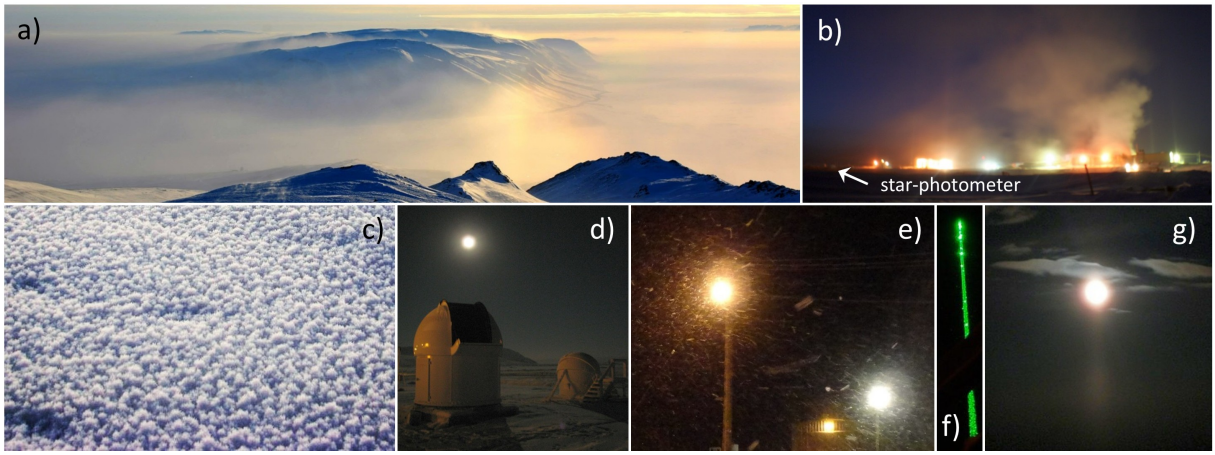

Figure 8: Observing conditions at sea level in Eureka: a) fog along the fjord; b) light & exhaust pollution at Eureka; c) the type of fresh powder like snow that leads to blowing crystals; d) strong illumination conditions caused by high-albedo snow reflecting moonlight; e) ice crystal effects on light pollution at Eureka; f) backscatter of a lidar beam on ice crystals layers; g) Moon pillar due to hexagonal ice crystals.

landscape. It produces a diffuse reflection, giving a surreal milky illumination. This effect is obviously amplified when the moon is up (Fig. 8, d), and accordingly increasing the brightness of the sky background. Most of the light coming from the street illumination around the station also ends up being backscattered towards the sky, contributing to the light pollution of the sky background. While this is experienced at the Eureka station, as long as the moon is down, the brightness of the sky background at the Ridge Lab seems to be negligible.[32]

The ice crystals in the air are an almost omnipresent feature near the sea-level. They do not only redeposit on the equipment, including the telescope, but also increase the scattered light pollution of the sky background, especially near the station street lights (Fig. 8, e). Installing an optical telescope facility on an isolated high peak will accordingly help to minimize surrounding ground surface and the consequent blowing snow, as well as minimize light pollution sources.

In addition to crystals lifted up from the ground, one also has frequent events of clear sky precipitating crystals in the polar atmosphere. Given the low moisture content in the air only a few such crystals are formed and the atmosphere remains optically transparent. Some sublimate from lower, dryer layers, before even reaching the ground. Fig. 8 (f) emphasizes a scene with brighter spots along the lidar backscatter beam, corresponding to ice crystal layers. Even if they don't precipitate to the ground, they still scatter the starlight and thereby increase the scintillation.[11] Crystal habits having a hexagonal plate shape are often formed.[33] They settle out like tree leaves, becoming horizontally oriented as they descend. A proof of such orientation are the typical polar scenes of Sun pillar and Sun dogs, when the Sun is near the horizon.[34] If such crystals are present at higher densities, even the moonlight can be subjected to such optical effects (Fig. 8, g).

At sea level, one can observe, with the naked eye, that the stars have higher scintillation than normally seen at mid-latitudes. On the other hand, from the 610 m elevation Ridge Lab they appear almost still. This means that one has a very turbulent boundary layer just above Eureka, probably due to turbulent northerlies below the Ridge Lab. The strength of the turbulence can be quantified by the angular size of the focal plane star spot, which is usually called astronomical seeing, or simply seeing. Our sea level starphotometer measurements indicate that the seeing is sometimes more than 3 arc-seconds, while at the Ridge-Lab it's mostly sub-arc-second.[16] Given the size of the focal plane star spot and the scintillation accentuated by the ice crystals, one may occasionally have difficulties centering the star on the detector. As our observing procedure alternatively measures the sky background and the star, the centering phase becomes time consuming, occasionally failing and interrupting the acquisition.

The frozen ground also presents difficulties for the equipment, inasmuch as one cannot have a proper electrical grounding. This means that one cannot filter stray oscillations, while the floating signals provoke electromagnetic

Figure 9: Abundant flora and fauna in Eureka (80 °N, 86 °W): flours and grass (left), diverse fauna (right). Some of the latter can be a threat for humans and their equipment (cables broken by musk ox are circled in red).

interference (EMI) in nearby instruments. EMI investigations in such an environment were unsuccessful in isolating and neutralizing the interference. In such situations the only solution is to require, if possible, that a significant distance be maintained between the different instruments.

2.3 An oasis in the Arctic

Eureka is known as the "Garden spot of the Arctic" to the northernmost Inuits who are located 600 km further south. This is because its abundance of flowers and animals stands out as an oasis in contrast to the high Arctic desert which characterizes the region in general. The moderately warmer summertime temperatures in Eureka (Fig. 4, right) allow for a thin permafrost melt layer that is thick enough for the sustainable growth of grass and flowers (Fig. 9, left). Such herbal presence is then the basis for surprisingly diverse animal life during the polar winter (Fig. 9, right). Actually, the past was even more favorable for hosting a diversity of plant and animal life. Eureka is an archaeological paradise for finding fossilized wood and ancient sea creatures.

While the wild life might be nice to watch, it's also a threat for humans and their equipment. In this area the polar bears are not an omnipresent danger. While being much larger than those living in the Low Arctic, they are very rare in Eureka, bears only being spotted every few years. This is because their main food, the seals, are not often present that far inland. The most dangerous threats are the Arctic wolves. Generally they ignore the humans, who usually perceive them more like dogs: it's nevertheless wiser to avoid finding yourself alone near a pack. There are moments when the wolves become aggressive and should be avoided at all costs: when the pack is too big (> 20), when natural food is very scarce (February-March); when meeting the alpha male, and when, despite regulations, visitors feed them and they come to expect feeding from any human on site. In the eventuality of a human being bitten, painful anti-rabies shots have to be administered. Another threat is the musk-ox, a big herbivore with dangerous horns, that becomes aggressive if one approaches too closely. In addition, they are also territorial. Sometimes it happens that the telescope facility ends up inside their territory and the access is compromised for a while. As there are no fences around the Eureka station, walking alone during the night from the residence to the telescope facility (about 100 m), could therefore be hazardous. Guns are not permitted, but one can carry bear attack deterrent sprays.

Beyond direct threats to the humans, the animals, especially the rodents, are a threat to the equipment, especially the cables. The food being generally scarce and because of their natural need for mastication, they chew on everything they find. Even the musk-ox may grate their body or their horns against the equipment, sometimes breaking the cables (Fig. 9, right). The only way to protect the cables are to bury them, in underground tubes, but that can be done only during the summer, since it's impossible to penetrate the frozen ground during the winter. The underground cables that emerge from beneath the surface remain, however, vulnerable. In case of a cable being broken during the winter, there if no easy way to deploy a new cable underground. This is because the buried cables are rigid, even if rated at $-40\,^{\circ}\mathrm{C}$, and the insertion of a new one may break the others.

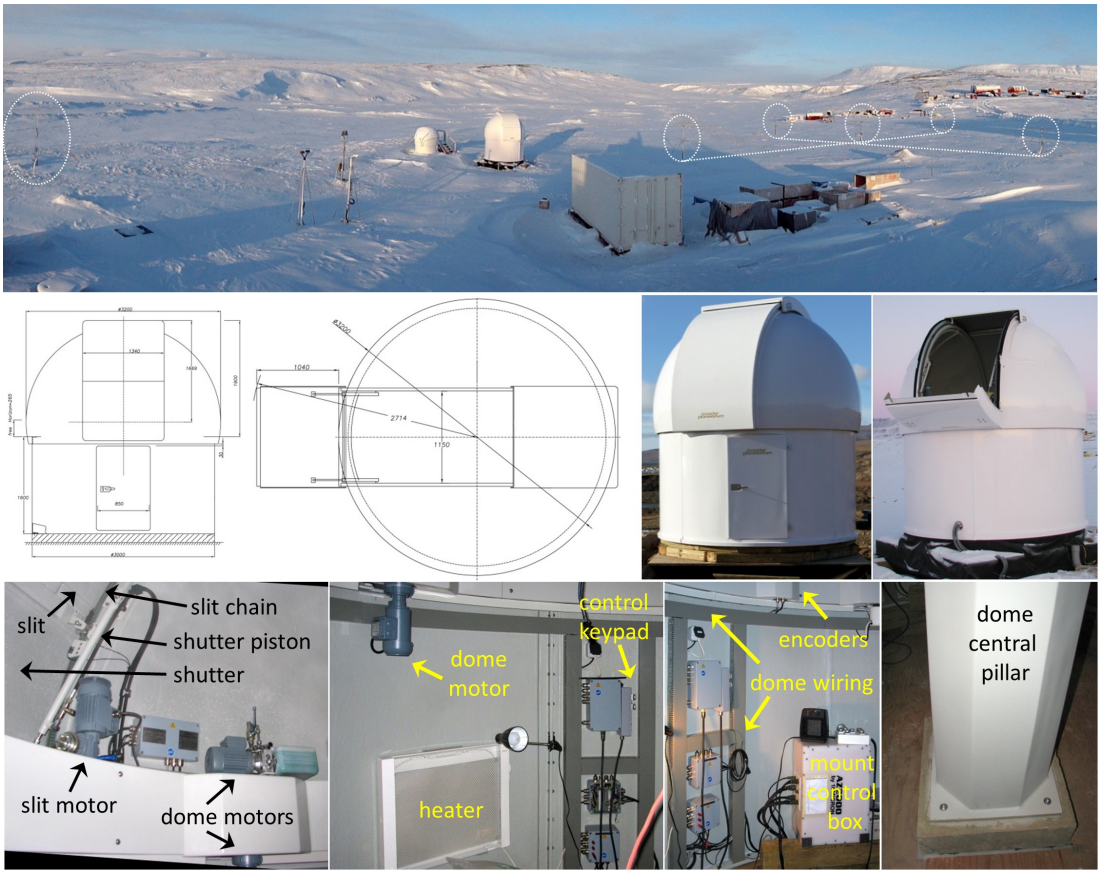

Figure 10: Star-photometer facility and dome details. Top: bird's eye view of the facility and surroundings, with white circles enclosing the nearby radar antennae. Middle: dome schematics and outside view. Bottom: inside the dome (slit, motors, control boxes, central pillar, heater etc.).

3. THE STAR-PHOTOMETER FACILITY

A bird eye view of the star-photometer facility and its surroundings is shown in the uppermost photo of Fig. 10, as seen from the roof of the 0PAL laboratory (Fig. 2). The main 3.2 m diameter dome was built especially for the Arctic by the German company Baader Planetarium. The sea-container in which it was housed for shipment to Eureka was thermally insulated before shipping, in order to use it as a control room afterwards. The facility still has a small, decommissioned, 7 ft Astrohaven clamshell dome, whose shell walls didn't survive the spring blizzards.

3.1 The dome

The manufacturer, Baader Planetarium, went through a lengthly learning process for developing domes in cold environments, like Antarctica and the Arctic. For temperatures down to $-55\,^{\circ}\mathrm{C}$, a classical, rotating dome, with shutter and an observational slit, was found to be a reliable solution. Bellow that temperature limit (determined by experience with a similar installation in Antarctica) the hydraulic systems cannot work and only a clamshell dome, made strong enough to withstand blizzards, will work. For the Eureka case, the hydraulic system works with a special, low temperature, aircraft oil.

The middle graphics of Fig. 10 shows the 3.2 m dome schematics and external views after the installation at Eureka (including the open shutter and slit). The dome is mounted on wood beams and has a wood deck floor. The bottom pictures show several views from inside the dome, emphasizing the slit, the motors, the heater, the wiring, the pillar etc. The central pillar, supporting the mount, the telescope and the instrument, is fixed on

a square concrete structure secured to the permafrost through the summertime melt layer. The pillar is not in contact with the dome, or deck structure, in order to ensure that dome vibrations will not affect the star pointing. The dome uses three phase motors which can be directly operated down to $-30\,^{\circ}$C, while employing efficient, pulse based, internal heating for temperatures from $-30\,^{\circ}$C to $-55\,^{\circ}$C. The shutter drive mechanisms (pistons) are made from stainless steel and employ an ultra low temperature grease. The slit opening is driven with a metal chain.

For dome sizes above 2.5 m diameter, an additional rotation motor is required to improve the ice breaking capability. The alternative of heating the ice away proved to be ineffectual under heavy icing conditions. First, the surface of the whole dome (even for small domes with < 2 m diameter) has too large a surface area for being permanently heated well above $0\,^{\circ}$C. Secondly, the melted ice and snow accumulate a few centimeters away from the heat source, making a hard ice crust. This blocks the moving mechanics even more than without heating. In addition, this affects potential infrared observations and generates unwanted local turbulence. The only solution was to make extremely smooth, highly polished surfaces on all the weather exposed dome parts, reducing the ice accumulation and allowing the break up of the ice without damaging the dome. In addition, an anti-sticking coating, similar to poly-tetra-fluoro-ethylene (PTFE), was applied. All of the commercially available coatings have specifications for room temperatures only. For most, their anti-sticking properties fail at $-50\,^{\circ}$C. In order to find an appropriate anti-stick coating, the manufacturer tested various coatings in its own $-86\,^{\circ}$C cold chamber, where it commonly tests all the dome parts and sub-systems.

Even with such a coating, ice accumulation may occur. For this reason, one uses over-sized heavy-duty motors, which can break the ice even at the slowest speed, just before starting the acceleration. For such a purpose, the standard wheel based rotation system is not strong enough and, for a big 3.2 m dome, one needs a tight power transmission between the motors and the dome. Therefore, a geared (toothed) drive, giving direct, slip free contact between motors and the dome rotation was found to be much more reliable. The drawback of this solution is however the need to perfectly synchronize all the motors. Using such a slip free geared dome, rotating on a giant toothed wheel, allows nevertheless the integration of absolute encoders. This adds much more reliability to the dome operation, since the real dome position is known under all circumstances, even after power interruption, or after heavy ice breaking events, when the dome may frequently run up against an ice barrier. These encoders also have to be thermally isolated and internally heated. All limit switches for the dome movements are magnetic based, rated at $-80\,^{\circ}$C, watertight and free of any mechanical contact to avoid ice blocking. Another important design innovation is the dome power bar with continuous contact in azimuth and rated at low temperature, for an endless rotation without any danger of breaking the cables.

The dome is made of a thermally insulating material, especially designed to withstand stress under cold conditions. This is a cold proof, brittle free, fiberglass reinforced polyester (FRP), in double layer design. Sandwiched between the layers is a 16 mm thick layer of hard polyurethane foam, which is certified for use in aircrafts, for withstanding years of vibrations and almost any amount of wind pressure, without becoming de-laminated. It's rated to support up to 10 kN/m^2 of ice load.

3.2 The telescope mount

After extensive testing in cold environments, an alt-azimuth (Alt-Az) mount, moving in altitude (elevation) and azimuth, proved to be more appropriate than the commonly used parallactic (German equatorial) mounts. Baader Planetarium, in collaboration with the company 10Micron, an Italian mount manufacturer, developed therefore the AZ2000 Alt-Az mount, specifically for polar environments (Fig. 11). Beyond the manual commands, it can also be controlled from a computer, through a serial link, with a virtual keypad, or any other custom made programs.

One main drawback of such a mount is the rotation of the field of view during the observations. This effect is due to the fact that the alt-azimuth pointing is not following the equatorial movement of the stars. For our case of star-photometry and spectroscopy, when only one star is observed at a time, the field rotation is not relevant. Even for cases when the field rotation matters, such a mount can still be used by employing a de-rotator. The Dobson's hole, covering 10-15$\,^{\circ}$ off zenith, is in principle another drawback, as the Alt-Az mount has difficulties accurately pointing in that direction. Again, for our application, as there is no stable bright star (magnitude < 3) in that area, the Dobson's hole is not an issue.

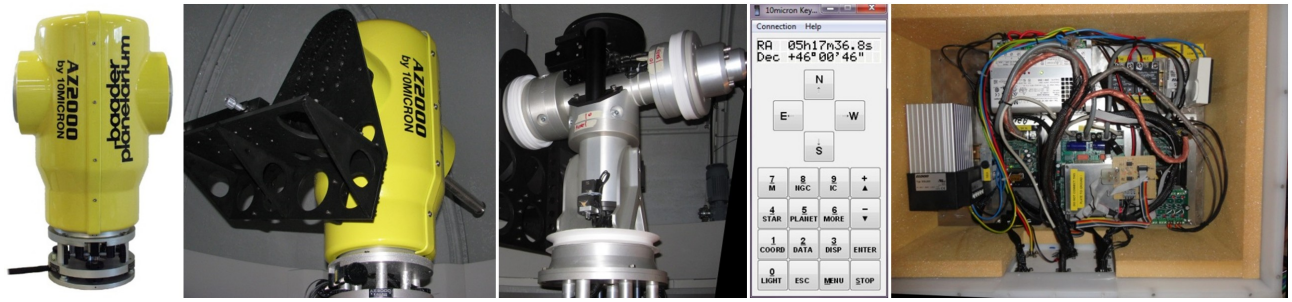

Figure 11: The AZ2000 star pointing mount in Eureka: with and without the insulating cover; virtual keypad; inside the mount/dome electronic box.

On the other hand, an Alt-Az mount easily enables the construction of an hermetically sealed, airtight insulated cover. It allows internal heating, while not allowing any warm air to escape and degrade the observations. This is mainly facilitated by the constantly vertical position of the mount, the white sealing ring, at the base of the mount (Fig. 11), will trap the warmer and less dense air inside. Also in this position, the mount cover applies a minimal stress to the ring. The sealing also protects against high humidity events for which condensation is particularly intense on the sharp parts, like the gears. All the sealing rings for the moving parts of the mount and dome are custom made from silicon and rated for temperatures below $-55\,^{\circ}$C. The cover is made from the same thermally insulating material as the dome, but with 10 mm thick foam, instead of 16 mm. It is therefore also able to support high ice loads and is coated with an anti-sticking material. The electrical appliances inside the cover serve to provide the necessary temperature gain, but there are also motor heaters and gear case heaters, to prevent backlash or an increased power consumption of the motors.

The basic mount alignment procedure is straightforward and can be performed by non-specialized personnel. A simple leveling session, combined with an azimuth synchronization is enough. In contrast, a classical equatorial mount needs to be perfectly polar aligned to avoid drifts during the star exposure. The classical Scheiner alignment method, based on correcting drifts which are proportional to the difference between Alt-Az and equatorial movements, fails near the poles. This is because those two types of movements are nearly the same near the poles and the pointing to the equator is affected by refraction. For relatively small telescopes, with the main mirror being less than 0.5 m diameter, one doesn't usually have a guider, tracking the telescope on an off-axis star. In such a case, being unable to make a good initial alignment, even very good correcting software has difficulties in achieving expected sub arc-second drift values. In addition, with equatorial mounts the telescopes can reach positions where one can hit the pillar. Also, the movement range in elevation is $180\,^{\circ}$, instead of $90\,^{\circ}$ as for an Alt-Az mount, leading to the risk of locked cables. Furthermore, the measuring instrument has only one rotational axis, reducing the time for controlling the balance and flextures.

Often overlooked is the very low air humidity prevailing at polar locations. There is weak electrical conductivity through the air and electrostatic accumulation and discharge are extremely likely. In this way, the usually sensitive electronic components can be damaged and there are rarely available spares in such remote locations. Unfortunately, the Arctic and Antarctic ground has a very low conductivity for a proper electrical grounding. All the electronic parts have to be electrically separated and protected with electromagnetic shielding. When out of operation, at very low ambient temperatures, the electronics have to be warmed up before powering up. Otherwise internal damage, due to shifted resistances, could occur. An internal temperature sensor then allows powering up only after the internal heating system raises the temperature to safe levels. Keeping the electronics warm is desirable even if not in operation. This is because the warm air can hold more moisture, avoiding the degradation, by electrolyte evaporation, of some electronic components, like capacitors.

If it's not possible to put the electronic equipment for controlling the mount and dome inside a heated control room, i.e. due to excessive length of cables, it has to be protected from the surrounding low temperatures inside a suitably insulated box. In Eureka, such a control box is installed inside the dome, (Fig. 10, second picture from right, bottom row, white box) and is resistant to long UV light exposures and temperatures down to $-60\,^{\circ}$C. The insulating material used is similar to the fiber glass (used in space applications), and will not easily crack

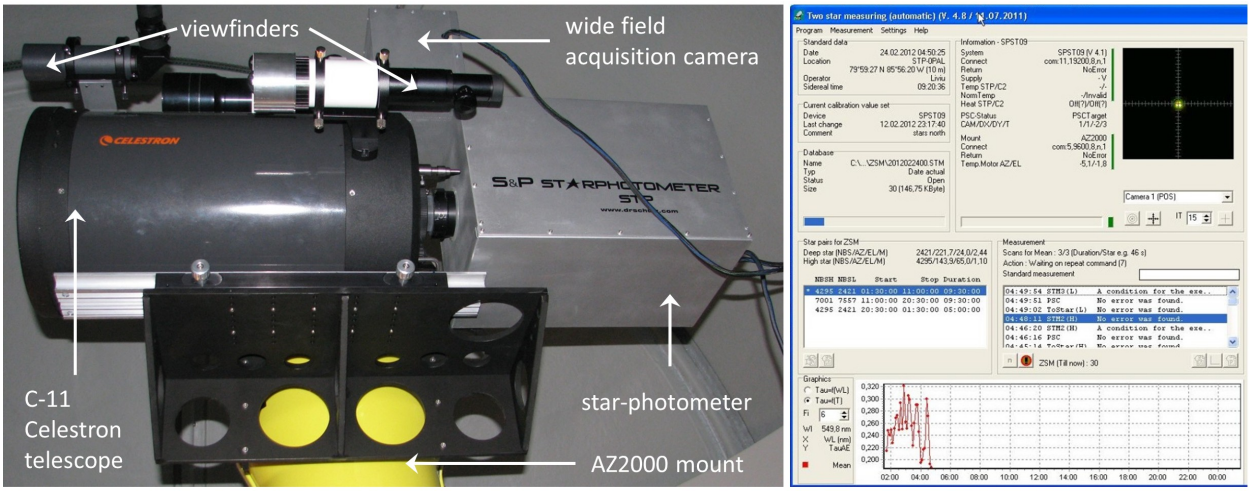

Figure 12: Left: star-photometer installed in Eureka. Right: software control panel for star acquisition and measurement control.

under stress, even down to −80 °C (Fig. 11, last picture). This also allows a good sealing to avoid any outward flow of warm air to degrade the observations. The main issue with being able to warm up such an insulated box is surprisingly not the heating. A small (sub 100 W) heating system is capable of keeping all the components above 0 °C. Heating that relies on air temperature conductivity is not efficient in dry air. Therefore an internal fan it's required, but without greased bearings to avoid out-gazing.

All the cables have to be rated for low temperature, as the standard PVC would break in a very short time, especially under conditions of permanent movement such as occurs inside the mount. For temperatures down to −60 °C, silicon mantled wires are suitable, while for Antarctic conditions the PTFE mantled wires are the only remaining solution. The cables, especially the long ones, making the link between different equipments, also have to be shielded to avoid electromagnetic cross-talk between different instruments. All the metal parts have to be made from brittle and corrosion free alloy, especially when used below −55 °C. Facilities for atmospheric observations at coastal sites, such as Eureka, can be particularly affected by corrosion during the open water summer season. Equipment made for standard temperatures would usually jam in Arctic or Antarctic conditions. Therefore, all the moving parts exposed to ambient temperatures have to be free of any temperature sensitive components, like belts. All the gears, bearings and fittings are designed to tolerate the expected low temperatures. If absolutely necessary, inside gears or bearings one uses only a grease rated for very low temperatures. Such items, normally used for space applications, are extremely expensive.

In case of a power outage, the manufacturer has made available a custom made, car battery based UPS for emergency closure of the dome, which is able to keep the electronic components warm. However, we don't use this system in Eureka, inasmuch as the batteries are difficult to maintain there. We simply rely on the fact that the Eureka station has to solve the power outage within 12 h anyway.

3.3 The telescope and instrument

In Eureka we currently use a Schmidt-Cassegrain C11 Celestron telescope, appropriate for narrow field of view observations, with an aperture of 280 mm, a focal length of 2800 mm and a weight of 14 kg (Fig. 12, left). The corrector plate, as entry window, is particularly useful to prevent the snow from entering the telescope tube.

The star-photometer (Fig. 12, left), built by the German company Dr. Schulz & Partner, is built around the QE65000 scientific-grade spectrometer made by Ocean Optics. It has a 0.7 nm resolution, covering the range 399.1 - 1159.3 nm. In practice one uses only 17 wavelengths (channels): 419.9, 450.2, 469.2, 500.2, 531.7, 549.8, 605.4, 639.7, 676.1, 750.7, 778.9, 862.3, 933.5, 943.2, 952.8, 1026.0 and 1040.7 nm, with a spectral bandwidth (FWHM) <6 nm. The detector is a Hamamatsu S7031-1006 CCD, with 1044 × 64 pixels, each with a detection surface of 24.6 μm^2. One usually works on stars brighter than visible magnitude 3.

Figure 13: The sea-ship container transformed into a control room: cable protection and precipitation and temperature sensor; inside the control room; dome/mount high voltage unit; inside the unit.

The star-acquisition procedure is based on subsequent acquisitions on two auxiliary SBIG ST-402ME-C2 CCD cameras. It first uses a wide field external camera (Fig. 12, left), having it's own little telescope, on top of the star-photometer. This camera has a 57.4' (arc-minutes) field of view (FOV), at 20.5"/px (arc-seconds per pixel), is thermally insulated and has an internal heater controlled by the main instrument. Once the star is centered in this camera, the acquisition is taken over by a high angular resolution internal camera with 8.3' FOV, at 3"/px. Inside the photometer the light is split with 10% going to the acquisition camera and 90% to the spectrometer, the latter being fed by an optical fiber with a 60" FOV.

The instrument, weighing 13 kg, is thermally insulated and has internal heating, allowing operation down to $-80\,^{\circ}$C. It has an internal temperature sensor preventing power up before the internal temperature reaches a safe level (usually over $0\,^{\circ}$C). It's controlled, by a custom made graphical interface (Fig. 12, right), through a serial link from a laptop located in the control room. Beyond data acquisition procedures, the software enables control of the focus and control of the mount, which in turn controls the dome movements.

The measurements are done by taking alternative exposures on star and sky background. If properly calibrated, optical depth of atmospheric particles can be extracted, with 3 minutes resolution, by observing only one star in any sky transparency conditions (using a retrieval based on the Bouger-Beer-Lambert law of starlight attenuation). The second means of estimating optical depth is to measure alternatively a high and a low elevation star. This procedure, unlike the single star method, doesn't require calibration. It does however require a uniformly transparent sky and it increases the time resolution to about 6 minutes. One expects an optical depth accuracy $\sim$0.01 or larger.[35]

3.4 The control room

The thermally insulated sea-shipping container, is equipped with a specially made cable entry, and makes a very handy control room. This latter feature optimizes the use of sea-tainers and avoids the costly construction of control rooms on site (Fig. 10, the uppermost photo). At every corner of the sea-tainer control room, a rod was inserted in the ground, for electrical grounding. The room is supplied with electricity and has a wired internet link with the nearby 0PAL laboratory. On the outside wall, it has an integrated precipitation sensor for automatically closing the dome. Inside (Fig. 13), there is an integrated heater and a white steel unit hosting the high power controls of the dome and mount. We installed two desks for operator convenience. There is also an IP phone with cordless handsets and a walkie-talkie.

4. OPERATING CHALLENGES

The first Eureka star-photometry observations in 2007,[17] were more of an exploratory testing of the system. The star-photometer instrument was designed for the Arctic, but the G-11 equatorial Losmady mount and the currently abandoned dome, were obviously not. The frequent equipment failures were mitigated by constant human intervention, that often put the operators health and security in danger. Without a control room, the operators had to work in shifts in the little open clamshell dome, making observations at temperatures down

to $-50\,^{\circ}$C and exposed to winds as well as to the dangers of roaming wolf packs. The equipment didn't allow remote or unattended observations and the aforementioned difficulties prevented the CANDAC operator on duty from continuing the observations after the servicing team left the station. Therefore, it was a period of high maintenance costs and low productivity. The current dome, mount and control room, installed in 2010, made a huge improvement in the reliability of the operation and data productivity. Nevertheless, the Arctic still gave us a number of challenges that we had to address.

First, the sea-ship container control room, while handy, had some drawbacks. It was only possible to completely close the door from the outside and there was no window to see where the telescope was pointing. So, one often had to go outside for checks. This was inconvenient, especially during the installation and initial alignment phases since the inside temperature could become quite cold. The open door also raised a polar bear security issue and we were forced to install a heavy duty chain and hook. On the other hand, if the door is closed (from outside), it almost seals the container. Due to problems in controlling the heating within the container, the temperature could rise to levels that were problematic for the equipment. In addition, the over-heating could increase the air pressure to such high levels that opening the container could be physically dangerous. To prevent such a problem, we installed a thermostat on the heating system, which cut off when the temperature was greater than $+15\,^{\circ}$C and also a remotely readable (over the internet) thermometer, as a secondary check.

The entry for cables, that initially was able to accommodate twice as many cables as necessary for the mount and dome, slowly reached its capacity, after adding more auxiliary equipment. In addition, that entry was not well protected against animals and the result was damaged cables caused by a musk ox (Fig. 9 "broken cables"). A big, wooden box was then installed to protect the cables (Fig. 13, left). The precipitation sensor measures the conductivity of melted snow that is deposited on it. As the snow in Eureka is generally so light and the sublimation of melted snow so high, the conductivity never increases enough for the sensor to detect it. Near the precipitation sensor, we also installed a high temporal resolution, air temperature sensor. In the fall or spring, the container absorbs the sun energy faster than the environment. Its close proximity to the sensor means the temperature data is not representative of the surrounding air.

To get reliable real-time weather parameters, we bought a Zeno-3200 automatic weather station, especially built for the Arctic by Coastal Environment Systems. Its deployment at Eureka was delayed by funding and logistical constraints. The station is currently deployed in Sherbrooke, providing measurements of pressure, temperature, relative-humidity, precipitation or frost presence, wind speed and direction. The data is recorded with sub-minute resolution and a down-sampled version is plotted on-line in real-time, over the internet. Inasmuch as the funding and logistical issues are largely resolved, we expect to moved it soon to the Arctic.

The laptop controlling the star-photometer, is a 1501 Inspiron from Dell, with a Windows XP operating system. It was surprising to see that, if started inside, at room temperature, it kept working outside, down to $-40\,^{\circ}$C. In the cold, the external laser based mouse soon stopped working, but the integrated touch-pad was functional, as was the hard disk. The touch-pad had however to be controlled with special touch-pad gloves, with conductive material on the tip of the fingers. Using the bare fingers in such a deep cold and dry environment causes cold burn and dry skin, which may take weeks to heal. On the other hand, the laptop battery didn't survive the cold. We are now contemplating replacing the laptop with a semi-rugged CF-53 Panasonic model, having a solid state drive (SSD) (no moving parts). It will be based on Windows 7 Ultimate or Windows 8, in order to provide the capability for sending microphone sound over a remote desktop connection.

The electricity provided at Eureka is three-phase 120 V. Our systems (dome, mount, star-photometer, heaters) are distributed between the two phases that are provided at the container. Over-loading one of them could trigger off the fuse, putting the equipment at risk. Such an eventuality would require human intervention, which is not always readily available. To avoid such a situation, we didn't rely solely on the manufacturer's power consumption specifications when assigning the load distribution. This is because one may have out of spec high loads, for short periods of time, especially at start up. We therefore measured the load on each phase at 6 s time resolution. For the overall power consumption, we found 1.3 kW in normal operation, with a peak of 2 kW at start up. In "sleep" mode, when one basically only keeps the equipment warm with moderate heating of the dome, power consumption is about 1 kW. As the fuses accept a total limit of about 3 kW, the load distribution is essential and one has to make sure that dome heating is off in the operating mode. From the cost perspective, the electricity consumption requires about 50$/day.

One of the most annoying aspects, which in the last four years cost us more than half of the observational time and uncounted effort and money, was the electromagnetic interference (EMI) issue. As one can see in the Fig. 10, the star-photometer facility is located between a meteor radar emitter antenna (on the left, encircled in white) and an array of five reception antennae (on the right, also encircled in white). The dome and mount, operating at 400 V AC, 50 Hz, with pulse motor heating, and using step up transformers, practically destroyed the 33 MHz meteor radar reception, especially the signal of the nearest antenna. This problem mainly related to the fact that one cannot make a proper electrical grounding to filter the residual oscillations. Drilling deep into the permafrost, to install a grounding rod, is almost impossible (usually breaking the drill bit). We installed split ferrite cores on all the wires, and also used high performance filters to filter out any frequency close to 33 MHz, especially from the power lines and high voltage controllers, all without success. For identifying the EMI sources, we tried to turn on one sub-system at the time, but due to their interdependence and the non-reproducibility of the perturbations, it was impossible to localize and solve the issue. We even tried oscilloscope measurements and using handy devices with reception antennae to localize EMI sources ("Electrosmog RF Microwave Meter TES-593"), again without success. Trying to minimize the impact on the radar, we reduced the dome motor heating. Since the motors need heat below $-40\,^{\circ}$C, this caused dome problems, with episodes of hard dome rotation and the slit refusing to close in the mornings. We also tried moving the nearest and more affected radar antenna. While looking promising during the summer, once the cold and snow cover came back, so too did the EMI interference issue. A temporary solution was to work in shifts, on a 36 hours basis for each instrument. However, without continuity the radar data was significantly compromised. Also, many interesting cloudy events were missed by the star-photometer. As a last resort, the meteor radar will be completely moved soon to a remote new location.

Another annoying aspect was the fact that the star-photometer stopped working, several times per day. As this never happened during the tests at the manufacturer location, we suspected that it was also suffering from the grounding issue or the EMI perturbations. The only solution to bring the photometer back on-line was to re-start it. However, doing frequent power cycles below $-40\,^{\circ}$C it's a recipe for disaster. We lost, in this way, two spectrometers, two SBIG cameras, the internal computer and the memory card, resulting in additional costs and time lost for repairs. The dome/mount control box (Fig. 11, last picture) also had to be repaired once, the damage probably having been caused by electrostatic discharges. One motor, the homing and temperature sensors also died inside the mount. To diminish the impact of the time and cost for repairs, we now have spare parts for almost every electronic component or board.

The Arctic environment is also challenging in terms of observational data, by virtue of background signal contributions (any signal, whether instrumental or environmental which is not related to star irradiance attenuation). Star-photometer controlled heating will, for example, not always keep up sometimes with the cold below $-40\,^{\circ}$C. This affects the read out current, and implicitly the retrieved background level. Another example was the presence of small spikes in the background signal that are suspected to be due to stray light reflections from ice crystals in the air. Also, being near the magnetic pole, we're more exposed to solar storms: we know of at least one event that raised the background signal levels to unusually high values.

Despite all the design precautions, the star-photometer also had an issue with an oily substance (Fig. 14, left) condensing on the inside walls of the photometer box and its entry window (the colder parts). This was probably due to the evaporation of the adhesive used for the heating plates (evaporation which is expected in dry air conditions). Beyond reducing the star radiance entering the photometer, this optical degradation changes the calibration, affecting the OD results in the one star mode. We are now investigating a different technique for affixing the heating plates inside the photometer.

The most troubling feature of the sea level Arctic environment is the optical degradation induced by the frequent ice crystals deposition on the telescope entry window (Fig. 14). Among the different ice crystal types, the most difficult to handle is the frost or rime icing (a similar phenomenon occurs in Antarctica[7]). It's probably due to super-cold semi-transparent fog usually found at sea level, adhering to the window in an amorphous state. It is difficult to remove even by manual intervention. Sometimes, one notices a diffuse appearance even in the inside of the telescope window. This is probably due to a bit of frost during a rare event of relatively higher air moisture. Another deposition type is clear sky snow, depositing crystals of various habits and levels. Using a heated dew cap is not a good preventive solution, because it induces local turbulence and tends to accumulate

Figure 14: Left, photometer entry window: oil condensed on entry window. Next pictures, telescope entry window: rime icing (frost) and various deposition levels of precipitating ice crystals. Last one: after 2 h of clear sky snow.

the snow inside. There is however a relatively simple maintenance solution: during non-observing periods, the icy deposition sublimates almost completely in few hours, especially if one heats the dome a bit. The ice crystal deposition compromises the utility of the nominal instrument calibration and affects the OD results in the one star mode. This is an important drawback for TIC observations when one usually doesn't have uniform sky, while the very act of being in the presence of TICs means ice crystal precipitation is likely to be occurring.

The possibility of moving the star-photometer facility up to the PEARL Ridge Lab is currently being considered. Being warmer, there should accordingly be fewer problems with the temperature protection of the equipment. At the Ridge Lab one avoids the exhaust of the diesel generators, the sea level fog, low laying ice crystals as well as blowing crystals. The lesser turbulence and scintillation should speed up the star acquisition process. On the other hand, one will forfeit the relative convenience of the 0PAL site.

5. REMOTE OPERATION

Due to all the aforementioned issues, the star-photometer operation needed constant supervision. Inasmuch as the CANDAC operator on duty had to take care of more than 25 instruments, his involvement on a regular basis was not an option. Therefore, soon after the installation, we started upgrading the facility, in order to replace all the manual commands with remote controls over the internet. When CANDAC stopped having a constant operator on site, in March 2012, this became a necessity. Even in the current improved funding situation, the new CANDAC policy is to shift all the operations towards a remote or automatic control.

5.1 Remote control

Normally, all the systems should remain powered on, even in the non-observing mode. This is to ensure that they remain warm, safe and ready for a new observation session, as soon the sky is clear enough to acquire the stars. However, as one needs to re-start the star-photometer when it stops working or to turn off/on the mount and dome to allow unperturbed radar operation, we added remote functionalities. We used an IP9258 (an IP based power bar) for internet control of the 120 V power on the star-photometer, the light and air blower (part of the maintenance kit), the mount and dome, and the dome heating (Fig. 15). More recently we replaced it with an IP bar having more sockets.

For performing low voltage operations over the internet, we used an X-300 webrelay (Fig. 15), to control the boot (reset) of the star-photometer, the mount, the dome and the laptop. The laptop was wired internally, and the star-photometer was modified, to remotely control its reset button. This device also controls the temperature sensors from inside and outside the control room. The real-time and historical temperature values are also plotted on the CANDAC website, along with temperatures from all other facilities. Actually, CANDAC also transfers the star-photometer observational data from the laptop to a server in Toronto over the night.

The mount/dome and star-photometer are remotely controlled through graphical interfaces from the laptop, using the Windows program "Remote Desktop Connection". Versions of this program exist even for smart phones, so one can perform remote control scenarios from anywhere. Although this is a high bandwidth operation, the CANDAC link is generally able to accommodate it. Since we had no real-time feed-back from the mount and dome, we installed a microphone in the dome. It proved to be a very useful tool, allowing one to know if the telescope and dome moved on command, and to have an auditory feed-back on the wind intensity. We will be

able to use it in remote operation with a future laptop, as the microphone sound is enabled for remote connection only in Windows 7 Ultimate or Windows 8.

Without a direct view to the dome, it is difficult to operate the facility locally, from the container. Operating it remotely without any visual feedback is almost impossible. Therefore we installed two web-cams. A TRENDnet normal webcam is installed inside the nearby 0PAL laboratory. It gives a view of the dome, providing feedback on the pointing direction, the slit opening and closure and the sky brightness or cloudiness. The street lights from 0PAL and the fuel storage park allow one to observe the dome operations at all times. Another webcam, a StarDot "NetCam SC 1MP Day/Night Internet Camera", was installed inside the dome, as part of the maintenance kit. This camera can withstand temperatures down to $-50\,^{\circ}\mathrm{C}$ (even if it's rated at $-40\,^{\circ}\mathrm{C}$), without any heating. It provides visible (in color) and infrared (in black and white) views, for nighttime monitoring of the telescope position. It permits verification of the remote maintenance operations, the boot sequence on the star-photometer LEDs, and gives feedback on the wind strength by looking at the red ribbon attached to the empty arm of the mount (Fig. 15).

If performed for an extended period of time, the remote control of the starphotometer by a single operator becomes an extenuating task. He must remain awake during the nightime measurement period, performing observations, regularly monitoring the instruments as well as carry out certain tasks during the daytime. Bad weather events can provide a break, but a better solution was to have two operators, working in shifts. When the nighttime becomes shorter, like in October or March, the start of measurements approaches midnight, while the stop is at 3-4 o'clock in the morning. In such a situation, it was particularly useful that we had a second operator in Europe, able to stop the measurements at normal morning hours there.

Since the star-photometer may stop from time to time, one has to check back frequently, while being careful to not use excessive bandwidth. In order to limit this operation, we made C-shell .bat program to check the data acquisition archive on the star-photometer laptop. If its size doesn't increase as expected, it automatically sends an email to the operator. Such an approach enabled the operator to sleep during the observations, being woken up only when intervention is required. In this way a single operator can handle all the remote operations. In the case of an iPhone, one sets up the email address used by the program (here, the operator's own address) as the only VIP contact. Then, if one disables all notifications, except those from VIP contacts, one can be sure that only the star-photometer wakes up the operator. The Eureka station provides online standard, hourly weather conditions (metars). The station actually takes more frequent measurements, as required by Navcan (the organization controlling the aviation traffic in Canada), especially when the weather changes significantly. For a more frequent update on observing conditions it is therefore better to interrogate such metars, with tools like "Metar Weather". There are also online tools for sending metar alerts, like aviador.es. For example, one can set up an email notification in case of wind speed larger than a given threshold.

5.2 Remote maintenance

Since ice crystal deposition on the telescope entry window appeared to be an almost omnipresent feature, we searched for ways to eliminate this problem other than requiring a time consuming cleaning operation by the operator on duty at Eureka. We installed a 300 CFM air blower ("A300 Power Cat Portable Blower") and a light projector. They are activated/disabled from the IP power bar, while StarDot camera remains active at all times. Together, they made a successful remote maintenance tool for regularly removing precipitating or blowing ice crystals. This technique had, however, little effect on frost accumulation. One can only sublimate the frost by remotely activating the dome heating during non-observing periods.

Even with remote maintenance, the constant deposition of crystals, even in small quantities, degrades the star-photometer calibration and affects the optical depth results. A much better solution would be to prevent the crystals from depositing there in the first place. A new blade-less fan from Dyson appears promising in terms of forcing a deflective air curtain around the telescope. While this set up is not yet ready for continuous operation in the Arctic, the first tests were encouraging (Fig. 15).

6. CONCLUSIONS

We went through a challenging learning period, spanning over seven years, in order to be able to perform star-photometry observations at sea level in the High Arctic. This work incurred high costs and presented logistical

Figure 15: Remote maintenance kit (air blower, light projector, Vis/IR webcam); webcam views (from dome & 0PAL); online panels for remote operations; testing Dyson blade-less fan.

challenges that could not have been overcome without the support of CANDAC and Environment Canada. The sea-level Eureka station is among the coldest places in the Arctic, with strong sea level turbulence and omnipresent ice crystals. The poor conductivity of the permafrost makes electrical grounding unworkable and leads to cross EMI perturbations between different instruments. Trying to overcome such conditions, pushed the instruments and the facility beyond the initial specifications. Consequently, we had equipment failures followed by repair periods, eventually improving the design whenever possible. Overall, during the last four years, we managed to acquire about three months worth of data. By comparison with the previous facility, which was not well prepared for the Arctic, there were merely a few hours of data over a three year period. As we gradually improved our operations and the readiness of the equipment for the Arctic, and as we make further refinements such as the transfer of the meteor radar to a more distant location, the perspective to further improve the data productivity appears to be promising. In the long term, the relocation of the facility to the Ridge Lab should improve the perspective even further.

The main remaining technical problem is to mitigate the issue of ice crystal deposition, in order to obtain reliable optical depth values. This affects manly the one star measurement mode, required in case of cloudy events. The two star mode is independent of crystal deposition and is appropriate for observations in uniform sky conditions, like aerosol scenes. The Dyson blade-less fan seems promising and the eventual Ridge Lab relocation may help to reduce ice crystal presence. In the mean time, one may still use data contaminated by ice crystal deposition in a differential manner, providing optical depth rates, useful for interpreting cloud evolution.

Summing up, precise photometric observations of stars at sea level, in the Arctic, might only be possible a few days per winter, when there is a very low amount of ice crystals in the air. The use of a blade-less fan may improve this situation. However, the fact that one may not know if the observation period was continuously crystal-free, may have an influence on the data quality. Probably the only real solution is to have the facility installed at a high elevation.[32]

ACKNOWLEDGMENTS

This work has been supported by the Canadian Network for the Detection of Atmospheric Change (CANDAC) and by the NSERC CREATE Training Program in Arctic Atmospheric Science. Special thanks are due to Jim Drummond, Pierre Fogal and Eureka Weather Station team for extensive technical and logistical support, to Eric Steinbring for stimulating discussions on this project, and to Chris Meek and Pierre Martin-Cocher for helping on the radar interference issue.

REFERENCES

[1] Wood, F. B., Chen, K. Y., and Giovane, F., "South Pole astronomical observatory," *Antarct. J. United States* **19**(5), 237–238 (1984).

[2] Chen, K. Y., Oliver, J. P., and Wood, F. B., "Stellar photometry with the South Pole optical telescope," *Antarct. J. United States* **22**(5), 283–284 (1987).

[3] Marks, R. D., Vernin, J., Azouit, M., Manigault, J. F., and Clevelin, C., "Measurement of optical seeing on the high antarctic plateau," *Astron. Astrophys. Suppl. Ser.* **134**, 161–172 (Jan. 1999).

[4] Storey, J. W. V., "Astronomy from Antarctica," *Antarct. Sci.* **17**(04), 555–560 (2005).

[5] Mark R. Swain and Hubert Gallée, "Antarctic Boundary Layer Seeing," *Publ. Astron. Soc. Pacific* **118**, 1190–1197 (Aug. 2006).

[6] Yuan, X., Cui, X., Liu, G., Zhai, F., Gong, X., Zhang, R., Xia, L., Hu, J., Lawrence, J. S., Yan, J., Storey, J. W. V., Wang, L., Feng, L., Ashley, M. C. B., Zhou, X., Jiang, Z., and Zhu, Z., "Chinese Small Telescope ARray (CSTAR) for Antarctic Dome A," in [*Proc. SPIE*], **7012**, 70124G–70124G–8 (2008).

[7] Strassmeier, K. G., Agabi, K., Agnoletto, L., Allan, A., Andersen, M. I., Ansorge, W., Bortoletto, F., Briguglio, R., Buey, J.-T., Castellini, S., Coudé du Foresto, V., Damé, L., Deeg, H. J., Eiroa, C., Durand, G., Fappani, D., Frezzotti, M., Granzer, T., Gröschke, A., Kärcher, H. J., Lenzen, R., Mancini, A., Montanari, C., Mora, A., Pierre, A., Pirnay, O., Roncella, F., Schmider, F.-X., Steele, I., Storey, J. W. V., Tothill, N. F. H., Travouillon, T., Vittuari, L., and Weber, M., "Telescope and instrument robotization at Dome C," *Astron. Nachrichten* **328**, 451–474 (July 2007).

[8] Macdonald, J., [*The Arctic sky: Inuit astronomy, star lore, and legend*], Royal Ontario Museum (1998).

[9] Jancik, J., Richardson, J., and Gardiner, S., [*Under the Midnight Sun: The Ascent of John Denver Peak and the Search for the Northernmost Point of Land on Earth*], Starsend Creations; First Edition (2002).

[10] Roscoe, H. K., Jones, R. L., Freshwater, R. A., Fish, D., Wolfenden, R., Harries, J. E., and Oldham, D. J., "A star-pointing UV-visible spectrometer for remote sensing of the stratosphere," in [*Proc. SPIE, Opt. Methods Atmos. Chem.*], **1715**, 374–380 (1993).

[11] Leiterer, U., Naebert, A., Naebert, T., and Alekseeva, G., "A new star photometer developed for spectral aerosol optical thickness measurements in Lindenberg," *Contrib. to Atmos. Phys.* **68**(2), 133–141 (1995).

[12] Ivanescu, L., "Arctic Astronomy," in [*Proc. SPIE Abstr. 4836-30*], **4836** (2002).

[13] Ivanescu, L., "Arctic Astronomy," *ESO Espas Libr. @ scribd.com* , 11 (2003).

[14] Blake, M., Vaduvescu, O., and Fingerhut, R., "A Canadian Modest Aperture Telescope," *Cassiopeia* (116) (2003).

[15] Steinbring, E., Carlberg, R., Croll, B., Fahlman, G., Hickson, P., Ivanescu, L., Leckie, B., Pfrommer, T., and Schoeck, M., "First Assessment of Mountains on Northwestern Ellesmere Island, Nunavut, as Potential Astronomical Observing Sites," *Publ. Astron. Soc. Pacific* **122**(895), 1092–1108 (2010).

[16] Steinbring, E., Millar-Blanchaer, M., Ngan, W., Murowinski, R., Leckie, B., and Carlberg, R., "Preliminary DIMM and MASS Nighttime Seeing Measurements at PEARL in the Canadian High Arctic," *Publ. Astron. Soc. Pacific* **125**(929), 866–877 (2013).

[17] Baibakov, K., O'Neill, N., Herber, A., Ritter, C., Schulz, K.-H., and Schrems, O., "Starphotometry at two High Arctic stations," in [*Geophys. Res. Abstr.*], **13**, EGU2011–892 (2011).

[18] IPCC, "Climate Change 2013: The Physical Science Basis, Contribution of Working Group I," in [*Fifth Assess. Rep. Intergov. Panel Clim. Chang.*], Stocker, T. F., Qin, D., Plattner, G.-K., Tignor, M. M., Allen, S. K., Boschung, J., Nauels, A., Xia, Y., Bex, V., and Midgley, P. M., eds., 1535, Cambridge University Press, Cambridge, United Kingdom and New York, NY, USA (2013).

[19] MSC, "Welcome to the Eureka Weather Station: a visitor's guide to Eureka," tech. rep., Environment Canada (2010).

[20] Allard, G., Barnard, C., and Sarrazin, D., "Ward Hunt Island Observatory Research Station, User's Manual," tech. rep., CEN Research Station Network (2013).

[21] Rytír, M., *Radiowave Propagation at Ka-band (20/30 GHz) for Satellite Communication in High-Latitude Regions*, PhD thesis, Norwegian University of Science and Technology (2009).

[22] Grenier, P., Blanchet, J.-P., and Muñoz Alpizar, R., "Study of polar thin ice clouds and aerosols seen by CloudSat and CALIPSO during midwinter 2007," *J. Geophys. Res. Atmos.* **114**, D09201 (May 2009).

[23] Chernoff, D. I. and Bertram, A. K., "Effects of sulfate coatings on the ice nucleation properties of a biological ice nucleus and several types of minerals," *J. Geophys. Res. Atmos.* **115**(D20) (2010).

[24] Eloranta, E. W., Garcia, J. P., Razenkov, I. A., Uttal, T., and Shupe, M., "Cloud Fraction Statistics Derived from 2-years of High Spectral Resolution Lidar Data Acquired at Eureka, Canada," in [*24th Int. Laser Radar Conf.*], 4 (2008).

[25] Shupe, M. D., Walden, V. P., Eloranta, E., Uttal, T., Campbell, J. R., Starkweather, S. M., and Shiobara, M., "Clouds at Arctic Atmospheric Observatories. Part I: Occurrence and Macrophysical Properties," *J. Appl. Meteorol. Climatol.* **50**, 626–644 (Nov. 2011).

[26] Ivănescu, L., Spann, R. A., and Erasmus, D. A., "Satellite Study for TMT," tech. rep., SAAO, Cape Town (2007).

[27] Serreze, M. C., Box, J. E., Barry, R. G., and Walsh, J. E., "Characteristics of Arctic synoptic activity, 1952–1989," *Meteorol. Atmos. Phys.* **51**(3-4), 147–164 (1993).

[28] Asada, K., Martin-Cocher, P. L., Chen, C.-P., Matsushita, S., Chen, M.-T., Huang, Y.-D., Inoue, M., Ho, P. T. P., Paine, S. N., and Steinbring, E., "Opacity measurements at Summit Camp on Greenland and PEARL in northern Canada with a 225 GHz tipping radiometer," in [*Proc. SPIE*], **8444**, 84441J–84441J–10 (2012).

[29] Butler, B., "Precipitable Water at the VLA 1990-1998," *Alma Memo Ser.* (Memo 237), 8 (1998).

[30] Otárola, A., Travouillon, T., Schöck, M., Els, S., Riddle, R., Skidmore, W., Dahl, R., Naylor, D., and Querel, R., "Thirty Meter Telescope Site Testing X: Precipitable Water Vapor," *Publ. Astron. Soc. Pacific* **122**, 470–484 (Apr. 2010).

[31] Lynch, D. K., "Cirrus clouds: Their role in climate and global change," *Acta Astronaut.* **38**, 859–863 (June 1996).

[32] Law, N. M., Carlberg, R., Steinbring, E., Ngan, W., Sivanandam, S., and Maire, J., "New results from the first exoplanet survey in the Canadian High Arctic," in [*Proc. SPIE*], **9145** (2014).

[33] Okamoto, H., Sato, K., and Hagihara, Y., "Global analysis of ice microphysics from CloudSat and CALIPSO: Incorporation of specular reflection in lidar signals," *J. Geophys. Res. Atmos.* **115**, D22209 (Nov. 2010).

[34] Borovoi, A. G., Burnashov, A. V., and Cheng, A. Y. S., "Light scattering by horizontally oriented ice crystal plates," *J. Quant. Spectrosc. Radiat. Transf.* **106**, 11–20 (July 2007).

[35] Herber, A., Thomason, L. W., Gernandt, H., Leiterer, U., Nagel, D., Schulz, K.-H., Kaptur, J., Albrecht, T., and Notholt, J., "Continuous day and night aerosol optical depth observations in the Arctic between 1991 and 1999," *J. Geophys. Res. Atmos.* **107**, AAC 6–1–AAC 6–13 (May 2002).

Chapter 2

Accuracy in starphotometry

Foreword

Core article of the thesis, to be submitted to Atmospheric Measurement Techniques (AMT)!

Accuracy in starphotometry

Liviu Ivănescu[1,2], **Konstantin Baibakov**[1,3], **Norman T. O'Neill**[1], **Jean-Pierre Blanchet**[2], **and Karl-Heinz Schulz**[4]

[1]Centre d'applications et de recherches en télédétection (CARTEL), Université de Sherbrooke, Sherbrooke, QC, Canada
[2]Department of Earth and Atmospheric Sciences, Université du Québec à Montréal (UQÀM), Montréal, QC, Canada
[3]Flight Research Laboratory, National Research Council, Bldg. U-61, 1920 Research Rd, Ottawa, ON, Canada
[4]Dr. Schulz & Partner GmbH, Falkenberger Str. 36, Buckow, Germany (end of operations as of April 2016)

Correspondence: Liviu Ivănescu
(Liviu.Ivanescu@usherbrooke.ca)

Abstract. Starphotometry, the nighttime counterpart of sunphotometry, has not yet achieved the commonly sought observational error level of 1% (a spectral optical depth error level of 0.01). In order to address this issue, we investigate a large variety of systematic (absolute) uncertainty sources. One of the design requirements to achieve this end is a Field of View of $45''$. The characterization of spectral drift indicated that a spectral calibration of spectrometer based starphotometers should be made annually. A set of 20 channels are identified to mitigate contamination errors associated with stellar and terrestrial-atmospheric gas absorption, as well as aurora and airglow emissions. In addition, various observation recommendations are presented. The bright star catalog of extraterrestrial references is noted as a major source of errors with an attendant recommendation that the accuracy of such catalogs be significantly improved. We noted the significant effects of snow crystal deposition on the starphotometer optics, how pseudo OD increases associated with these contaminations could be detected and how proactive techniques could be employed to avoid their occurrence in the first place. The small FOVs employed in starphotometry ensure that this technique is only weakly dependent on the intrinsic and artificial OD reduction induced by scattering into the FOV by optically thin clouds. The importance of monitoring sky background and using interpolation techniques to avoid spikes was underscored. We also note that observations for starsphotometers similar to our high-Arctic starphotometer should be made below airmasses of 5. If all these recommendations are followed, one may aspire to achieve a reduction of each optical depth error component to well below 0.01 and the goal of 0.01 for the total optical depth error.

1 Introduction

The nocturnal monitoring of semi-transparent atmospheric features, such as particles (aerosols, optically thin clouds) or gases (O_3, H_2O) can be performed using attenuated starlight, to derive a spectral optical depth. The passive remote sensing method of stellar spectrophotometry (known as starphotometry in atmospheric science) was accordingly introduced in the early 1980s (Alekseeva, 1980; Roddier, 1981). Despite some technological progress, accurate stellar spectrophotometry remains a slowly progressing challenge (Deustua et al., 2013; Bohlin et al., 2014). A perception of the successes and problems associated with starphotometry over the years can be obtained by consulting, for example, (Roscoe et al., 1993; Leiterer et al., 1995, 1998; Herber et al., 2002; Pérez-Ramírez et al., 2008a, b; Baibakov et al., 2009, 2015; Ivănescu, 2015). The accuracy of the optical depth (OD) retrieval remains critical for particle feature extraction methods, which require sub 0.01 optical depth error (O'Neill et al., 2001a). Other technical and data processing challenges remain inasmuch as this relatively rare type of instrument, with only a few operational starphotometers worldwide, is still evolving.

Sunphotometry, and to some extend moonphotometry, are much more mature technologies. The current starphotometers cannot yet, for example, parallel the automated robustness of the CIMEL sunphotometers in the AERONET network (see Holben et al. (2001) for a discussion of the CIMEL instrument and the AERONET network). One can aspire to benefit from the accomplishments of the solar methodology and improve its nocturnal counterpart. An early and comprehensive analysis of sunphotometer related errors and its data processing procedures was detailed in Shaw (1976), with

subsequent contributions by (Forgan, 1994; Dubovik et al., 2000; Mitchell and Forgan, 2003; Cachorro et al., 2004).

Optical depth retrieval, typically in the near-UV to near-IR spectral range, is based on the Beer–Bouguer-Lambert law of atmospheric attenuation. The detailed heterochromatic (wide spectral band) attenuation law was investigated by King (1952); Rufener (1963, 1986); Young and Irvine (1967). While employing wide spectral bands enhances the S/N (signal to noise ratio) of faint stars, the attenuation law is substantially simplified in the monochromatic approximation. Depending on the acceptable error, the approximation is generally valid for spectral bandwidths narrower than 50 nm (see Golay (1974), pages 47–50). The narrow bands typical of sunphotometry are also employed in starphotometry: however accuracy requirements generally limit the operational star set to the brightest stars (visual magnitudes less than 3).

Beyond the fact that stellar photometric observations are currently not accurate enough, the lack of information on certain types of errors is even more problematic. Our purpose is to overcome such issues and enhance the starphotometry reliability. A comprehensive initial analysis of stellar photometry errors was detailed in Young (1974). Strategies for retrieving accurate photometric observations in variable optical depth conditions were proposed by Rufener (1964, 1986). Those fundamental astronomical studies remained largely unreferenced in atmospheric science literature. In the present study we invoke and complement them in order to identify and characterize most sources of systematic uncertainty. We expect that, with the proper approach, optical depth accuracy within 0.01 is achievable. That target aside, the very act of approaching this value, is worthwhile as it will increase the level of trust and reliability in starphotometry. We aim to achieve such a goal by identifying ways to mitigate the most important errors, either by instrumental improvement, retrieval algorithm improvement or improved observational strategies.

The paper will consist of instrumental descriptions and retrieval methods followed by a comprehensive discussion of error sources for each key parameter. It will terminate with recommendations for achieving the 0.01 goal. Most of the errors we describe are of a general nature, while some are specific to our particular spectrometer-based starphotometers (Ivănescu et al., 2014). We only focus here on accuracy aspects, leaving precision and calibration errors to be addressed in subsequent studies. We also do not analyse nonlinear aspects characterizing measurements in the water vapor absorption bands, a subject which has already been extensively described in Galkin and Arkharov (1981), Halthore et al. (1997), Galkin et al. (2010a) and Galkin et al. (2010b).

2 Observing conditions

As detailed in Appendix A, our data has been acquired with basically two types of instrument/telescope configurations built by Dr. Schulz & Partner GmbH: the similar SPST05/SPST06 instruments with Intes Micro Alter M703 telescope, and the SPST09 instrument with Celestron C11 telescope (all being spectrometer-based photometers). The calculations of Appendix A identified their FOVs to be $57.3''$ and $36.9''$, respectively. SBIG CCD cameras are employed for star acquisition, where the native camera pixels are binned into larger pixels of 3×3 native pixels, with an angular resolution of $3''$/bin for the SPST06/M703 instruments and $2''$/bin for the SPST09/C11 instruments. Other technical parameters of the most recent version (SPST09/C11) are listed in Table 1.

Table 1. Technical parameters of SPST09

Telescope	Schmidt-Cassegrain C11 Celestron, aperture 280 mm, focal length 2800 mm
Measurement range	399.1 – 1159.3 nm, resolution 0.7 nm
Standard channels	17 channels: 420, 450, 470, 500, 532, 550, 605, 640, 675, 750, 778, 862, 934, 943, 953, 1024, 1040 nm
FOV	$36.9''$
Wavelength error	$\pm$ 2 nm
Diffraction method	grating
Spectral bandwidth	FWHM $\simeq 8.2$ nm
Detector	CCD sensor S7031 (Hamamatsu)
Number of pixels	1024×58 (1044×64 total), 24.6 μm^2
Quantum efficiency	90% peak
ADU	22 e^-/cnt
Standard exposure	6 sec
Time resolution	<3 min for OSM, <6 min TSM
Star mag. range	<3
OD accuracy	0.003- 0.011
Guiding system	two SBIG CCD cameras
Tracking system	mounts: GTO900, AZA2000, G11
Operating temperature range	down to -80°C (with additional temperature insulation and heating)
Interface	RS232
Power supply	12V (3 A)
Instrument weight	13 kg
Telescope weight	14 kg

The simultaneous measurement of all channels by all three spectrometer based systems renders them unique and particularly appropriate for observing rapidly evolving atmospheric features, such as optically thin clouds. This is important for purposes of coherent spectral analysis where all the channels have to capture the same sky view. Other starphotometer types are filter wheel based systems that sequentially observe one channel at a time (see, for example Leiterer et al. (1995); Herber et al. (2002); Pérez-Ramírez et al. (2008b)).

The observation sites included a variety of environments: warm, continental environment at the mid-latitude sites of Egbert and Sherbrooke; warm, continental and marine environment at the mid-latitude site of Halifax; warm and dry, tropical high altitude site influenced by frequent Saharan dust events at Izaña; marine environment at the low Arctic site of

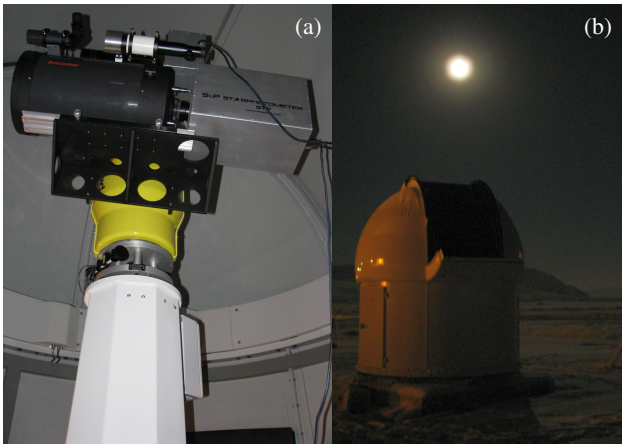

Figure 1. The SPST09 starphotometer and C11 Celestron telescope installed on the AZA-2000 mount, inside the Baader dome in Eureka (a). Outside view of the dome in Eureka, during a starphotometer observation (b).

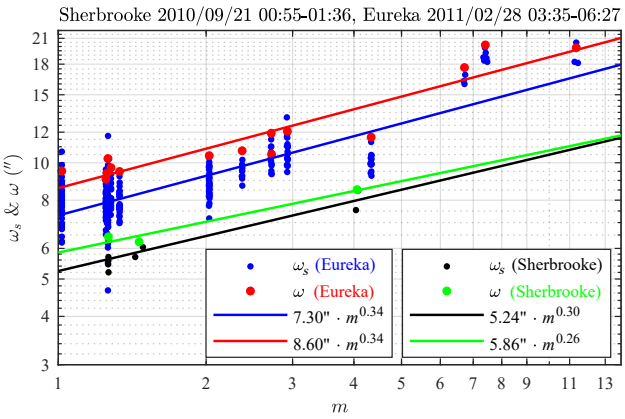

Figure 2. Very large star spots measured at Sherbrooke and Eureka, with weaker than expected dependence on the airmass. The symbol ω_s is associated with short time exposures, while ω represents long time exposures.

Barrow and a cold and dry environment, influenced by the quasi-constant presence of ice crystals at the low altitude, high Arctic site of Eureka. The latter is unique in terms of its extreme environmental conditions and the deployment of a larger telescope (C11). More details about the Eureka instrument and the observing facility (shown in Figure 1), as well as its remote operation are found in Ivănescu et al. (2014). One particular consideration of note in this case is the recurring frost formation on the telescope corrector plate and the quasi-constant deposition of ice crystals on it.

In Figure 2 we present observations of star spot sizes (FWHM $\equiv \omega_s$ for short, quasi-instantaneous exposures and ω for long time exposures), at Eureka and Sherbrooke, as a function of the observing airmass. There are 5–40 short exposures per recording position (the Kendrick Astro heating system, which we normally use, was not present for this experiment). The exposure integration times are star dependant and, in order to avoid detector saturation, are varied in the 1–30 second range. The exposure-to-exposure position change on the CCD of these short-exposure spots (the blue and black dots), is largely influenced by turbulence jitter (Roddier, 1981)). To account for this aspect and fully characterize the turbulence, one artificially creates long-exposure (1–4 minute) spots by adding up the short exposure CCD images. The spot size of the artificial images will inevitably be relatively large and will be an average indicator of turbulence. We should note that starphotometry integration times correspond to the short exposure times: the reason that we create the artificial images is to adequately characterize the low frequency component of the turbulence.

In order to avoid any flux loss, the photometer FOV must be much larger than the FWHM of the short exposure image, whose intensity profile (the star Point Spread Function, or PSF) can be approximated with a Gaussian profile (Racine, 1996). The total FWHM is then quadratically composed of the FWHM$= \omega$ of the "seeing" spot (the blurring due only to the air turbulence) and the FWHM$= \omega_d$ of the Airy spot (the blurring due to the diffraction through the telescope aperture). The latter is also approximated by a Gaussian profile with the same FWHM as the diffraction spot. Optical aberrations, especially coma for this type of telescope, may also play a role. However, tests done at AiryLab (2012) show that the C11, when correctly collimated, is not subject to optical aberrations that influence the size of such large star spots as those of Figure 2. The angular size of an Airy spot can be computed as $\omega_d = 1.03 \cdot \lambda / D$, with λ the measurement wavelength. This gives less than $1''$ ($0.49''$ for C11 and $0.75''$ for M703), at $\lambda = 640$ μm (peak of CCD detection). Since these values are 10-20 times smaller than the star spots, the observed FWHM is practically ω. Figure 2 indicates that, for typical atmospheric remote sensing sites (near sea-level, not particularly dry, near heated buildings etc.), the expected seeing could be ~ 10 times larger than what is usual in professional astronomy ($\sim 1''$). Uncontrolled telescope motion in strong winds may also increase the size of the recorded star spots. However, for the observational conditions associated with Figure 2, the impact of surface winds was largely negligible.

The turbulence strength can be assessed through the length parameter r_0 (Fried, 1966). If we apply the ω values of Figure 2 to the expression of Racine (1996) ($\omega = 0.976 \cdot \lambda / r_0$) we obtain r_0 in the 5–15 mm range (about the size of the inner scale of turbulence). This means that the turbulence goes beyond the inertial Kolmogorov spectrum, into the dissipation regime of the von Karman spectrum (Osborn (2010), pages 16–17). This may explain the values of 0.3–0.34 for the exponent of m in Figure 2, corresponding to a 3D turbulence power spectrum with an exponent of about 15/3, that is characteristic for the von Karman spectrum at high spa-

tial frequencies (see, for example, Figure 2.3 ibid). One normally expects an exponent of 0.6 (or 3/5) for an inertial Kolmogorov turbulence (Roddier, 1981). Also, since ω of Figure 2 corresponds to an averaged $\lambda = 630$ nm, and since $\omega \sim \lambda^{-1/5}$, then ω should be $\sim 10\%$ larger at 400 nm, and $\sim 10\%$ smaller at 1000 nm.

With respect to the $\omega \simeq 1''$ values usually experienced at high altitude professional (non-amateur) astronomical sites, it's important to note the dramatically large values associated with the sea-level (10 m altitude) Eureka station of Figure 2. However, the seeing at the 610 m altitude Ridge Lab (CANDAC site, also at Eureka) is, relatively very small (Steinbring et al., 2013) and comparable with the best observing sites. One concludes that most of the turbulence at Eureka is confined in the first few hundred meters above sea level. It is instructive to characterize the vertical structure of the turbulence, notably its effect on the refractive index variation and, consequently, on star blurring (see, for example, Owens (1967) for basics on the refractive index of air). Unfortunately, a precise characterization solely based on radiosonde measurements may not be possible (Roddier, 1981). However, the usual approach, when a reliable theory is not yet developed or there is not enough information, is to approximately parameterize the vertical structure. We accordingly express the vertical variation of the star spot size due to turbulence as

$$d\omega = k_c \cdot k_t \cdot d\mathrm{n} \cdot dv/v \tag{1}$$

where dv/v is the relative wind shear (whose kinetic turbulent energy is the primary influence on the refractive index variation (dn) between the atmospheric layers). This equation is a first order, empirically convenient expression whose goal was to arrive at a coarse representation of ω versus altitude. The constant $k_t \simeq 6$ is an empirical normalizing constant that adjusts the right side of equation (1) so that its integration yields the surface ω values of Figure 2. Employing an ensemble of Eureka, polar winter profiles acquired over a ~ 6 weeks period about the measurement time of Figure 2, we integrated the $d\omega$ interpretation of those profiles from the maximum altitude of the radiosonde to a given altitude in order to yield ω at every altitude (Figure 3). On the median (red) and average (green) curves one can identify major blurring increases: just below 3 km, below 200–400 m (suggesting a quasi-permanent turbulent layer), and again about 10–20 m from the surface. This confirms the very low ω values at the Ridge Lab, despite the dramatically large seeing at sea-level.

3 Observing methodology

A photometric system, from the perspective of the astronomical community, is a system assessing the brightness of an object on a logarithmic scale, normalised to a standard reference (a natural source or a convenient synthetic spectrum).

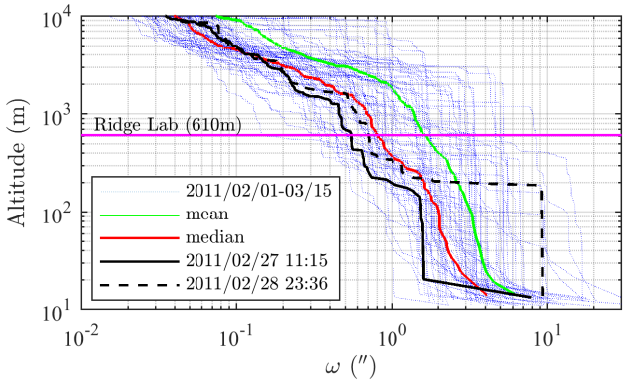

Figure 3. Vertical structure of star spot blurring in Eureka derived from the quadrature integration of equation (1). Most of the turbulence is below the Ridge Lab elevation (magenta line). The black curves comes from the two most nearly synchronous radiosondes to the ω measurements in Figure 2. The $k_t = 6$ (derived for the black curves) was employed for all the other curves.

3.1 Catalog photometric system

We denote by I the star irradiance expressed in absolute measurement units. By definition, the apparent magnitude (M) of a star is the ratio between I and the unattenuated irradiance ($I_{0,c}$) of a reference source

$$M = -2.5 \log \frac{I}{I_{0,c}} = -2.5 \log I + 2.5 \log I_{0,c} \tag{2}$$

where log is short for $\log_{10}$. The quantity

$$\mathrm{ZP} = 2.5 \log I_{0,c} \tag{3}$$

is usually referred to as the "zero-point" of the photometric system and it practically identify it. The star magnitudes are therefore photometric-system dependent. One should note that the magnitude of the reference source is, by definition, $M_{0,c} = 0$ at any wavelength (i.e. when $I = I_{0,c}$). Since Vega has been historically considered a magnitude zero star, one may naturally use $I_{0,c}$ as the irradiance of Vega. Most of the current photometric systems are actually based on Vega as primary reference ("primary standard") (Bessell, 2005).

One can rewrite equation (2) with a zero subscript to denote the case where the starlight is measured outside of the Earth's atmosphere

$$M_0 = -2.5 \log \frac{I_0}{I_{0,c}} = -2.5 \log I_0 + 2.5 \log I_{0,c} \tag{4}$$

The expression "outside of the Earth's atmosphere" can take on various adjectival forms in the literature. These include unattenuated, extraterrestrial, extra-atmospheric, exoatmospheric or zero-airmass. Ground measurements are usually referred to as ground-based or attenuated. The extraterrestrial magnitudes, being intrinsic characteristics of the stars,

can be predetermined and are found in the catalogs of various observation campaigns. M_0 obtained with the V standard wide-band filter (Johnson and Morgan, 1953), covering most of the visible spectrum, is usually called visual V magnitude. The blue B magnitude is obtained then with their B band filter, etc.

In terms of the spectral range of starphotometry, the most accurate reference source available is the Pulkovo catalog (Alekseeva et al., 1996). It provides exoatmospheric irradiances for most of the brightest stars ($V < 3$), in the near-UV to near-IR spectral range. One should note however that, while those irradiances are correctly expressed in SI units of W/m^2/m in the VisieR online database (Ochsenbein et al., 2000), their values in the published paper have to be divided by 10^5 to yield W/m^2/m. Their corresponding magnitudes (Alekseeva et al., 1994) are simply expressed as

$$M_0 = -2.5 \log I_0 \tag{5}$$

with I_0 being the exoatmospheric star irradiance converted to cgs units of erg/s/cm^2/cm. From equation (3) and (4), one deduces that ZP = 0 in equation (5). Therefore, the reference spectrum used to compute the Pulkovo catalog magnitudes is $I_{0,c} = 1$ erg/s/cm^2/cm, at any wavelength. This is usually called a "raw" photometric system (or "raw" magnitudes). Since 1 W/m^2/m = 10 erg/s/cm^2/cm, then $I_{0,c} =$ 0.1 W/m^2/m: this reference is commensurate in magnitude with the Vega spectrum maximum of 0.0796 W/m^2/m at 402.5 nm (when measured at 8.2 nm bandwidth).

3.2 Theoretical considerations

The starphotometer measurement principle is based on the Beer–Bouguer-Lambert attenuation law applied to the starlight passing through the Earth's atmosphere (as described, for example, in Liou (2002)). The attenuation, due to the out-scattering and absorption of the incoming light by atmospheric particles and gases, is described by

$$I = I_0 e^{-m\tau} \tag{6}$$

with τ being the total vertical optical depth, m the stellar airmass, I and I_0 the attenuated and unattenuated star irradiances, respectively. For the plane-parallel atmosphere approximation, $m = 1/\cos\theta$, with θ being the zenith angle of a given star.

This law is more practically expressed in terms of apparent magnitudes (M and M_0), as defined in equations (2) and (4). Taking the logarithm of equation (6), one obtains

$$\log \frac{I}{I_0} = -\frac{M - M_0}{2.5} = -m\tau \log e \tag{7}$$

where e is the natural logarithm base. The exponential law then becomes a linear relation in terms of apparent magnitudes

$$M = M_0 + 2.5 \log e \cdot m\tau = M_0 + (m/0.921)\tau \tag{8}$$

This expression, in conditions of approximately constant τ, can be used to retrieve the intercept M_0 from a linear regression of M versus m. This can be done, for example, by employing a series of irradiance measurements carried out over a clear night with significant changes in m (not always a given in the case of a high Arctic site). Such a procedure is referred to as the Langley calibration technique, or Langley plot (also described in Liou (2002)).

3.3 Practical considerations

The measured signal (F) of the star flux is expressed in counts per second (cnt/s). If $F_{0,s}$ is an unattenuated reference signal defining the instrument photometric system, the attenuated and unattenuated instrumental magnitudes (S and S_0) can be expressed, in a manner analogous to equations (2) and (4)

$$S = -2.5 \log \frac{F}{F_{0,s}}, \qquad S_0 = -2.5 \log \frac{F_0}{F_{0,s}} \tag{9}$$

where the subscript "s" is employed as the instrumental reference (of a separate instrumental photometric system) in order to minimize confusion relative to the catalog reference "c". One can convert F into I, its corresponding irradiance in absolute units, with an instrument specific conversion factor

$$c = \frac{I}{F} \tag{10}$$

Applied to the two system references, the ratio becomes

$$c_r = \frac{I_{0,c}}{F_{0,s}} \tag{11}$$

This represents a transformation (scaling) factor from the instrument to catalog reference system. Therefore, in addition to accounting for the optical and electronic throughput of the instrument, the unitless c/c_r ratio also incorporates the photometric system scaling. In terms of magnitudes, this defines the instrument-specific calibration parameter

$$C = -2.5 \log \frac{c}{c_r} = -2.5 \log \frac{I}{I_{0,c}} - \left(-2.5 \log \frac{F}{F_{0,s}} \right) \tag{12}$$

Substituting S and S_0 from equations (9), as well as M and M_0 from equations (2) and (4) into equation (12), yields

$$C = M - S \tag{13}$$

$$C = M_0 - S_0 \tag{14}$$

where the role of C as a conversion factor between the catalog and instrument magnitudes is made readily apparent by the elegant simplicity of this pair of equations.

If one observes $I_{0,c}$ (i.e. the catalog reference source, for which $M_{0,c} = 0$, as per equation (4)), then $C = -S_{0,c}$ from equation (14). Accordingly, if the catalog reference is an actual star, C can be obtained by measuring the unattenuated

instrumental magnitude of that star. Alternatively, when observing the instrumental reference $F_{0,s}$ (i.e. the reference source for which $S_{0,s} = 0$ as per equation (9)), equation (14) indicates that $C = M_{0,s}$ (i.e. the catalog magnitude of the instrument reference source). Equating the C values for those two special cases yields $M_{0,s} = -S_{0,c}$.

In practice, equations (9) are often expressed as

$$S = -2.5 \log F = -\ln F / 0.921 \tag{15}$$

$$S_0 = -2.5 \log F_0 = -\ln F_0 / 0.921 \tag{16}$$

This either implies that F and F_0 are unitless (i.e. measurements are already normalised to the instrument reference), or that the reference is conveniently chosen as $F_{0,s} = 1$ cnt/s, so ZP = 0. This is the "raw" photometric system that is employed for our starphotometers. Consequently, the calibration parameter may be expressed as

$$C = -S_{0,c} = 2.5 \log F_{0,c} = \ln F_{0,c} / 0.921 \tag{17}$$

with $F_{0,c}$ the instrument signal measured when observing the star catalog reference ($I_{0,c}$). Having spectrally constant, unit values for both photometric system references, implies that the scaling factor is also unit ($c_r = 1$). This yields

$$C = -2.5 \log c = -2.5 \log \frac{I}{F} \tag{18}$$

The calibration reduces then to the measurement of any source of known irradiance. Equation (18) may be used in laboratory based calibrations, or in "in-situ" calibrations, by measuring any accurately known star spectra. This may be done in a Rayleigh atmosphere (i.e. without aerosol or clouds), for which the attenuation can be accurately estimated (Bucholtz, 1995). Such conditions can generally be approximated at high elevation, calibration sites (supported by some independent estimate of the small but non negligible aerosol optical depth).

If we define, for simplicity

$$x = m / 0.921 \tag{19}$$

equation (8) can be rewritten as

$$M = \tau x + M_0 \tag{20}$$

Substituting M from (13) into (20), yields a Langley calibration equation whose ground-based (τ dependent) component is expressed in terms of the instrument signal S

$$M_0 - S = -\tau x + C \tag{21}$$

This expression enables the retrieval of C when M_0 is provided by a catalog. However, if an accurate M_0 spectrum cannot be found, then equation (14) can be used to transform equation (21) into a pure instrumentation version

$$S = \tau x + S_0 \tag{22}$$

so that a catalog is no longer required. Instead of finding C, one has to employ Langley calibrations to estimate S_0 for all stars that are part of the operational protocol of a given starphotometer. Equation (21), on the other hand, has the advantage of casting the calibration procedure in terms of an explicit function of a single star-independent constant (C). C represents an intrinsic parameter that remains constant as long the instrument characteristics do not change.

3.4 Measuring methods

3.4.1 One-star method (OSM)

Inasmuch as the main purpose of starphotometer measurements is to retrieve the optical depth (τ), we rearrange equations (21) and (22) accordingly

$$\tau = \frac{S - S_0}{x} = \frac{S - M_0 + C}{x} \tag{23}$$

Restricting measurements to one star speeds up the acquisition process. This is particularly useful in the presence of rapid τ variations that one observes, for example, during cloud events. However, since equation (23) contains calibration values, any optical or electronic degradation of the instrument will propagate into the τ estimation.

3.4.2 Two-star method (TSM)

The Langley calibration enabled by equation (21) allows the direct retrieval of τ as the slope of a linear regression between S and x. In lieu of having calibrated the starphotometer to exploit the OSM or in lieu of carrying out a Langley plot using one star over a large range of x (typically over hours of measurements), one may simply use two different stars for generating observations at two different airmasses, and employ the "Δ method" introduced by Leiterer et al. (1998). From equation (21), we can derive

$$\tau = \frac{(S_1 - S_2) - (M_{01} - M_{02})}{x_1 - x_2} \tag{24}$$

where the subscripts "1" and "2" refer to a low star (large airmass) and a high star (small airmass), respectively. In order to minimize OD errors associated with this technique, the airmass difference between the two stars should be large. However, beyond airmass 5, the impact of higher measurement errors may overcome the benefits of a large airmass range (see Young (1974) for an optimization analysis). In practice, the high star is in the range of 1–2 airmasses, while the low star is in the range of 3–5.

The “auto-calibrating” feature of equation (24) (i.e. no need for C), is limited in its applicability: there are temporal and spatial restrictions on the variation of τ between the two observations. It is therefore a method that is more appropriate for the typically weak and slow variations associated with aerosols (as opposed to the typically strong and

high frequency variations associated with clouds). There are also restrictions on the optical throughput variation: specifically in terms of any dust, dew, frost or snow deposition on the telescope optics or star vignetting and focusing variations between the two observations. In fact, the TSM can be interpreted as an OSM, with C being determined by regression through only two data points. The TSM-based calibration vector can be obtained from equation (23)

$$C = \frac{(S_1 - M_{01})x_2 - (S_2 - M_{02})x_1}{x_1 - x_2} \tag{25}$$

3.5 Optical depth accuracy

In reality, we cannot measure the starlight alone, since the measurement always includes a background signal B. The latter is mainly due to electronics readout signal and sky brightness. If R is the starphotometer measurement obtained while pointing towards the star, then B can be estimated by a slightly off-axis measurement. In dark sky conditions, B is dominated by the instrument dark current. The desired starphotometer (starlight) signal is estimated as

$$F = R - B \tag{26}$$

with attendant systematic error components

$$\delta_F = \delta_R + \delta_B \tag{27}$$

For small relative errors δ_F/F, one obtains δ_S by taking the derivative $|S'|$ of S with respect to F in equation (15)

$$\delta_S = |S'|\delta_F = 1.0857\frac{\delta_F}{F} \tag{28}$$

If the only errors are in S, then equation (23) yields

$$\delta_\tau = \frac{\delta_S}{x} = \frac{1}{m}\frac{\delta_F}{F} \tag{29}$$

However, the optical depth accuracy is subject not only to errors in the observational parameter (S), but also to all the other physical parameters (M_0, C, x) involved in the starphotometry retrieval. By differentiating equation (23), one identifies all the contributions to the observation error along the line of sight

$$\delta_\epsilon \equiv x\delta_\tau = -\delta_{M_0} - \delta_x\tau + \delta_S + \delta_C \tag{30}$$

The other components of the observation error that represent magnitudes (M_0 and C, as per equations (5) and (18)) can, in a similar fashion to equation (28), be expressed as

$$\delta_{M_0} = 1.0857\frac{\delta_{I_0}}{I_0}, \qquad \delta_C = 1.0857\frac{\delta_c}{c} \tag{31}$$

A comprehensive description of starphotometry related errors can be found in Young (1974) and Carlund et al. (2003). In the following sections we continue this work by quantifying the accuracy of each individual parameter of equation (30) (M_0, x, S & C).

4 Spectrophotometric catalog (M_0) accuracy

In order to move from a star-dependent S_0 calibration, which is currently the standard (Rufener, 1986; Pérez-Ramírez et al., 2011), to the more convenient star-independent calibration in terms of C, one has to make sure that the exoatmospheric magnitudes M_0 are sufficiently accurate. The star dataset that we employed (Appendix B) was limited to stars having magnitude stability within 0.005, as determined by the observations leading to the Pulkovo catalog (Alekseeva et al., 1996) and are employed as the default catalog by the manufacturer of our instruments. They are mostly main-sequence stars (of luminosity class V) (Kippenhahn et al., 2012) at the most stable period of their life-cycle (five are of luminosity class II–III). Five are of "early-type" spectral class B stars (i.e. B0–B3), one of "late-type" class A (i.e. A7–A9) and one of class F. They are all characterized by weaker absorption lines and cleaner continuum (Silva and Cornell, 1992). However, the "early-type" B stars may also experience non-negligible (0.01 magnitudes) photometric variability (Eyer and Grenon, 1997). This remains to be confirmed using ongoing, state-of-the-art Gaia satellite investigations (Brown et al., 2018). Beyond their intrinsic photometric stability, the M_0 accuracy remains a concern. Alekseeva et al. (1996) stated that: "to preserve the uniform absolute system for all our seasonal catalogues, we always used the same energy distribution of Vega based on the absolute calibrations by Oke and Schild (1970) and Kharitonov et al. (1978)". As if the Pulkovo catalog was not old enough relative to the current technological capabilities, its data was calibrated to the accuracy level achievable about 50 years ago. In addition, Knyazeva and Kharitonov (1990) specified that their (Kharitonov et al. (1978)) calibration values were actually erroneous. In spite of the shorcomings of the Pulkovo catalog, it remains the most accurate catalog to encompass our entire bright star dataset of Appendix B. By comparison, the Hubble Space Telescope (HST) measured only a few of those stars. To better understand the impact of the Pulkovo catalog shortcomings, we compared its absolute irradiances with those measured by the HST. This higher accuracy dataset only contains a few bright stars: Vega (HR7001) and Sirius (HR2491) from the CALSPEC Calibration database (Bohlin et al., 2014), and HR15, HR2618 and HR4295 from the STIS New Generation Stellar Library (NGSL) (Bohlin et al., 2001). Inasmuch as HST measurements are performed with a more recent technology, are not subject to atmospheric effects and have absolute errors below 1% (Bohlin, 2014), we considered them to be the reference. The corresponding magnitude differences between the Pulkovo and HST spectra, computed in terms of the Pulkovo photometric system, are presented in Figure 4. Within a context of the potential impact of atmospheric errors, it is remarkable for a catalog derived from ground-based measurements, that more than half of the standard starphotometer channels (open circles) are characterized by errors of less than 2% or equivalently

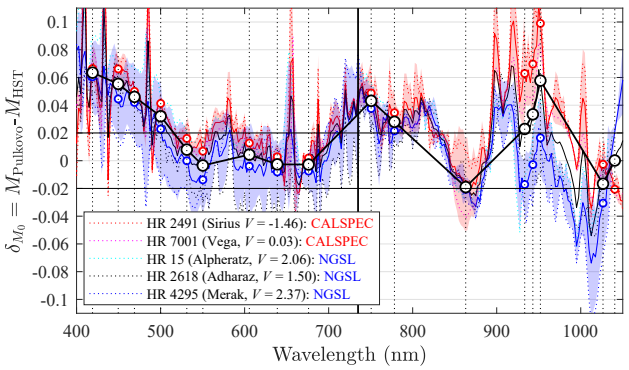

Figure 4. Spectrophotometric bias (δM_0) of the Pulkovo catalog with respect to two different HST catalogs (CALSPEC and NGSL). Open circles represent our standard starphotometer channels, solid colored lines are δM_0 averages for each HST catalog, while the colored shading represents the corresponding standard deviations. For each spectrum point, the two colored curves and their shading represent sampling populations of 2 points (stars) for the red CALSPEC catalog and 3 points (stars) for the blue NGSL catalog: our objective here was to obtain an estimate of δM_0 statistics assuming δM_0 values were roughly independent of the M_0 values of individual stars.

$\delta M_0 < 0.02$ (equation (31)). Based on the average difference of Figure 4, one nevertheless concludes that the Pulkovo catalog is characterized by a bias that is particularly large in the near-UV and in the 900-1000 nm range. These biases may, in part, be attributable to uncertainties related to the stronger aerosol scattering effects in the UV and to water vapour effects in the near-infrared (NIR). The average bias found in Figure 4 could then be used to correct the Pulkovo catalog. However, a bias will not actually affect the optical depth measurements. For example, in the TSM mode, such a bias is canceled out in the M_0 magnitude difference of equation (24). Even in the OSM mode of equation (23), the bias will actually pass into C during the calibration process. This bias transfer is attributable to the fact that a bias will only affect the intercept of the Langley plot, not its slope, as expressed by equation (21). The δM_0 standard deviation of Figure 4 (~ 0.02), can, on its own merits, be compared with the accuracy of 0.015–0.02 claimed for the Pulkovo catalog (Alekseeva et al., 1996), although these values increase in the UV and water vapour channels. One should also note that for its primary reference stars, such as Vega and Sirius, the 0.02 Pulkovo catalog upper limit of error is halved. Such error levels will impact information extraction from optical depth spectra, especially as the required accuracy for aerosol retrievals sensitive to higher orders of the AOD spectrum is ~ 0.01 (O'Neill et al., 2001b).

Figure 5 shows the quasi-constant 8.2 nm bandwidth measured by observing Vega with the SPST09/C11 system. Those FWHM estimates are line broadening measures of the strong hydrogen Balmer series ($H_\alpha = 656.3$ nm, $H_\beta =$

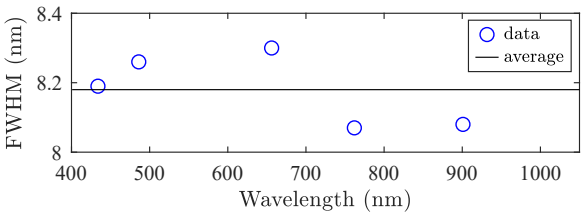

Figure 5. SPST09/C11 bandwidth measured with Vega.

486.1 nm, $H_\gamma = 434.1$ nm, but not $H_\delta = 410.2$ nm). These are absorption lines in the star's own atmosphere and are accordingly intrinsic to the exoatmospheric stellar spectra. We also employed the telluric (i.e. Earth's atmosphere) O_2 line at 762 nm and another near-infrared line specific to Vega. The observations used for the Pulkovo catalog were, in contrast, made at 5 nm bandwidth over the 310–735 nm range and at 10 nm over the 735–1105 nm range (at 2.5 nm nominal resolution). For bandwidth consistency over the entire 310–1105 nm range, Alekseeva et al. (1996) re-processed the 5 nm measurements to synthesize a unique 10 nm bandwidth. Currently, we only use the 10 nm bandwidth version over the entire 310–1105 nm range. However, as noted in Young (1992), a bandwidth mismatch between the catalog and the instrument (i.e. 10 and 8.2 nm, respectively in our case), may have an impact on the optical depth error and merits investigation. In order to asses the impact of the bandwidth mismatch, we compared the magnitude errors when using $M_{5.0}$ and M_{10}, associated with the 5 nm and 10 nm bandwidths, instead of the actual magnitude $M_{8.2}$ at 8.2 nm bandwidth. We also assessed how a simple magnitude calculation $(M_{5.0}+2M_{10})/3$ compares with the actual 8.2 nm bandwidth, in order to improve the actual 10 nm bandwidth catalog. We synthesised star magnitudes for the three different bandwidths by applying Gaussian bandpass filters to the HST data (originally at 1 Å resolution). This is, in fact, a convolution operation that effectively blurs the stellar absorption lines.

In Figure 6 we compare the magnitudes computed for the three bandwidths, for a star of spectral class A0 (Vega). Figure 6a shows a zoom in the neighbourhood of the 420 nm starphotometer channel. The increased broadening with increasing FWHM about the H_γ and H_δ Balmer lines demonstrates the blurring effect of the different bandwidths. The graph also shows that one may actually limit the blurring impact by optimising the spectral location of a given channel. Moving the 420 nm channel to 423 nm will, for example, significantly reduce that impact. Figure 6b shows the contamination due to different blurring levels for the entire spectrum (contamination expressed in terms of δM_0, which from equation (30) is, in the absence of other errors, equivalent to $x\delta_\tau$. The spikey high frequency nature of the δM_0 spectra demonstrates that, while most of the starphotometer channels have negligible (< 0.01) errors, channels in the blue and the near-IR are significantly affected. The black curve

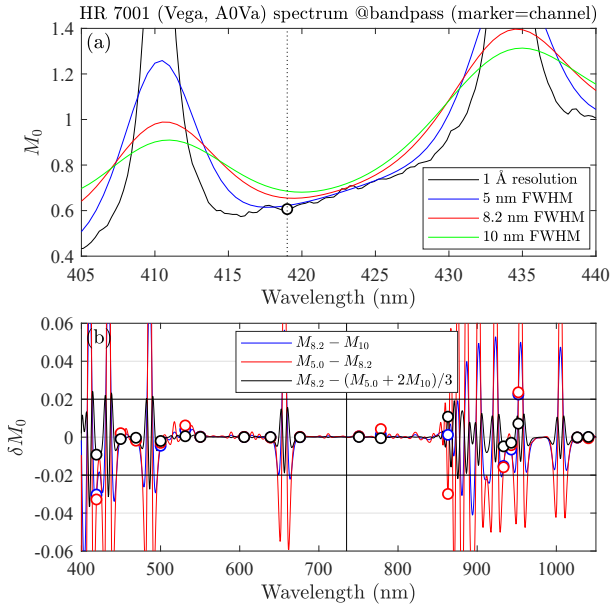

Figure 6. Bandwidth mismatch error for a star of spectral class A (Vega, HR7001). Open circles are the nominal starphotometer channels.

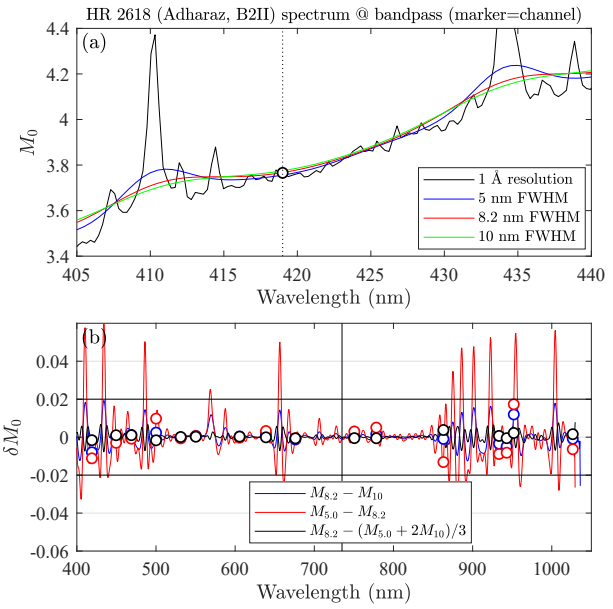

Figure 7. Bandwidth mismatch error for a star of (early-type) spectral class B (Adharaz, HR2618). Open circles are nominal starphotometer channels.

"$\delta M_0 = M_{8.2} - (M_{5.0} + 2M_{10})/3$" demonstrates that one may approximate a spectral convolution using a simple average of twice the upper and once the lower bound magnitudes.

The same exercise carried out for a star of early-type spectral class B (Adharaz) underscores the fact that the H Balmer lines are much weaker (Figure 7a). One expects a similar behaviour for our "late-type" A and F class stars. Consequently, the blurring contamination over the entire spectrum (Figure 7b) is, for the case that concerns us the most ($M_{8.2} - M_{10}$) largely less than 0.01, except for the 958 nm channel that is too close to the 954.6 nm H Paschen absorption line. Inasmuch as all our operational stars are of class A and B (except for one F class star), this analysis is representative. Since the bandwidth mismatch error is a bias that differs for the two star classes of Figures 6 and 7, it may be minimised by distinct photometric calibrations for each star class. However, this may be of limited applicability since the local sky does not present a sufficient array of photometrically stable stars of early-type B, late-type A and F spectral classes.

Up until this point, we have presumed a stable spectral calibration of the instrument. In Figure 8 we show a spectral drift of SPST09 over four months, for four stellar atmosphere absorption lines (hydrogen Balmer series) and two Earth atmosphere absorption lines (O_2 and H_2O). The result indicates a likely spectral drift as large as 1 nm (particularly in the NIR), over the duration of one observation season. Such a non-linear spectral drift is particularly harmful inasmuch as it will likely influence the spectral shape of the photometric calibration vector. A second consequence is that the channels may be subject to additional stellar absorption line contamination if the drift moves them closer to those lines.

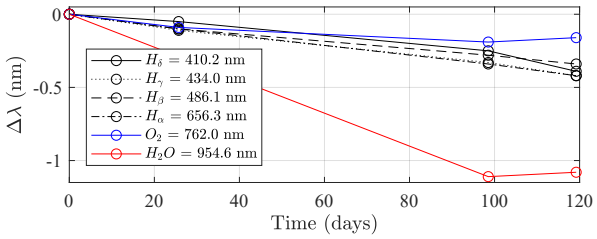

Figure 8. SPST09 spectral drift over the 2017/11/11–2018/03/10 period, for the stellar hydrogen absorption lines of the Balmer series and for the atmospheric O_2 and H_2O lines.

A third broadband consequence of the spectral drift results from the stellar-magnitude spectra being generally characterized by a significant positive spectral slope, over the 400-1100 nm range, for both, A and B class stars, (c.f. Figure 9a and Figure 10a, respectively). This shift in wavelength transforms into a spectral incoherency between the catalogued M_0 values and the measured signal. The M_0 bias, corresponding to the positive-slope stellar spectrum of Figure 9a for ± 1 and ± 2 nm shifts is illustrated in Figure 9b. These results indicate that the maintenance of photometric bias values below 0.01 magnitudes requires a spectral calibration within 1 nm (excluding the case of strong water vapour absorption in the near-infrared). The same exercise is presented in Figure 10 for the early-type B star. While there are individual channel

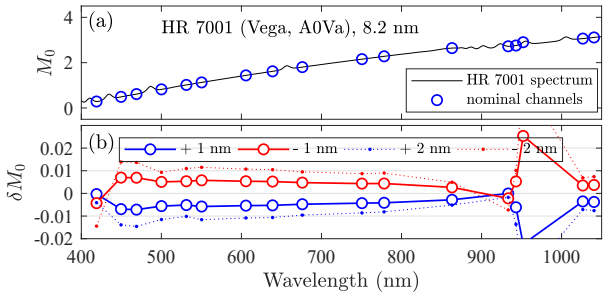

Figure 9. Bandwidth mismatch error for an A class star (Vega, HR 7001), as a consequence of a spectrum shift.

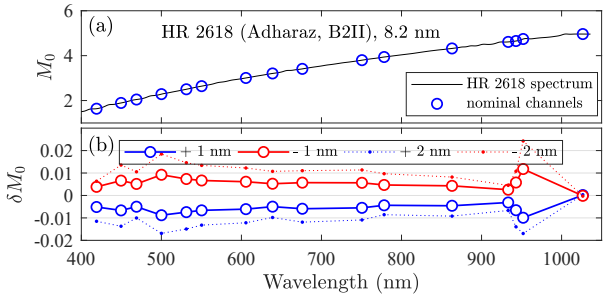

Figure 10. Bandwidth mismatch error for an (early-type) B class star (Adharaz, HR 2618), as a consequence of a spectrum shift.

differences with respect to the class A star, the broad δM_0 results are similar because the M_0 slopes are similar.

As long we employ the same class for both high and low TSM stars, any spectral drift is mitigated in real-time (i.e. similar δM_0 trends produce common biases and thus the type of bias mitigation discussed in the case of Figure 4 will prevail). While the bias in the OSM case will be initially absorbed into the calibration constant, any additional drift will progressively propagate into post-calibration δ_τ error. Based on the analysis of Figure 8 it appears that the spectral drift may be constrained to values $\lesssim 1$ nm if a spectral calibration is carried out at least once per year (and preferably at the beginning of the observing season). Our experience indicates that the six absorption lines employed in the development of Figure 8 are sufficient to adequately characterize the spectral shift of all the starphotometer channels. The radial velocity of our Eureka stars, as retrieved from (Wenger et al., 2000), lead to 0.15 nm maximum Doppler spectrum shift at 1000 nm, and 0.06 nm at 400 nm, among our stars. Therefore, this effect can be neglected during spectral calibration.

An M_0 catalog whose bandwidths match those of the instrument is preferred in order to avoid bandwidth mismatch errors. One natural approach would be to generate a S_0 catalog by calibrating the starphotometer at a high altitude site. A single calibrating site may not, however, yield a sufficient number and class diversity of S_0 values (i.e. a sufficiently comprehensive catalog of stars) to satisfy the starphotometry requirements of a given operational starphotometer site.

For spectrometer based starphotometers, it is necessary to retrieve S_0 at all available spectrometer channels (not just the nominal operational channels) since the spectral drift calculations need to be done at the highest resolutions. This S_0 catalog can then be transformed into a corresponding M_0 catalog by first resampling HST M_0 values of a selected reference (Vega or Sirius) to the spectrometer resolution and then employing equation (14) to compute C. With that HST-derived value of C in hand, the same equation can be rearranged to yield $M_0 = C + S_0$ values for all the other stars. Accurate C values and spectral calibration may also be obtained in the laboratory with the help of a halogen calibration lamp (Paraskeva et al., 2013), or by doing simultaneous measurements on site with a collocated calibrated instrument.

The alternative to an instrument specific catalog is to use a general purpose high resolution spectrophotometric catalog, from which one can synthesize magnitudes at any bandwidth (as we did with the HST spectra). Given the maximum bandwidth mismatch errors found in the Pulkovo catalog (~ 0.04 in Figure 6b for standard channels, at 8.2 nm bandwidth), we estimate that a catalog with about 1 nm bandwidth, i.e. about a factor 10 less, would be enough to limit the errors to < 0.01. We note that the generally sub 0.01 mismatch errors estimated for a 1 nm spectrum shift (Figures 9b and 10b) are not inconsistent with this affirmation. In general a higher resolution catalog such as the HST catalog, with its 1 Å, resolution would be preferred. It is however surprising that there are no existing high resolution, near-UV to near-IR, spectrophotometric catalogs that achieve 1% accuracy (Kent et al., 2009) for the bright ($V < 3$) stars. The stars observed by professional astronomers are usually much fainter ($V > 6$) in order to avoid saturating the detectors. This may explain the lack of interest from the astronomical community in improving the absolute spectrophotometry of bright stars. An effort to address this situation was pursued by Le Borgne et al. (2003), with their release of the STELIB catalog. However, we identified large biases in the blue/UV part of the STELIB spectra (Figure 11) in comparison with the HST NGST catalog. The fact that the Pulkovo catalog also has the largest bias in that range (Figure 4), suggests a recurring issue for catalogs generated from ground-based observations (perhaps due to the higher optical depth in the blue, and the deficient compensation for aerosol contributions), and accordingly, that an accurate catalog must be of extraterrestrial origin. It is however noteworthy that Zhao et al. (2012) reported a new ground-retrieved catalog (including our entire bright stars dataset) derived from the measurements of the Large Sky Area Multi-Object Fiber Spectroscopic Telescope (LAMOST). The spectral resolution and bandwidth of this catalog are variable, but always sub-nm. The spectral range extends over most of our spectrum, but unfortunately not beyond 900 nm.

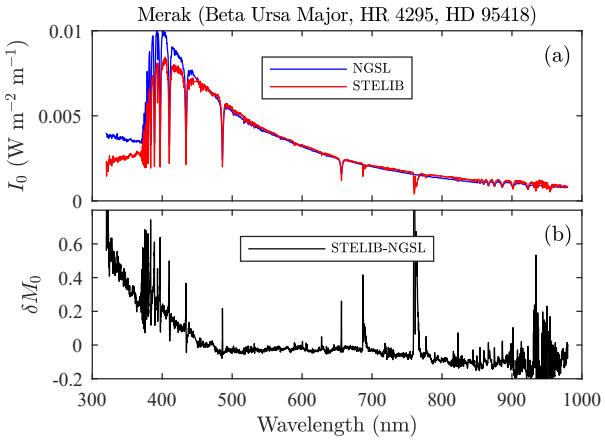

Figure 11. Spectrophotometric comparison of STELIB catalog with respect to the HST-NGSL (a). Important bias shows up in the UV and a much weaker one in the IR (b).

As an alternative to satellite-based catalogs, the recent ACCESS rocket project (Kaiser and Access Team, 2016) was also a promising initiative, given their mandate to perform high spectral resolution photometry near the top of the atmosphere. Unfortunately their list of $V < 3$ bright stars is limited to Sirius and Vega. Another recent initiative is the NIRS STARS campaign (Zimmer et al., 2016), whose mandate is to produce a bright star spectrophotometric catalog using lidar measurements to back out the atmospheric contribution. However, once again, the brightest stars ($V < 3$) are largely excluded from consideration. Probably the most promising option is to use the star observations of the GOMOS satellite (Kyrölä et al., 2004). This sensor employs high resolution (1.2 and 0.2 nm, depending on spectral bands) limb starphotometry to retrieve ozone and other atmospheric components from space. Its off limb measurements, performed before each limb scan, can be used to build an exoatmospheric spectrophotometric catalog (Ivanescu et al. (2017)). GOMOS doesn't cover our entire 400–1100 nm spectrum: it's unfortunately limited to the spectral ranges of 250–675 nm, 756–773 nm and 926–952 nm. It covers the problematic spectral ranges in the case of ground-based observations: UV/blue range, O_2 and H_2O absorption bands. The missing portions of the starphotometer spectra can be filled in by fitting the STELIB, LAMOST spectra, synthetic spectra (Rauch et al., 2013) or averaged star-type spectra (Pickles, 1998) to the GOMOS measurements.

We will continue, in the short term, to employ the Pulkovo catalog spectra for the operational M_0 values of our star dataset (Appendix B). However we will employ the 8.2 nm version, over the available spectral range, to mach our starphotometer bandwidth.

5 Airmass (x) accuracy

Systematic errors in the calculation of the airmass m (or alternatively x) can be significant (see, for example, Rapp-Arrarás and Domingo-Santos (2011) for a review of analytical airmass formulae). The following operational equation characterizes m, in a spherically homogeneous, dry-air atmosphere with an accuracy of better than 1% at $m = 10$ (Hardie, 1962):

$$m = \sec z - 0.0018167(\sec z - 1) - 0.002875(\sec z - 1)^2 - 0.0008083(\sec z - 1)^3 \quad (32)$$

where z is the apparent zenith angle (the zenith angle of the refraction-dependent telescope line of sight). This expression only departs significantly from the plane parallel expression of $m = \sec z$ at values of $m > 5$. If the target star position is computed using astronomical data rather than a measured instrumental mount position then it is more appropriate to use the true zenith angle (z_t) formula of Young (1994). The computation of z_t can be effected using star coordinates, site location and time. It ensures an associated maximum 0.0037 airmass error at the horizon (with respect to calculations made on a standard mid-latitude atmospheric model).

One should note that the airmass depends slightly on the vertical structure of the atmosphere (Stone, 1996; Nijegorodov and Luhanga, 1996): an effect which is particularly distinctive in a polar environment. The relative errors due to such environmental variations are however below 0.2% up to $z \simeq 82°$ ($m \simeq 7$), and below 1% at $z \simeq 87°$ ($m \simeq 15$) (Tomasi and Petkov, 2014). Differences in airmass associated with different atmospheric constituents (Tomasi et al. (1998) and Gueymard (2001)), have negligible impact on the observation accuracy of starphotometry.

In spite of the generally high accuracy associated with airmass expressions, the airmass error can be significant if the recorded time stamps are inaccurate. Stars targeted by our starphotometers are recentered between several (3–5) consecutive exposures: a process that is of variable duration (usually 20–40 s). The airmass associated with the mean of all the measurement times (the one reported) may differ from the airmass associated with the mean observing time (the weighted mean time where the weights are exposure duration times). A δ_x error in x, induced by a δ_t time error, is equivalent to a measurement error $\delta_\epsilon \equiv \delta_x \tau$ (equation (30)). Figure 12 shows the variation of δ_ϵ with altitude (for hypothetical observation sites at different elevations), for a $\delta_t = +30$ s case (i.e. time overestimation leading to $\delta_x > 0$ for a descending star), at $\lambda = 400$ nm, and for three different airmasses in a Rayleigh atmosphere (the condition of molecular scattering domination; see Bucholtz (1995) for the optical parameterization of a Rayleigh atmosphere).

The variation of δ_ϵ with x is shown in Figure 13a for observations at 10 m (Eureka elevation) and 2360 m (Izaña observatory elevation). The real x variation at Eureka is weak

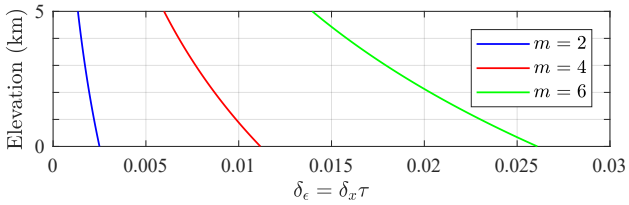

Figure 12. Assessment of stellar magnitude errors associated with airmass miscalculation errors due to a time delay error (δ_t) of 30 s in a Rayleigh scattering atmosphere and as a function of the hypothetical elevation of a starphotometer site.

(near the poles, stars carve out sky tracks that vary little in zenith angle). The δ_ϵ variation, for unrestricted variation in x (up to $x = 7$), will be comparable for both sites. Figure 13b shows the corresponding δ_τ error for Izaña (solid blue line) growing linearly with x, and a dominating x^2 dependency demonstrated by the saturation of the $\delta_\epsilon(x)/x^2$ curve (dashed blue line). For this simulated δ_t = 30 s case, $\delta_\tau < 0.01$ even at large x. However, the computer time may typically drift about 1 min per year (Marouani and Dagenais, 2008): a scenario where δ_τ would be significant. The computer time thus has to be corrected weekly, if not daily (using, for example, a GPS time server).

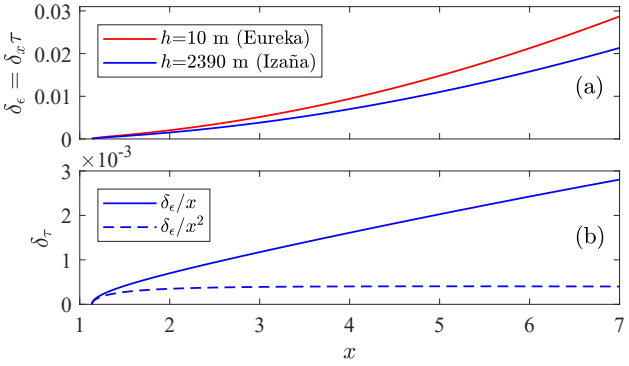

Figure 13. (a) Assessment of accuracy associated with airmass miscalculation errors for a descending star (same conditions as Figure 12). (b) δ_τ in the case of Izaña site (where $\delta_\tau = \tau\delta_x/x = \delta_\epsilon/x$), while δ_ϵ/x^2 shows δ_x dependency in x^2.

6 Observation (S) accuracy

6.1 Heterochromaticity

Wide-band optical depth calculations using starlight as the extinction source were first described in Rufener (1964) (in French). A comprehensive description by Golay (1974) (pages 47–50) affirms that non-linear, wide-band radiation detection effects are negligible in terms of S estimation for spectral bandwidths narrower than 50 nm. The error associated with this non-linear component is about the squared ratio between the bandwidth and the central wavelength (i.e. $(\Delta\lambda/\lambda)^2$), Rufener (1986)). A bandwidth of less than 40 nm is then sufficiently small to achieve optical depth errors < 0.01 at 400 nm. These optical depth (heterochromaticity) errors should be well below the negligible value of 0.001 for our sub 10 nm starphotometer-channel bandwidths.

6.2 Lognormal fluctuations

The optical depth retrieval, as expressed by equation (23) or (24), is based on computing the instrumental magnitudes S through the logarithm of the measured star signal F. However, before doing so, one performs an arithmetic mean $\overline{F}$ over several consecutive exposures. Since F is subject to lognormal fluctuations induced primarily by scintillation effects (Roddier, 1981), one should characterize its probability distribution in terms of its geometric mean $\overline{\log F}$ and its geometric standard deviation $\sigma_{\log F}$. The corresponding bias, called "misuse of least-squares" by Young (1974), is given by

$$\delta_{\log F} = \log \overline{F} - \overline{\log F} = \sigma^2_{\log F}/2 \tag{33}$$

(a classical relationship between the geometric and arithmetic means). From equation (15) and the general definition of a standard deviation, $\delta_S = 2.5\delta_{\log F}$ and, similarly, $\sigma_S = 2.5\sigma_{\log F}$. The bias then becomes

$$\delta_S = \sigma^2_S/5 \tag{34}$$

Since a single OD measurement is effectively the arithmetic mean of 3–5 measurements, then only observation fluctuations with $\sigma_S > 0.22$, which we basically never experienced (even at large airmasses), would lead to $\delta_S > 0.01$. One can conclude from equation (29) that $x\delta_\tau < 0.01$ and thus that this issue is negligible in starphotometry.

6.3 Forward scattering

Forward scattering into the photometer FOV by atmospheric particulates increases the magnitude of S and thereby induces an underestimate of the optical depth. This "forward scattering error" can be estimated with the single scattering expression

$$\frac{\delta_\tau}{\tau} = \overline{\omega} \cdot P\Delta\Omega \tag{35}$$

where $P\Delta\Omega$ is the integral of the normalised scattering phase function P over the angle $\Omega =$ FOV$/2$ (Shiobara et al., 1994). Figure 14 shows a variety of forward scattering error calculations obtained using equation (35) at a wavelength of 400 nm. The red curve represents a typical biomass burning aerosol example (Qie et al., 2017), based on P given by the widely used Henyey–Greenstein (HG) phase function (Zhao et al., 2018). It underscores its negligible forward scattering error on any practical FOV size.

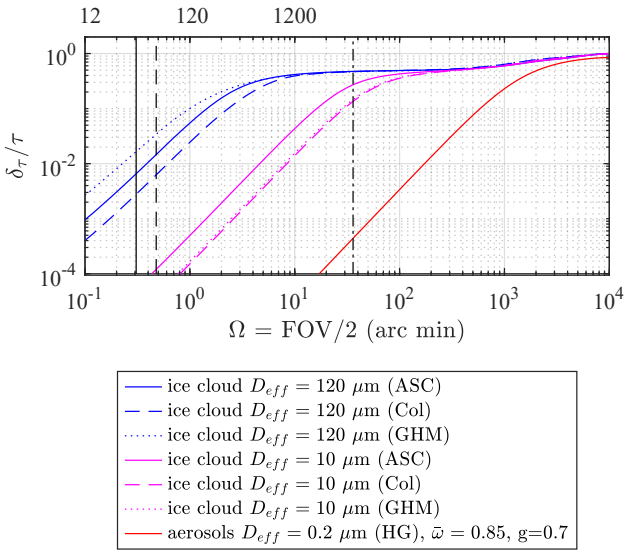

Figure 14. The relative forward scattering error for typical aerosols and ice-clouds, as a function of the half field of view. The vertical black lines correspond to SPST09/C11 (solid line), SPST05/M703 (dashed line) and Cimel sun/moon photometers (dash-dotted line). The acronyms between accolades specify the phase function model.

For ice-crystals, $\overline{\omega}$ is practically unity. Two ice-crystal effective diameters were employed: 10 μm (non-precipitating clouds, magenta curves) and 120 μm (precipitating clouds, blue curves). Three crystal habit models were employed to represent the variation of the bulk phase function with crystal habit (from the computations of Baum et al. (2014)): severely roughened aggregates of solid columns (ASC, solid curves, typical in the high Arctic), severely roughened solid columns (Col, dashed curves) and general habit mixture (GHM, dotted curves). Several relevant instruments are represented by vertical black lines in Figure 14: SPST09/C11 (solid), SPST05/M703 (dashed) and the Cimel Sun/Moon photometers with a 1.2° FOV (dashed-dot).

The computations of Figure 14 assume that the contaminating particles (those that induce the FOV scattering effect) are also the particles that one seeks to detect. Those δ_τ/τ computations still apply when the contaminating particles differ from the particles to be detected as long as the FOV effect of the contaminating particles dominates the FOV effect of the latter (for example the FOV effect could be dominated by small OD ice clouds while one seeks to detect fine mode aerosols of significantly larger OD). Aerosol or cloud detection using CIMEL-like instruments in the contaminating presence of any type of thin ice cloud is a critical consideration, with $\delta_\tau/\tau \sim$ 0.2–0.5, and δ_τ being $\gtrsim 0.01$ if the cloud optical depth $\gtrsim 0.03$. In the case of our star photometers, those errors are negligible in the presence of non precipitating ice clouds. In the case of precipitating clouds, the SPST09/C11 instrument, for which $\delta_\tau/\tau \sim 0.01$ still provides the required accuracy for $\tau < 1$.

6.4 Night sky background

Airglow, and potentially aurora, can be important contributors to the night sky background (see Chattopadhyay and Midya (2006) on the importance of airglow). Their high frequency temporal and spatial variability (Dempsey et al., 2005; Nyassor et al., 2018) complicates their elimination in a background subtraction process. This can lead to significant optical depth systematic errors. Their spectra are similar: in particular both exhibit a strong 557.7 nm [OI] green emission line, whose intensity is used for classification of auroral strength. Unique signature features of each phenomenon are those due to OH band emissions in the case of airglow and N_2 (first positive system) emissions in the case of aurora (Chamberlain, 1995). The emission line intensities are usually expressed in Rayleigh (R) units (effectively a measure of directional panchromatic radiance, as per Baker (1974)), with the airglow exhibiting typical 557.7 nm (line-integrated) values of ~ 0.25 kR. The International Brightness Coefficient (IBC) is employed to discriminate four aurora classes: IBC1 = 1 kR (brightness of the Milky Way); IBC2 = 10 kR (brightness of thin moonlit cirrus clouds); IBC3 = 100 kR (brightness of moonlit cumulus clouds); and IBC4 = 1000 kR (provides a total illumination on the ground equivalent to full moonlight) (Chamberlain, 1995). We note that the assessment of the accuracy errors for those classes, may help to infer the effect of moonlight and moonlit clouds too.

Figure 15a shows their emission density spectra (Rayleigh per unit wavelength), converted to 8.2 nm bandwidth of our starphotometers. The airglow data (the black solid curve) represent tropical nighttime observations made by Hanuschik (2003). These include zodiacal light (sunlight scattered by dust from the solar system ecliptic plane). The actual airglow emissions should accordingly be even weaker. The aurora density spectra (the colored solid curves) are a compilation of observations from Jones and Gattinger (1972), Gattinger and Jones (1974), Jones and Gattinger (1975) and Jones and Gattinger (1976). Their spectra were adjusted to produce three curves, representing the first three IBC levels. Their common continuum (without respect to aurora class) is adjusted to 8 R/Å, the minimum value proposed by Gattinger and Jones (1974).

Figure 15b enables an appreciation of airglow and aurora effects on starphotometer measurements. It shows the ratio of those spectra to the Vega spectrum (artificially attenuated to magnitude $V = 3$, the faint limit of our star dataset). The resulting estimates of optical depth error (equation (29) converted to observational error $x\delta_\tau$ of equation (30)), in the presence of uncorrected emission contributions, correspond to the throughput of the C11. Optical depth errors for the M703 (shown only for the IBC2 case of red dots) are the result of the M703 (FOV-filling IBC2) flux being 2.4 times

larger than that of the C11 (i.e. the ratio of their solid angles, $(57.3/36.9)^2$). We note that, in spite of the fact that the C11 emission spectra are significantly higher in the near IR spectral region, they are, except for the IBC3 case, generally less than 1%. Short term airglow variability induced by air density fluctuations engendered by gravity waves may occur (Nyassor et al., 2018). Figure 15b indicates however that typical airglow conditions have negligible error contribution. Even at twilight, when the Sodium emission lines, at 589.3 nm, can be enhanced by a factor of 5 (i.e. the "Sodium flash" reported by Krassovsky et al. (1962), the potential accuracy error remains negligible.

On the other hand, the aurora is characterized by a much higher temporal and spatial variability (Dempsey et al., 2005). Beyond that, the aurora shown in Figure 15 is of the green type (i.e. main visible line at 557.7 nm), but one may have other types too, the most common being red, with the main visible line at 630 nm. Therefore, one may get spectral variation too. Such variations may induce significant departures from the nominal emission background spectra of Figure 15a. Considering the results of Figure 15b the worst estimation of those variations, the optical depth error remains well below 0.01 for the C11 telescope, even when observing a weak $V = 3$ star during an IBC2 aurora (solid red line). An IBC3 Aurora can, given that a (factor of 10) IBC class change is equivalent to a magnitude change of 2.5, be accomodated by employing a sufficiently bright star: the IBC3 representation for a $V = 0.5$ star will decrease to the red (sub 0.01 error) IBC2 curve in Figure 15b. Fortunately, given the current location of Eureka in the auroral oval (Vestine, 1944), IBC3 aurora will only be seen occasionally near the horizon. Therefore, the accuracy errors of Figure 15b will only appear at airmasses above 5. However, this may change in the next decades, given the recent fast pace migration of the magnetic pole (Witze, 2019).

The IBC definition provides a way to also infer δ_F/F errors associated with the presence of thin moonlit clouds by simply arguing that the red IBC2 curve of Figure 15b also applies to the IBC2 analogy of “thin moonlit cirrus clouds”. By definition, the δ_F spectrum for such a case corresponds to the IBC2 radiance of Figure 15a. The F value for a $V = 0$ star in a thin-cloud atmosphere can be modelled, in an order of magnitude fashion, by assigning a value of $\tau x = 3$ to equation (21). Using this attenuated star signal as a rough model for the IBC2 moonlit clouds analogy, we employ the same equation to show that the $V = 0$, cloud-attenuated star magnitude is equivalent to an unattenuated ($\tau = 0$) $V = 3$ star. In other words, the same F is used to obtain the red δ_F/F curve of Figure 15b but, with the added rider that the exoatmospheric star was a $V = 0$ star. Accordingly the acceptability of the sub 10^{-2} red error curve in Figure 15b applies to the moonlit cloud IBC2 analogy, but for a $V = 0$ star. Actually, given the strong snow albedo in the Arctic, thin cloud brightness may even exceed IBC2 brightness during full moon conditions. Quantitative assessment of optical depth errors related to moonlit and twilight lit sky brightness, especially in cloudy situations, would however require the development of a radiative transfer model informed by starphotometer background measurements. Given the complexity and specificity of such endeavour, this will be addressed in a future study.

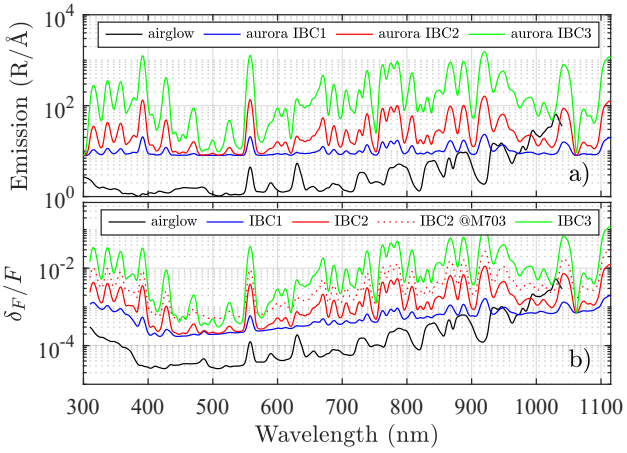

Figure 15. Typical emission density spectrum for airglow and aurora (a). Corresponding optical depth error in the presence of uncorrected emission contributions (b): $\delta_\tau = \delta_F/F$ (from equation (29) for $m = 1$), representing the ratio of emission to a Vega spectrum dimmed to $V = 3$ and attenuated in a Rayleigh atmosphere. When observing a $V = 0.5$ star, the corresponding aurora IBC types can be one class brighter to achieve the same optical depth errors. The red-colored dots show comparative $V = 3$ results for the (larger FOV) M703 instrument (see text for details).

The typical polar wintertime night sky background spectrum at Eureka (in terms of catalog-photometric-system magnitude per square arc-second) is shown in the Figure 16a, at two different times: mid-day (magenta curve, local time) and evening (blue). The evening sky is darker and approaches the

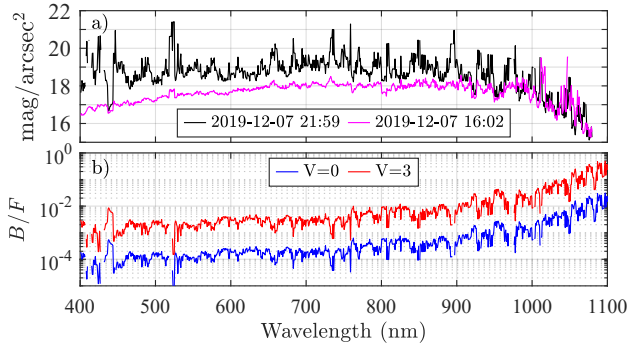

Figure 16. a) Night sky background spectrum, measured with the Eureka SPST09/C11 (in the Pulkovo catalogue photometric system), at mid-day (magenta curve) and evening (black curve) during the polar night. b) Ratio of background to star flux, for the evening sky and for two star magnitudes: Vega at $V = 0$ (blue curve) and a dimmed Vega at $V = 3$ (red curve). Times are UTC.

detection limit of our instrument (as made evident by its noisier profile). This detection limit may be the reason for the difficulty in identifying the aforementioned aurora and airglow lines in the visible range. An omnipresent weak line, unassociated with any major aurora emission lines, is however noticeable around 440 nm (436–445 nm band). Some absorption lines can also be identified: 532 nm, probably due to O_4 (Orphal and Chance, 2003) and 663 nm, probably due to NO_3 (Orphal et al., 2003). The midnight sky is expected to be even darker (higher visible magnitude). One also notices a brighter infrared spectrum, rather constant throughout the day, confirming the J band measurements of Sivanandam et al. (2012). This may be associated with the airglow OH lines, but a factor ~ 10 higher than estimated in Figure 15b. The evening sky background with respect to a magnitude $V = 3$ star (simulated by dimming Vega) exceeds the 1% mark beyond 900 nm (red curve in Figure 16b). With respect to a magnitude $V = 0$ star (Vega, blue curve), the evening sky background remains below the 1% mark in the starphotometer spectral range, i.e. < 1050 nm. This indicates that accurate measurements, in the case of weakly radiating ($V > 1$) stars, can only be achieved by applying a reasonably accurate background subtraction for wavelengths > 1000 nm.

7 Calibration parameter (C) accuracy

The accuracy of the calibration parameter C retrieval is dependent on the performance of the calibration procedure and will accordingly be addressed in a separate study. C accounts for the optical and electronic throughput: we asses here the instrument instability or degradation that may alter it.

7.1 Misalignment issues

One way to get throughput degradation is by losing flux outside the boundary of the FOV, due to focusing error (blurring), to off-axis star centering errors, or because the FOV is simply too small (design error). The instrument was originally built for the M703 telescope specifications. The smaller FOV of the C11 telescope (almost half of M703's) is at greater risk of focusing errors, particularly in Eureka, where the star spots are larger (Figure 2). An analysis of the impact of design shortcomings on both instruments is an instructive exercise. Figure 17 illustrates the effect of defocusing the optical train within the context of the associated OD errors (case of the C11 telescope) and of star centering errors (cases of both, C11 and M703 telescopes). The fitted curves, which are well modelled by an $a|s|^b$ equation, are only employed to estimate the error variation for low OD (where the density of measurement points is prohibitively small). For the focusing error, the negative and positive s values mean the star spot shift, in steps of the focusing stage (the adjustable unit that controls the focusing of the star photometer, at ~ 1.36 mm/step along the axis, or equivalently $\sim 10''$/step angular increase of the confusion circle), before and after passing through the on-focus position. For the centering error, they mean the spot shift, in pixels of the high resolution camera, before and after passing through the on-axis position.

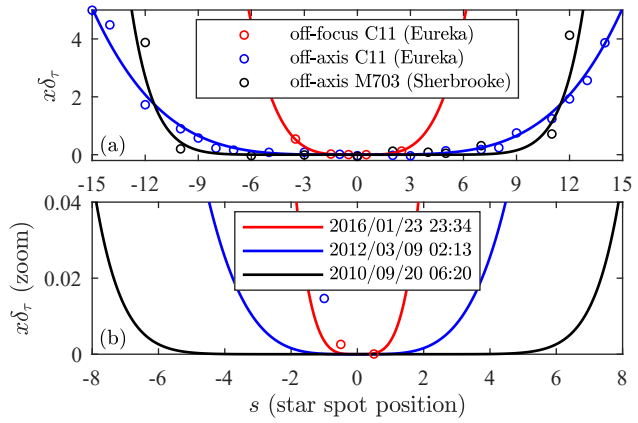

Figure 17. Optical depth increase induced by throughput degradation due to misalignment: star focusing error (red for C11) and centering error (blue for C11 and black for M703). For focusing, the positions s represent focusing stage steps (at $\sim 10''$/step increase of the confusion circle); for centering they represent high resolution camera binned pixels, at $3''$/bin for M703 and $2''$/bin for C11. (a) data and $a|s|^b$ fit; (b) the same fit as (a), but zoomed-in to low OD (the measurement date and UTC time is indicated in the legend).

Our focusing stage employs a continuously driven motor, subject to electronically controlled steps. Those steps represent approximately the same distance along the optical axis, based on a fixed driving time interval. The best that can be achieved is a half-step focus, for which the flux loss, in the C11 case, is a negligible ~0.02%. In the absence of an automatic focusing procedure, the focus has to be checked and adjusted manually whenever there is an important temperature variation. This may happen because of weather changes or as the result of opening the dome (with significant optical impacts up to one hour after the opening). Based on our Arctic experience, the focus must be corrected by one focus step for each 10°C change of temperature: if this correction is performed, the flux loss is a negligible 0.35%. Any focusing errors larger than that will significantly affect the optical depth estimation (Figure 17b).

Star centering is based on an automatic tracking procedure that ends once a chosen centering tolerance δ_c is satisfied. Such a tolerance has to be small enough to ensure that, during the subsequent measurement, the star still remains in the accepted centering range, despite any drift due to its natural jitter (spot wandering due to the air turbulence). On the other hand, a faster centering procedure can be achieved using a larger tolerance. There is therefore a trade-off to be made between those two requirements. This is investigated in Appendix C, by taking the constraints posed by the FOV into account. We show, for a perfectly aligned star, that the maxi-

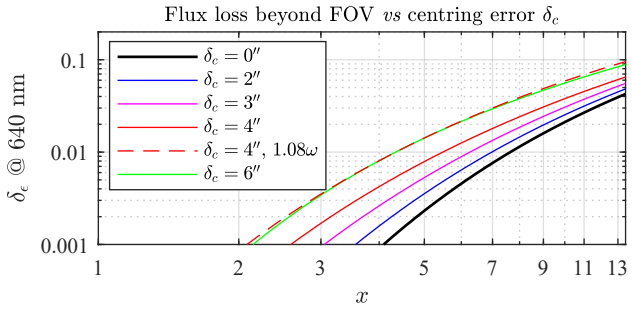

Figure 18. Observation error due to throughput degradation in Eureka when using the SPST09/C11 system. This error is the result of a FOV that is too small combined with a centering error (see the main text for details).

mum seeing that the FOV can accommodate is 16.7″, for our C11 Arctic telescope. This is borderline at $m = 5$ in Figure 2 (long exposure case). Obviously, this somewhat excessively small FOV is a design shortcoming that can be fixed, for example, with a larger limiting diaphragm.

In order to asses the accuracy, we employ the calculations of Appendix C to transform the Arctic star spot sizes of Figure 2 into the corresponding observation errors of Figure 18. The black curve represents a systematic throughput degradation due only to the flux loss at the edges of the star spot. Such degradation characterizes the case of a perfectly centered ($\delta_c = 0''$) short exposure star spot (ω_s).

The colored curves account for the attendant error due to different centering tolerance choices ($\delta_c = 2''$, $4''$ & $6''$). We compute them by quasi-quadratically summing (with a 5/3 Kolmogorov turbulence exponent) the natural jitter contribution and the position uncertainty inside the tolerance zone (i.e. $(\sigma_\theta^{5/3} + \delta_c^2)^{1/2}$, with σ_θ from Appendix C). One has to keep in mind, however, that those calculations are based on the blue linear fit of data points used in Figure 2.

The possible variations about that line can be estimated inasmuch as the short exposures indicate a standard deviation of 5-10%. This is about the 5% difference between the long and short exposure spot sizes in the Kolmogorov turbulence case, as computed in Appendix C (the approximation $\omega_s \simeq 0.95 \cdot \omega$ following equation (C2)). However, for the purposes of our error modelling, we retained an empirical 8% standard deviation case. The ω_s values (of a Gaussian distribution in ω_s) may accordingly be greater than ω values 33% of the time (33% of the Gaussian distribution that extends across the red line at one standard deviation from its blue-line mean). This 1.08ω case is represented by the dashed red-colored $\delta_c = 4''$ curve of Figure 18. The difference with respect to the plain red curve accounts then for the seeing variation. Since it already exceeds our accuracy limit of 0.01 at $x = 4.4$ (or $m \simeq 5$), it represents the maximum acceptable δ_c for the constraints of our SPST09/C11 system.

7.2 Non-linearity

Non-linearity of detector response to incoming light flux is another source of systematic error. The onset of significant non-linearity conditions occurs at ∼8000 cnt/s (i.e. $V = -0.47$ with the C11 telescope, a level normally not reached by any star other than Sirius). If the sky brightness due to atmospheric scattering of sunlight is strong (at dawn or dusk at mid-latitudes, or for longer periods during seasonal shifts of the late and early winter in the Arctic), this limit will be exceeded. The culmination of the non-linearity is that, using our standard 6 s integration, the detector progressively approaches its saturation point at 2^{16} counts, or $65535/6 = 10922.5$ cnt/s (i.e. $V = -0.8$ for C11). The consequence, as illustrated in Figure 19, is an apparent decrease of star brightness (artificial reduction of the difference between the star and the sky measurements) with a corresponding increase in the computer value of the optical depth. The onset of non-linearity in the case of Vega (whose signal is ~ 5000 cnt/s at transit in Eureka) begins at a background (B) value of ~ 3000 cnt/s (at a total signal of ~ 8000 cnt/s as indicated above). One should never employ an instrument such as the C11 to make Sirius ($V = -1.46$) attenuation measurements unless the OD > 0.5. Data whose signal exceeds 8000 cnt/s should be discarded unless a subtraction process that accounts for the onset of non-linearity is applied.

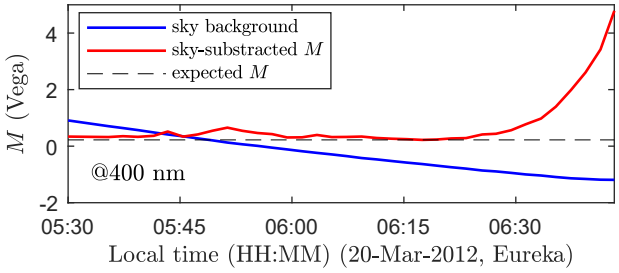

Figure 19. Apparent decrease of star brightness (increase of magnitude M) as the sky background brings the detector into a non-linear regime. The star brightness has been corrected for sky brightness (the latter has been subtracted out from the former). The separate background measurement (blue line) is not affected by the non-linearity of the detector since $B < 8000$ cnt/s, but the sum $F + B$ used to compute S is, leading to $M = S + C$, equation (13).

The sky background is strongly influenced by O_3 absorption. This is likely due to the multiple scattering influence of the effective increase in the light path length (from the sub-horizon Sun to the telescope line of sight). This is underscored in Figure 20 where we compare, in a relative fashion, the starphotometer sky background measurements with sky irradiance (daylight) computations at the bottom of a standard atmosphere for a solar zenith angle of 48.12° "standard indirect solar reference spectrum" (ASTM-G173-03, 2012). The presumed multiple scattering impact of ozone is almost negligible in the latter case, when compared with the starpho-

tometer measurements for the sub-horizon Sun case. One should also note that other absorption bands, like O_2 at ~ 760 nm or H_2O at ~ 940 nm (for example), remain comparable. This means that the non-linearity, as well as saturation, happens first in the blue, leading to a distortion of the retrieved aerosols optical depth spectrum.

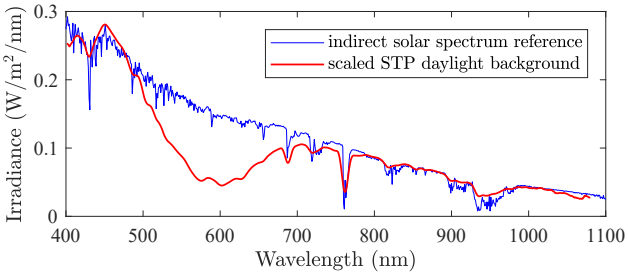

Figure 20. Daylight sky background: standard ASTM G173-03 indirect solar reference sky irradiance spectrum (blue); scaled starphotometer background measurements in Eureka (2018-02-18 10:33, local time) to match ASTM infrared level (red).

7.3 Delayed background

Unlike the majority of instrumentally related calibration-degradation influences discussed in this section, the particular problem of delays in background measurements (and the background contamination problem discussed in the next subsection) are of a combined instrumental and observational nature. It concerns bright background conditions, mainly twilight, when the only feasible observation mode is OSM. If the background subtraction is effected using a background measurement which is delayed in time (~ 30 s) relative to the star measurement (as is the case for our instruments), then S will sustain a systematic error, that becomes progressively worse as the sky brightness increases. Figure 21 illustrates the sky background increase for seven standard channels, as acquired at Eureka in support of a morning series of OSM measurements. When those channels (notably the longer wavelength channels of Figure 21) approach the saturation point, near 09:00, the relative rate of increase $\delta B/B \simeq 0.01$ over the 30 s delay (as computed from the local slope of the curves just before the onset of significant saturation). This leads to an observation error $x\delta_\tau \simeq \delta B/F \simeq 0.01 \cdot B/F$. Accordingly, the sky brightness should never exceed the star's brightness if the OD error is to be less than 0.01. The minimum OD error due to 30 s delay in such anomalously bright (dawn or dusk) conditions is $0.01 \cdot 5000/3000 = 0.017$ for Vega (for other stars is larger, since their F is smaller).

One can nevertheless mitigate this error by extrapolation from outside the saturation regime and correct for it in post-processing. This procedure is, however, less than ideal inasmuch as the duration spent on a given star measurement is not known precisely due to the unknown duration of the star recentering process between exposures. In any case, one generally expects the residual δ_B to be 10-20% of the initial. This yields OD errors < 0.01 for the entire linear range, even when observing $V = 3$ stars.

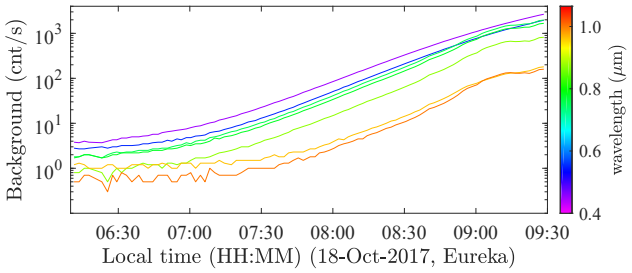

Figure 21. Sky brightness increase in the morning, in Eureka, for seven standard channels. The blue part of the spectrum is brightest.

7.4 Background contamination

This can also be considered as both, an observation issue and an instrumental issue, i.e. affecting the calibration parameter. This kind of error is a design shortcoming affecting our older SPST05 and 06 instrument versions (both employing the Losmandy mount). The error has been corrected since it was first noted, but its existence is worth mentioning because the source of this problem was not obvious. As indicated above, background subtraction has to be performed subsequent to the star measurement. Based on the appendix C calculations and on the Eureka star spot sizes shown in Figure 2, the position of the background measurement should be made at a star separation larger than $35''$ with the C11 telescope and $45''$ with the M703 (i.e. $1.1 \cdot \omega$ at $m = 5$, plus half of the FOV) to make sure the FOV encases less than 1% of the star flux on its border. A separation of $60'' = 1'$ would be then a safe enough margin. A separation of $8'$ was, in actual fact, a feature of the original design (i.e. similar to the FOV of the high resolution camera). However, a shortcoming in the implementation of that design meant that, for some areas in the sky, the telescope mount fails to achieve the requested move. This can result in erroneous S values induced by the star spot signal contaminating the background measurement. In Figure 22 we show one particularly extreme event that occurred during the Halifax campaign (see Section A2 for details of the campaign). Fortunately, we could correct this type of error in post-processing by interpolating between the neighbouring low level, spike-free points on either side of the spikes seen in Figure 22.

7.5 Internal temperature variation

The dark current of our detector (S7031-1006 Hamamatsu CCD) varies exponentially with temperature according to the manufacturer's specs. Our instruments incorporate two-stage temperature stabilisation controllers, in order to increase the ambient temperature operation range and accordingly, mini-

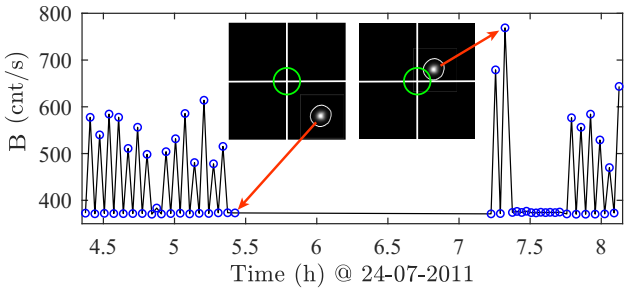

Figure 22. Star spot contamination of the background measurements (spikes) observed during the Halifax campaign with SPST05/M703. The spikes occur when background measurements are acquired too close to the star. The 1% star flux level (white circles around the star spots) should never foul the photometer FOV (green circles).

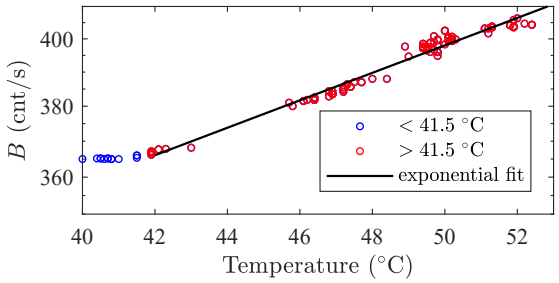

Figure 23. Variation of B due to dark current increase with the instrument enclosure temperature above the 41.5°C (1040 nm channel). These measurements were acquired with the SPST05/M703 instrument during the Halifax campaign. The stabilised dark current is 365 cnt/s.

mize any temperature sensitive OD retrieval errors. The first stage stabilizes the instrument enclosure to 30 ± 0.5°C. The instrument's cold-environment design features include internal heaters to help reach and maintain the temperature set point. It does not however, incorporate coolers to compensate for warmer temperatures. The influence of warmer temperatures may, as a consequence of the heat generated by the enclosed (quasi-hermetical) electronics, occur when the outside temperature surpasses 0°C. The only way to cool in such a circumstance is to remove any thermal insulation plates. At higher outside temperatures one simply opens the instrument box for ventilation in open air. The second stage controller is a thermo-electric cooler (TEC), that stabilizes the detector temperature to a standard set point of -10°C, (adjustable in the -20°C to -8°C range). The TEC can cool down 30° to 45°C below its environment (the instrument enclosure). However, from our measurements, this range is rather found to be 38.5° to 51.5°C.

In warm environments, one can maintain the control up to an enclosure temperature of 41.5°C (Figure 23). Above that, the dark current (the main component of B in dark

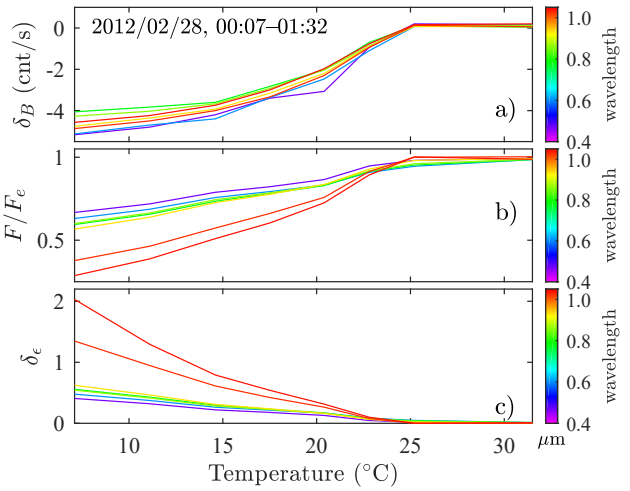

Figure 24. B variation (δ_B) due to dark current decrease when the instrument enclosure temperature starts below the control range (a), measured in Eureka with SPST09/C11. Detector sensitivity as a function of temperature (b) and the corresponding observation error $\delta_\epsilon = x\delta_\tau \simeq |F - F_e|/F$ (c). The measurements were acquired at Eureka with the SPST09/C11.

sky conditions) increases exponentially with the temperature (slightly more pronounced in the near-infrared). In Figure 23 the exponential fit looks linear because of the short vertical range. In cold environments, the instrument enclosure can be subject to temperatures below the lower limit (28.5°C) of its nominal control range. This may happen, for example, during the instrument warm-up phase (Figure 24), or when the outside temperature drops below -45°C and the internal instrument heaters struggle to maintain the $+30$°C set point. The resulting dark current variation (δ_B) is illustrated in Figure 24a). Because it decreases exponentially with the temperature, its variation is much weaker than that induced by temperatures above the upper limit of the control range. This nonetheless results in significant variation of the detection sensitivity (F/F_e), as shown in Figure 24b (where F_e is the star signal once the temperature reaches the nominal control range). This sensitivity ratio is approximately linear with temperature. The much larger slope in the near-infrared channels converts into particularly large observation errors (Figure 24c).

7.6 Throughput degradation

Even in the type of clean environment typically found at a mountain top astronomical site, one can notice an optical throughput degradation due to dust deposition on telescope mirrors (Burki et al., 1995). Our starphotometers employ off the shelf (amateur) telescopes, with an optical corrector plate sealing off the optical train and being the main contact surface for any particle deposition. The formation of dew, frost or the deposition of clear-sky snow crystals on that plate rep-

resents our greatest source of throughput degradation. Of particular concern is that humidity trapped inside the sealed telescope tube leads to dew or frost formation on the inside of the corrector plate (a degradation which cannot be easily removed by mechanical means). A dramatic event of frost formation, that occurred during the Barrow campaign, (in the absence of a dome or dew cap to protect the telescope), is illustrated in Figure 25. The auto calibrating TSM (c.f. Section

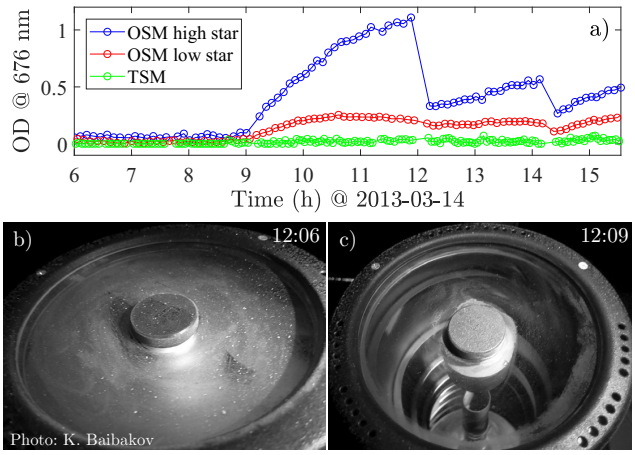

Figure 25. Extreme throughput degradation event caused by frost formation on the telescope corrector plate (Barrow campaign). The TSM auto-calibrating mode, effectively compensates, in real time, for any common-mode throughput degradation (attenuation increase) and accordingly remains largely unaffected by the frost (open green circles on a)). On the other hand, the OSM mode is very sensitive to the apparent attenuation of the high and low stars that constitute the TSM pair (blue and red open circles on a)). The two rapid decreases in the OSM ODs correspond to cleanings at 12:09 at and 14:20. The two photos show the collector plate just prior to and just after the cleaning at 12:09.

3.4.2) used to derive the green OD points, shows little variation. This indicates that there was likely no aerosol and/or significant cloud OD variation during that period. However, the computed OD associated with the individual high and low stars varies strongly and is, based on our photographic evidence, attributable to frost formation on the plate. One should note that the ramping effects in the OD plot result from progressive frost formation and growth, after two separate damp-cloth cleanings. This operation did not apparently remove all the frost (the OD values at the beginnings of the two ramps are higher than those acquired prior to the 09:00 time stamp). One should also note that the low star measurements (red data points) are less affected by the frost: this is because the throughput error, as represented by the OD variation from the baseline, is, as per equation (29), divided by a larger airmass.

While at mid-latitudes one usually uses a dew cap to avoid fogging the optics, in the Arctic it cannot be used since it becomes a container for accumulating snow flakes and renders their mechanical removal difficult. One can usually sublimate the snow and frost from the external side of the corrector plate by closing the dome and increasing the dome temperature by few degrees. However, this doesn't represent the necessary real time solution for preventing throughput degradation. In addition, it doesn't remove any internal telescope frost. Other experiments with limited success were described in Ivănescu et al. (2014). It seemed a rather impossible issue to solve, but a working solution was nevertheless identified, addressing both the frost and incoming crystals: a Kendrick Astro system using a controlled heating band wrapped around the telescope tube. It increases the temperature of the optics, particularly the corrector plate, by up to 10°C with respect to the environment. One expected this to increase the blurring of the star spots due to micro-turbulence near the telescope, but such effect turned out to be negligible for our instruments.

8 Toward 1% accuracy

A relative photometric error of 1% in δ_F/F represents, in turn, a magnitude error of $\delta_S \simeq 0.01$ and an observational error of $\delta_\epsilon = x\delta_\tau = 0.01$. We seek to achieve the $\delta_\epsilon < 0.01$ required accuracy goal discussed in the introduction, by mitigating the non-negligible systematic uncertainties identified in this paper.

8.1 Optimum channel selection

Some of the largest accuracy errors in starphotometry are, as explained in section 4, due to contamination by stellar and Earth atmosphere (also called telluric) absorption lines, photometer spectral drift, bandwidth mismatch between the instrument and catalog references, as well as airglow and aurora contamination, when present. These errors can be mitigated through a judicious channel wavelength selection. Avoiding the high frequency spectral influences is also a reason for having narrow (< 10 nm) channels. Since remote sensing photometry is historically based on sunphotometry and much influenced by AERONET standards (the latest being Version 3 (Giles et al., 2019)), the World Meteorological Organization (WMO, 2016) recommendations for photometric-based aerosol observation includes AERONET (central) wavelengths. For consistency, one should endeavor to select at least a few AERONET bands. Sunphotometry is basically starphotometry based on a spectral class G2 star. Such stars have much weaker hydrogen absorption lines than the typical B and A stars of our catalog. Therefore, our channel selection needs to consider the starphotometry reality, with its specific constraints: mainly to avoid hydrogen (H) lines and insuring a star brightness (particularly challenging in near-infrared) much larger than the sky background. Also, selecting more channels than the sunphotometers may help to compensate for typically larger starphotometer observation

errors. The process of selecting more channels in starphotometry is facilitated by the fact that the number of channels employed by our (spectrometer based) starphotometers is not constrained by the time consuming constraints of an AERONET type rotating filter wheel system. In what follows we attempt to create an OD spectrum with the goal of identifying an optimal starphotometry band set in typical conditions. The method is constrained by an eventual fit to measured OD spectra.

The first step in our band selection process was to identify the spectral intervals free of stellar and aurora/airglow line contamination. To this end, we used the extraterrestrial (HST measured) Vega spectrum (also shown in Section 4), at 8.2 nm bandwidth. Since Vega is a spectral class A0 star, its spectrum, strongly influenced by Balmer and Paschen H lines, is among the most affected by stellar absorption (Silva and Cornell, 1992). Inasmuch as the Vega spectrum can be considered the worst case scenario, the systematic errors due to characteristic stellar absorption bands should be weaker for other stars. In order to obtain only the stellar absorption spectrum, we subtracted the continuum obtained by fitting the magnitude spectrum on off-lines data points. The result shown in Figure 26a was divided by 1.6, to simulate the airmass of an actual star. An IBC2 aurora OD error spectrum with respect to a $V = 2$ star, together with an airglow 10 times larger than that of Figure 15b, was employed to produce the gold "airglow & aurora" curve. The bottom red bars in Figure 26a delineate the spectral intervals to be avoided, where the total of H lines and aurora contaminants are noticeable (> 0.007). For realistic estimates of typical ODs for the most important telluric gaseous absorbers, we used laboratory measured spectra. These included the O_2 of Rothman et al. (2009) adjusted to typical Arctic levels (red curve), the H_2O results of Hill et al. (2013) adjusted to a typical wintertime precipitable water vapour value of 0.8 mm over Eureka (purple curve), and the O_3 results of Voigt et al. (2001) adjusted to 250 DU (blue curve). We neglected the NO_2 contribution, inasmuch as the measurements of Lindenmaier et al. (2011) identified a maximum NO_2 column of 5×10^{15} molecules/cm^2 = 0.19 DU in Eureka in summer-time, representing $\tau_{NO_2} = 0.003$ at $\lambda = 400$ nm, while in wintertime the models estimate it to a much lower value. The cumulative synthetic absorption spectrum of these component contributions is shown in dotted green in Figure 26a. We employed the local minima of this curve as band placement indicators for which errors in ascribing values to the ensemble of absorption contributions (which one must inevitably do to extract an aerosol or cloud OD) would be minimized. A set of 20 new channels (solid black vertical lines) was identified as a potential replacement for the old set of 17 channels (dashed grey vertical lines) currently employed in our starphotometers (it also represents approximately 3 times the number of channels employed in the AERONET instruments). The dotted green curve of Figure 26b shows the same dotted green cumulative spectrum of Figure 26a to which aerosol scattering has been added. The aerosol scattering OD was assumed to vary as per the classical Angstrom expression of $b\lambda^{-a}$, while b was incrementally perturbed until it matched an actual OD Vega spectrum (blue curve) measured at Eureka (a typical value of 1.3 was assumed for a). For reference, the same spectrum but without the stellar components is represented in purple. The position of the 20 new channels are duplicated on Figure 26a in order to better appreciate the final total OD context for those positions.

The selection procedure identifies as many channels as possible, constrained by the avoidance of any absorption line contamination. The ultimate goal is the characterization of the low frequency (slowly varying) aerosol and cloud scattering spectrum. Since there are large spectral intervals where that is not possible (mainly across the O_3, O_2 and H_2O absorption bands), one also needs to include channels that independently facilitate the extraction of O_3 and H_2O column abundances (at least two channels per band, as they are noisier due to the strong absorption). The newly identified central channel wavelengths, as well as their application and their reason for selection, are summarised in Table 2.

The justifications for the 20 selected channels (sequentially ordered as per Table 2) are given below:

Table 2. Specifications for the 20 starphotometry channels chosen according to the absorption feature avoidance process outlined in the text (see the text for details on the reason(s) for selection).

#	Nominal	λ(nm)	Application	Reasons for selection
1	403	403.2	fine-mode[a]	off H Balmer
2	423	422.6	fine-mode	off H Balmer
3	446	445.9	fine-mode	O_3 base, AERONET
4	467	466.7	fine-mode	off H Balmer
5	500	500.3	O_3[b], fine-mode	WMO & AERONET
6	532	532.1	O_3, fine-mode	lidar λ
7	549	548.7	O_3	extra sampling
8	595	595.3	O_3	mid twin-peaks
9	614	614.2	O_3	extra sampling
10	640	640.1	O_3	extra sampling
11	675	675.2	O_3	WMO & AERONET
12	711	711.0	O_3, coarse-mode	extra sampling
13	745	745.0	coarse-mode	O_2 & O_3 baseline
14	778	778.2	coarse-mode	WMO λ
15	845	844.8	coarse-mode	WMO λ
16	879	879.0	coarse-mode	H_2O base
17	936	935.7	H_2O	main peak, off H
18	938	937.9	H_2O	mid twin-peaks, off H
19	989	988.9	coarse-mode	H_2O base
20	1020	1020.2	coarse-mode	AERONET λ

[a] Spectral region that is more sensitive to the characterization of fine-mode (FM) aerosol properties such as FM aerosol OD. The total aerosol OD (FM OD + coarse mode OD) will be sensitive to the presence of FM aerosols.
[b] O_3 absorption is sufficiently strong to provide a retrieval of O_3 columnar abundance and thus O_3 OD from a spectrally dependent matching type of total OD retrieval and accordingly to correct (eliminate) the O_3 OD from the total OD for all O_3-affected channels.

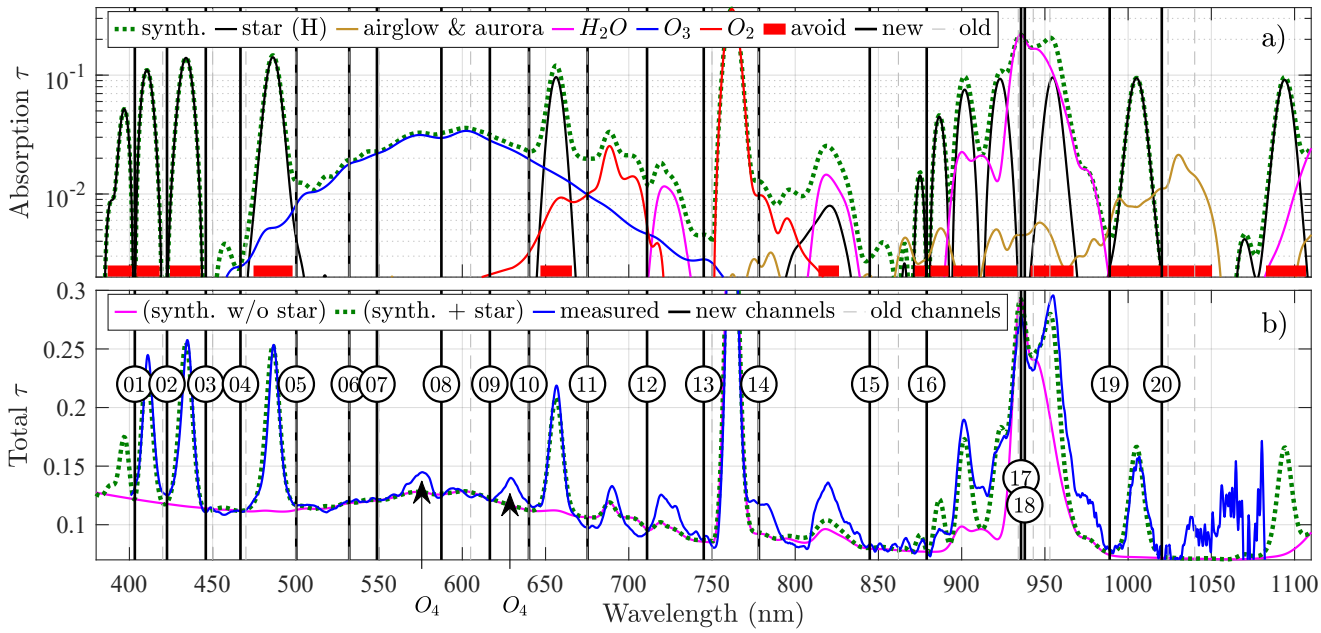

Figure 26. OD spectra of constituents that contaminate the retrieval of aerosol and cloud ODs in the visible and near-infrared. a) Starphotometer channel selection (vertical black lines) obtained by avoiding contaminants, such as the stellar (Vega) absorption OD spectrum (black curve), OD errors associated with airglow and IBC2 aurora (gold curve) as well as O_2 (at least those parts of its red curve whose $OD \simeq 0.01$). The red bars delimit intervals where those contaminants are non-negligible ($\tau > 0.007$). The channel selection also includes strategically selected regions of H_2O and O_3 absorption that allows for the dynamic identification and characterization of their OD and subsequently, their removal from the total OD spectrum. The cumulative contaminant optical depth yields the total synthetic curve (green dotted curve). b) The synthetic curve (with an added aerosol scattering component) versus an OD spectrum (blue curve) retrieved from Vega measurements over Eureka (measured on 2019/11/03 14:01:02). The optimal fit shows generally good agreement except where the contaminant influence is misestimated. This is particularly true for O_4 absorption which we realized, a posteriori, should have been included in the ensemble of contaminants. The numbers of the selected channels are superimposed for reference purposes.

1. Avoidance or minimization of H contamination. It better constraints the UV/blue trend of the fine-mode aerosol spectrum.
2. Avoidance or minimization of H contamination. This is the optimum λ identified in Section 4.
3. Avoidance of an H line, but also the 440 nm emission line identified in section 6.4. This band is near the 440 nm AERONET channel and can be used as the lower bound baseline for isolating the O_3 OD band.
4. Avoidance of an H line. Both 3 and 4 channels are moved a bit left with respect to the current (old) channels, to increase their sensitivity to aerosols.
5. WMO recommendation and an AERONET channel.
6. Lidar standard channel.
7. Good channel for sampling the ozone profile shape while avoiding the 557.7 nm aurora and airglow peak.
8. We note that the difference between the measured and synthetic curves around 590 and 640 nm underscores what appears to be a shortcoming in our synthetic curve: the presence of significant O_4 absorption features (see Wagner et al. (2002) for information on O_4 absorption). Strong O_3 OD channel that lies between double ozone peaks. It's one of 3 bands sensitive to O_3 abundance (and thus O_3 retrieval). It avoids side-bands of O_4 contamination and any possible twilight contamination by 589 nm *Na* flashes (Chamberlain, 1995).
9. Strong O_3 OD channel that also avoids an O_4 line. Same mandate as band 8 (sensitive to O_3 abundance).
10. Avoidance of O_4 and H lines. Useful spectral placement for characterizing the O_3 profile shape. Requires correction for O_2 contamination (note the marginally significant strength of the O_2 OD in Figure 26a).
11. WMO recommendation and an AERONET channel. Requires correction for O_2 contamination.
12. New channel that fills what, up to this point, has been a large spectral gap in atmospheric photometry. Avoidance of a nearby H_2O line. Requires correction for O_2 contamination.
13. Avoidance of the water vapour line at ~ 840 nm and the strongest O_2 line at ~ 761 nm. This channel can be used, respectively, as a lower- and upper-bound baseline for O_2 and O_3 absorption profiles.
14. WMO recommendation channel. Avoidance of the 840 nm H_2O line and the 761 nm O_2 line. Requires correction for O_2 contamination.

15. Avoidance of the 840 nm H_2O line. Requires correction for O_2 contamination. This channel is near the WMO 862 nm recommendation, but the latter may be affected by aurora OD errors.
16. Avoidance of H_2O and H lines. This channel is meant to serve as a lower-bound baseline for the broad H_2O absorption profile that starts around 890 nm.
17. Maximum H_2O absorption (free from H contamination): used for the retrieval of H_2O abundance. The choice of a maximum also minimises the influence of the line shape variation as a function of water vapor abundance (Volz, 1969).
18. Second H_2O channel to improve measurement precision in low starlight flux conditions: due to strong H_2O absorption and generally low starlight flux in near-infrared.
19. Avoidance of H_2O and H lines. This channel is meant to serve as a lower-bound baseline for the broad H_2O absorption profile that ends around 990 nm. It also avoids the region of the strongest aurora- and airglow-induced OD errors.
20. Channel at the largest near infrared wavelength that still provides accurate measurements, while avoiding H lines. Even if this channel is relatively sensitive to airglow emissions, it can be considered reasonably reliable for $V = 0$–1 BA class stars, or bright (and colder) F class stars, such as Procyon, whose near-infrared flux is relatively strong.

The major changes and improvements with respect to the original channel set are: a new 402 nm channel to better estimate the UV attenuation due to fine-mode aerosols; 432 nm channel is optimised for minimal contamination; the ozone absorption profile is over sampled to allow better removal in post-processing; the 953 nm H_2O channel was excluded (see it at the right side peak, on top of the H_2O band, Figure 26a), inasmuch as it is likely influenced by a H Paschen line; the H_2O baseline is better estimated with more strategically selected baseline channels (closer to the limits of significant absorption); the original (persistently noisy) 1040 nm channel was excluded (the high frequency variations seen in the retrieved ODs above approximately 1030 nm in Figure 26b is a symptom of the noisy nature of signals in that region of the near infrared). In order to avoid near-IR airglow one needs only acquire data at wavelengths above 1050 nm: this however results in weaker star flux and the above-mentioned weak signal to noise. Finally, we remind that our channel selection process is optimized for the peculiarities of our starphotometer. Signal to noise considerations aside, the spectral bandwidth is one of those peculiarities : different bandwidths may require slightly different channels.

8.2 Starphotometry recommendations

We recommend the general usage of the 20 starphotometry channels defined in the previous section. Those channels are dedicated to the extraction of aerosol and/or cloud ODs as well as the strong molecular absorbers of O_3 and H_2O (either as corrections to achieve estimates of aerosol and cloud ODs or, as remote sensing targets on their own merit).

An important source of OD error is related to the accuracy of the spectrophotometric catalog. In the case of the Pulkovo catalog, we identified a particularly large bias in the UV and 900–1000 nm regions (c.f. the text associated with Figure 4), that could distort the retrieved aerosol spectrum. That bias aside, the errors in the individual star spectra are also prohibitive in terms of achieving the required accuracy. It is strongly recommended that a new and improved bright star catalog should be made, preferably with magnitude measurements acquired by a space-based instrument, to avoid the incertitude related to telluric absorption contributions. As discussed in Section 4, the requirements for such a catalog are 1 nm bandwidth and < 1 nm (preferably 1 Å) spectral resolution. In the mean time, we continue to use the Pulkovo catalog, but with its 8.2 nm bandwidth version that improves the bandwidth match with our instruments, and offers a wider bright star diversity than what is currently provided by HST. Alternatively, if the starphotometer is spectrometer-based, as is our starphotometer, then one can generate such a catalog from direct high resolution observations (all spectrometer channels) at a high altitude site. Such a catalog would perfectly match the instrument bandwidth. We recommend, that future starphotometer bandwidths be held to less than 10 nm : this is an easily attainable standard that ensures negligible heterochromatic errors ($\delta_\tau < 0.001$). The employment of all the spectrometer channels ensures that any high resolution stellar features can be properly accounted for in future corrections of any spectral drift (before extracting a drift-modified set of optimized operational set of starphotometer channels). Observations and calibration should be preferentially performed with a B0–B3 (early-type B) star, or A7–A9 (late-type A) and F stars, to avoid the incertitudes related to the strong stellar absorption lines. Also, spectral calibration, clearly becomes a necessity in the face of spectral drift: results like those of Figure 8 indicate that they must be performed every few months, or annually for short observing seasons. Alternatively, one may simply record every few months a high resolution spectrum of Vega, which will serve as reference for spectral calibration in post-processing.

One particular concern at mid-latitudes locations, is that NO_2 may be several times larger (Cede et al., 2006) than Eureka (i.e. up to 0.03 OD at 400 nm) and its absorption will be no longer negligible. Since NO_2 absorption is impossible to discriminate from aerosol spectrum, it has to be assessed from independent sources.

Retrievals in the presence of rapid temporal variations of sky brightness (a measurement which must accompany every

star measurement) must be corrected by interpolating from pre- an post-contaminated sky brightness measurements to the time of the star measurement. Signals greater than the threshold for the onset of non-linearity (8000 cnt/s in the case of our starphotometer) should be discarded (Section 7.2). In such bright sky conditions, one may expect OD errors > 0.017, unless interpolating the sky brightness to the time-stamps of star measurements. One should be aware that, at sky brightness increase, the blue part of the spectrum saturates first, leading to a distorted aerosol spectrum retrieval.

Airmass accuracy should be ensured by the use of a GPS time server. OD errors associated with airmass uncertainties can also be reduced at a high altitude site, while they remain sensitive to time errors on low stars, i.e. at large x (c.f. Figure 12). The internal instrument temperature should be monitored, inasmuch as the temperature controller may eventually fail (for example, at the very low environmental temperatures found in the Arctic). One particularly needs to wait for the system to warm up to its stabilised range, as the low temperatures have a larger error impact (c.f. Section 7.5).

The stability of the throughput has fundamental impact on the calibration process. Due to the excessively small FOV of the SPST09/C11 configuration ($36.9''$), the optical alignment proved to be critical to ensuring stable throughput. As demonstrated in the discussion surrounding Figure 18, the centering tolerance error should not exceed $4''$ for this instrument in Eureka (2 CCD bins). The focusing error of SPST09/C11 should always be within one step adjustment step (confusion circle variation of $\sim 10''$/step, as per the legend of Figure 17). This means, for example, that the focus must be adjusted by one step for each 10°C change in outside temperature.

Turbulence analysis using star spot imaging revealed another large source of throughput degradation, which is acerbated at Arctic sea-level sites: possible vignetting of star spots at large airmasses. This problem was ascribed to the small SPST09/C11 FOV in the context of the excessively larger seeing of Eureka. The worst case ($m = 10$) scenario of the red curve in Figure 2 (for which the star spot is $\omega \simeq 19''$) can be accomodated by a FOV of $2.3\omega \simeq 45''$ (see Appendix C for details). In the light of the forward scattering error analysis, one should not increase it beyond $\sim 47''$ (roughly where the mean of the most demanding cases of Figure 14, the "120 mm (ASC) ice cloud" case, crosses the 0.01 value of the δ_τ/τ axis). This FOV limitation also ensures accurate measurements (sub 1% errors associated with the brightness contamination cases of Figures 15 and 16) during faint aurora (IBC2) events (or their illumination-equivalence of thin moonlit cirrus clouds) for even weak ($V = 3$) stars (with the near infrared exception of Figure 16 where a bright, $V = 0$ star such as Vega, is needed to achieve the 1% threshold). A $45''$ FOV, which would be obtained with a 0.61 mm diaphragm in the C11 case, therefore appears to be good compromise between the conflicting requirements of maximizing the FOV to accommodate all star spot sizes (red curve of Figure 2) and limiting the FOV to minimize the largest forward scattering errors (blue curves of Figure 14). The small FOVs employed in starphotometry ensure that this technique is significantly less dependent on the intrinsic and artificial OD reduction induced by scattering into the FOV by optically thin clouds. This singular capability of starphotometry renders it rather unique in extinction-based photometry inasmuch as sun- and moon-based techniques require (or at least traditionally use) much larger FOVs and accordingly suffer from much larger FOV scattering contamination.

We demonstrated (Section 7.1) that observations at airmasses higher than ~ 5 should not be made with the C11 because of the influence of vignetting. Calibration may nevertheless be performed beyond this airmass limit, as long the S values still show a linear dependence on x. This may happen in weaker air turbulence conditions than those of Figure 2. Throughput degradation due to frost/dew or ice crystals deposition on the telescope was a longstanding problem of our Eureka starphotometer (with critical accuracy implications). The use of the Kendrick system (or similar heating bands), together with a small wind shield, proved to be a reliable solution which would be appropriate for most of Arctic observing sites.

If all these recommendations are followed, one may aspire to achieve a reduction of each zenith OD error component to well bellow 0.01 and the total zenith OD error to $\lesssim 0.01$ (i.e. the stated 1% photometric accuracy). Even if these goals are, in certain cases still under development, any progress that substantially approaches the goal of 0.01 total zenith OD error would represent a significant advance in starphotometry reliability.

9 Conclusions

With the the ultimate goal of improving starphotometry accuracy, we analysed a large variety of sources leading to systematic (absolute) errors and classified them by their impact on each parameter involved in the optical depth retrieval. The contamination from stellar and telluric gas absorption lines may potentially induce large OD errors. One of the newly identified contaminants are O_4 absorption lines, that affect O_3 estimation and removal, leading to distorted aerosol OD spectrum. Such errors are nevertheless mitigated with proper channel allocation: this we demonstrated using synthetic and measured OD spectra to extract a set of 20 optimal channels. In order to minimize further the absorption lines induced OD errors (stronger hydrogen lines tend to spill over into different bands), one may favour the starphotometry observations using early-type B, late-type A and F spectral class stars, that have weaker hydrogen absorption lines. Therefore, we may particularly prefer them for calibration purposes.

Inaccuracies in the current exoatmospheric photometric catalog can be partly addressed in the TSM observation mode, where the catalog bias is cancelled out, or by com-

pletely avoiding it through a lengthy calibration involving each star that one wishes to employ as an extinction target. Given such restrictive options, the community is strongly encouraged to prioritise the development of a new spectrophotometric catalog with improved accuracy. This will increase confidence in the accuracy of a star independent calibration, and render that approach more operational and reliable. Alternatively, one may generate an instrument-specific catalog, from direct observations at a high altitude site (where one may also perform the calibration).

Problems related to the instrument instability (including spectral drift and star spot vignetting) were identified and appropriate observation strategies and design improvements were proposed. Beyond the current accuracy assessment study, we will pursue starphotometry reliability improvement by also characterising the non-systematic, random errors, as well as those related to C values retrievals through Langley plot calibration. A sky brightness model to estimate the background of moonlit and twilight lit clouds is in development. A new exoatmospheric photometric catalog based on GOMOS satellite photometry is also envisioned. In order to validate the proposed improvements, one should participate in observing campaigns and compare the observations with other collocated instruments. The CIMEL moonphotometer and the profiling backscatter lidar at our Eureka site are collocated instruments that already provide support of this nature.

As a side-derivation of this study, in Section 2, equation (1), we developed an original estimation of the astronomical seeing from radiosondes measurements.

Code and data availability. The displayed data, as well as the plot codes are available upon request from the authors (Liviu.Ivanescu@usherbrooke.ca).

Appendix A: The Canadian starphotometry program

Our group at the Université de Sherbrooke has been performing starphotometry observations of aerosols and optically thin clouds in Canada and elsewhere since 2007. There have been a total of three Canadian sites in our small starphotometer network (the high latitude site at Eureka, Nunavut, and mid-latitude sites at Sherbrooke, Québec and Egbert, Ontario). Currently the network has been reduced to the Eureka and Sherbrooke sites. Additionally, campaign-based observations took place in Halifax (NS), Barrow (Alaska, USA) and Izaña (Canary Islands, Spain).

A1 The instruments

Our starphotometers were built by Dr. Schulz & Partner GmbH, a German company that has now ceased operations. The existing instrument versions in the network are the SPST05 at Sherbrooke, the SPST06 version which was formerly at Egbert and now at Sherbrooke and the SPST09 version at Eureka. The detection device inside all those models is the QE65000 scientific-grade spectrometer from Ocean Optics. It's based on a Hamamatsu S7031-1006 CCD sensor (1044×64 pixels). We use two different telescope models, both having an $f_{\#} = f/D = 10$ focal ratio, where f is the focal length and D the diameter.

The telescope "plate scale" P_s on the focal plane, can be computed (Carroll and Ostlie, 2007) with

$$P_s = k_c/f = k_c/(D \cdot f_{\#})$$

where P_s is expressed in ($''$/mm), with $k_c = 3600 \cdot 360/(2\pi) = 206264.8$ ($''/rad$), being a radian to ($''$) conversion factor, and f and D in mm. Our version to version instrument improvements concern mainly the robustness of the instrument. However, the throughput of the SPST09 instrument is a factor of 3.2 better than previous versions due to the use of an 11 inch (279.4 mm) diameter C11 Schmidt-Cassegrain telescope made by Celestron, with Starbright XLT coating and a 98 mm diameter central obstruction due to the secondary mirror (11.5% of the primary mirror surface). The previous models used a 7 inch (177.8 mm) Alter M703 Maksutov-Cassegrain telescope made by the Russian company Intes Micro, with 32% central obstruction (100 mm diameter). The internal optics of the SPST09 are currently coated with Melles Griot, Extended HEBBAR^{TM} coating. By comparison, the previous versions have custom coatings with about 3 mag. throughput loss around 500 nm, but with about 1 mag. gain in the infrared. They perform measurements simultaneously across 1000 channels along the 1044 pixels of the CCD (from which only 17 were selected by the manufacturer as standard for regular operation, see Table 1). Night sky radiance for background subtraction from the stellar signal is measured by pointing the photometer about $8'$ (arcminutes) off-target. The star-acquisition procedure is based on star centering by two auxiliary SBIG ST-402ME-C2 CCD cameras. One uses a square 504×504 pixels (px) sub-frame, out of the original 510×765 px CCD. For speed and sensitivity, the acquisition mode is using 3×3 bins of 9 μm square pixels (i.e. 27×27 μm bins). The initial wide field centering uses a 67 mm diameter refractive auxiliary telescope with a fast $f_{\#} = 4$ focal ratio. With a $P_s = 12.65'$/mm plate scale, it provides a $57.4'$ field of view (FOV) on its camera, with $20.5''$/bin (arc-seconds per 3 pixel bin). The subsequent centering is done at high angular resolution, using the main telescope. For the C11 telescope, at $P_s = 73.7''$/mm plate scale, one has a $5.6'$ FOV, at $2''$/bin. For the M703 telescope, at $P_s = 114.6''$/mm plate scale, on has a $8.3'$ FOV, at $3''$/bin. Based on the Nyquist-Shannon sampling theorem (Shannon, 1948), one can track star spots at the maximum precision of 1 bin if one has at least one bin per standard deviation (Robertson, 2017), or 2.355 bins per Full Width at Half Maximum (FWHM). This would be the case for FWHMs larger than $4.7''$ for C11 and $7.1''$ for M703. We will see later that this is more than adequate for C11, but borderline for M703. To avoid contamination from off-target objects, one limits the

measured FOV with a 0.5 mm diameter diaphragm, at the telescope focus. Based on the corresponding plate scale, this means that the spectrometer, i.e. the actual detector, has a 36.9″ FOV for C11 and 57.3″ FOV for M703. The star light is then refocused on a 400 μm diameter optical fiber, which feeds the QE65000 grating spectrometer through a 200 μm wide slit. The diffraction profile, on the spectrometer 1044 pixels long CCD, covers several pixels, at ~ 0.75 nm/px. In order to improve the measurement accuracy, one averages 5 pixels (± 2 around the central one). The convolution of the slit function with the averaged pixels leads to a profile having FWHM$\simeq 8.2$ nm, or 11 pixels, representing the bandwidth measured in section 4. Assuming it a Gaussian shape, each channel may get $> 1\%$ influence from about 10 nm around. The measurement also implies averaging several (usually 3 or 5) 6 seconds exposures, simultaneously on all channels. Other technical parameters are also listed in Table 1.

All instruments are protected by astronomical domes. In Sherbrooke there is a 12 ft Astrohaven dome, while in Egbert there is a 7 ft dome fabricated by the same maker. In Eureka there is a 10 m diameter dome built especially for the Arctic by the German company Baader Planetarium (Figure 1). The tracking system (the telescope mount), in the case of Sherbrooke and Egbert instruments, is the Losmandy G-11 German equatorial mount. For Eureka there is an AZA-2000 Dobsonian alt-azimuth mount, especially built for the Arctic by the Italian company 10Micron.

A2 Observing sites

The Sherbrooke, Quebec, site is located near the Université de Sherbrooke campus, on the roof of the observation station SIRENE ("Site Interdisciplinaire de REcherche en ENvironnement Extérieur"), at coordinates 45.374°N, 71.923°W, and ground elevation + instrument height of 308 + 6 m ASL (above sea level). The Egbert, Ontario, site was at the Environment Canada "Centre for Atmospheric Research Experiments" (44.232°N, 79.781°W, 251+6 m ASL), located 65 km North of Toronto, Ontario.

The Eureka, Nunavut site (79.991°N, 85.939°W, 10+2 m ASL), at the Zero Altitude PEARL Auxiliary Laboratory (0PAL), near the Environment Canada Eureka Weather Station, is our most prolific data provider. Polar nightime data (i.e. winter time, roughly late September to late March) was acquired there from 2008 to 2010 using the SPST05/M703 instrument, followed by its upgraded version SPST09/C11. The latter instrument collected data for about two months during each observing seasons until 2014 (Ivănescu et al., 2014), with a gap in 2012-2013. After overcoming several technical difficulties, the acquisition period extended to 3-4 months from 2015 onwards.

The Halifax site was on the roof of the Sir James Dunn Building (44.638°N, 63.593°W, 45+6 m ASL), at Dalhousie University. Two weeks of data were acquired there with SPST05/M703 during the July 2011 BORTAS campaign ("BOReal forest fires on Tropospheric oxidants over the Atlantic using Aircraft and Satellites"). Outside of Canada, we performed SPST06/M703 observations, for about a week, in October 2008, at the "Izaña Atmospheric Research Center" in Tenerife, Canary Islands, Spain (28.309°N, 16.499°W, 2390+1 m ASL). In March 2013, we carried out a SPST05/M703 field campaign at the Barrow, Alaska Observatory, USA (71.323°N, 156.611°W, 11+2 m ASL).

Appendix B: Star dataset

Our 20 stars dataset for the Northern Hemisphere is presented in the table B0, essentially selected for being stable stars and having their declination higher than about -23.5°, to account for Earth axis inclination. We usually refer to those stars by their HR labels, standing for their index in the Bright Star catalog (label legacy from the Harvard Revised Photometry Catalog). For facilitating their identification, we also present their index HIP in the Hipparcos catalog. The following columns present their affiliated constellation and rank, their usual name, Right Ascension (RA) and Declination (DE) coordinates at epoch 2000, visual magnitude and spectral class. From them, 13 are usually present in the Arctic sky, having positive declination. They are identified in the last column of the table as High and Low, standing for their status during the TSM measurements (see section 3.4.2 for explanation). One always can form a pair from those 13 stars in order to observe around the clock in TSM mode.

With a constraint of having pairs of the same spectral type, as emphasised in the section 4, in the Arctic we may then use the A type pair HR 7001-7557, and the B type pairs HR 1791-1790 and HR 5191-3982. These pairs have similar Right Ascension (basically, closely located in azimuth) and, together, cover the entire 24 h period, while keeping the airmass smaller than 6 for low stars. Unfortunately, they are not of similar spectral subtype, but this can be achieved tough for the pair HR 5191-1790, both stars being of early-type B.

Appendix C: FOV constraints

The long exposure PSF, i.e. the star spot blurring due to atmospheric turbulence, can be approximated with a Gaussian profile (Racine, 1996), where the FWHM$\simeq \omega$ and standard deviation $\sigma = \omega/2.355$. A large part of the PSF is due to random spot movements, called jitter (θ). As we continuously track the short 6 second exposures, the low frequency part of that jitter (θ_L), being compensated for, should not longer blur the star spot fed into the photometer. We estimate $\sigma^2_{\theta_L}$ by integrating, from 0 up to the tracking bandwidth, the one-axis jitter power spectrum, i.e. half of the low-frequency value given in equation (15) of Glindemann (1997). When the tracking bandwidth tends to the sampling frequency ($1/t$),

Table B0. Stable star selection from the Northern Hemisphere bright stars

HR	HIP	Rank Constellation	Name	RA(2000)	DE(2000)	V	Sp/Lum	TSM
15	677	Alpha Andromeda	Alpheratz	00:08:23	29°05:26	2.06	B8I/Vp	High
1790	25336	Gamma Orion	Bellatrix	05:25:08	06°20:59	1.64	B2/III	Low
1791	25428	Beta Taurus	Elnath	05:26:18	28°36:27	1.65	B7/III	High
2004	27366	Kappa Orion	Saiph	05:47:45	–09°40:11	2.06	B0.5/Ia	-
2421	31681	Gamma Gemini	Alhena	06:37:43	16°23:57	1.93	A0/IV	Low
2491	32349	Alpha Canis Major	Sirius	06:45:09	–16°42:58	–1.46	A1/Vm	-
2618	33579	Epsilon Canis Major	Adharaz	06:58:37	–28°58:20	1.50	B2/II	-
2943	37279	Alpha Canis Minor	Procyon	07:39:18	05°13:30	0.38	F5/IV-V	Low
3982	49669	Alpha Leo	Regulus	10:08:22	11°58:02	1.35	B7/V	Low
4295	53910	Beta Ursa Major	Merak	11:01:50	56°22:57	2.37	A1/V	High
4534	57632	Beta Leo	Denebola	11:49:04	14°34:19	2.14	A3/V	Low
4662	59803	Gamma Corvus	Gienah	12:15:48	–17°32:31	2.59	B8/IIIp	-
5191	67301	Eta Ursa Major	Alkaid	13:47:32	49°18:48	1.86	B3/V	High
6378	84012	Eta Ophiuchus	Sabik	17:10:23	–15°43:29	2.43	A2/V	-
6556	86032	Alpha Ophiuchus	Rasalhague	17:34:56	12°33:36	2.08	A5/III	Low
7001	91262	Alpha Lyra	Vega	18:36:56	38°47:01	0.03	A0/Va	High
7121	92855	Sigma Sagittarius	Nunki	18:55:20	–26°17:43	2.02	B2.5/V	-
7557	97649	Alpha Aquila	Altair	19:50:47	08°52:06	0.77	A7/V	Low
8728	113368	Alpha Pisces Australids	Formalhaut	22:57:42	–29°37:01	1.16	A3/V	-
8781	113963	Alpha Pegasus	Markab	23:04:49	15°12:38	2.49	B9/V	Low

the missing jitter contribution to ω is

$$\omega_{\theta_L} = 2.355 \cdot \sigma_{\theta_L} = 0.917 \left(\frac{r_0}{vt}\right)^{1/6} \omega \quad \text{(C1)}$$

The turbulence length parameter was found to be $r_0 \simeq 0.01$ m for Eureka (section 2) and $v \simeq 10$ m/s is the typical effective wind speed. Then, for $t = 6$ s,

$$\omega_{\theta_L} = 0.215 \cdot \omega \quad \text{(C2)}$$

Depending on the tracking system performance, its bandwidth may even be a factor 10 slower (Glindemann, 1997) than the sampling frequency, i.e. $0.1/t$. In such case $\omega_{\theta_L} \simeq 0.15 \cdot \omega$. The FWHM of the short exposure spot, in a Kolmogorov turbulence, is then $\omega_s = (\omega^{5/3} - \omega_{\theta_L}^{5/3})^{3/5} \simeq 0.95 \cdot \omega$ or more. It means that the tracking basically applies a negligible correction to ω. The average of ω_s in Figure 2 shows a slightly larger difference though, consistent with a shorter integration time than 6 s.

Based on the equations (77) from Tyler (1994) and (5) from Racine (1996), the one-axis standard deviation of the total jitter σ_θ is

$$\sigma_\theta = 0.42 \cdot (\lambda/D)^{1/6} \cdot \omega^{5/6} \quad \text{(C3)}$$

For our instruments and telescopes $(\lambda/D)^{1/6} \simeq 1''$. In addition, for ω in the range 5-15$''$, as shown for $m < 5$ in Figure 2, $\omega^{5/6} \simeq 0.7 \cdot \omega$. Then

$$\sigma_\theta \simeq 0.4 \cdot \omega^{5/6} \simeq 0.3 \cdot \omega \quad \text{(C4)}$$

Removing its low-frequency part, $(\sigma_\theta^2 - \sigma_{\theta_L}^2)^{1/2} \simeq 0.29 \cdot \omega$, underscores again negligible impact of the tracking. We can thus characterize the spot to spot (exposure to exposure) displacement of a star due to the turbulence-induced jitter (σ_θ), as a function of the ω characterization of the site (Figure 2). Given a Gaussian probability for the random jitter, centering, for example, with a tolerance $\delta_c = \sigma_\theta$ would ensure that, once centered, about 2/3 of the subsequent measurements will still find the star centered. For the long exposure observations presented in Figure 2, at $m = 5$ one has $\omega = 14.7''$ in the Arctic with the C11 telescope and $\omega = 8.9''$ at mid latitudes with M703. That implies a tolerance δ_c of 4.4$''$ and 2.7$''$, or roughly 2 and 1 pixels, respectively, on the high-resolution SBIG cameras. This is consistent with the $\omega/4$ rule of thumb suggestion of Baudat (2017) as the acceptable tracking error. In Figure C1 one shows the C11 telescope tracking configuration of the short exposure spots, with $4'' = 2$ pixels centering error, and with 3 choices of centering tolerance. The ω_s spot sizes correspond to the blue line of Figure 2. It emphasises the loss of flux beyond FOV, especially for low stars. Based on the Gaussian approximation of the star spot, one can compute that 1% of the flux is lost if the FOV is $2.4 \cdot \omega_s = 2.3 \cdot \omega$. One limits therefore the flux loss to 1% if the star spots have $\omega <$ FOV$/2.3$. This means 26$''$ for M703 telescope, or more than what the seeing was ever observed. However, in the Arctic the same calculation gives 16.7$''$ as the maximum seeing that one can accommodate for a perfectly centred star, by using the C11 telescope. This becomes critical since as it's already close to the spot sizes at airmass $m = 5$ shown in Figure 2.

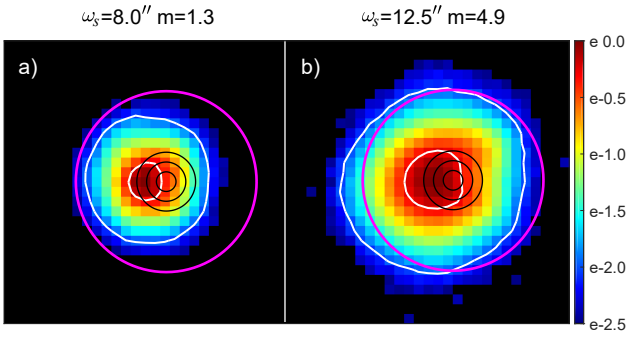

Figure C1. Tracking 6 s short exposure spots of high stars (a) and low star (b), for SPST09/C11. The spots are normalised to maximum flux and presented in log scale. The FOV is the magenta circle, the flux levels of 1% and 50% (where FWHM$\simeq \omega_s$ is measured) are in white contours, while 3 choices of centring tolerance (2, 4 and 6″) are on the 3 black concentric circles. The spots are horizontally shifted with respect to FOV, corresponding to 4″ centring error.

Appendix D: Symbols and Acronyms

C11	Celestron C11 Schmidt-Cassegrain telescope
M703	Alter M703 Maksutov-Cassegrain telescope made by Intes Micro
SPST05	starphotometer version 5 made by Dr. Schulz & Partner GmbH
SPST06	starphotometer version 6
SPST09	starphotometer version 9
D	telescope diameter
f	telescope focal length
$f_\#$	telescope focal number (focal ratio)
P_s	telescope plate scale
FOV	telescope/instrument field of view
FWHM	Full Width at Half Maximum
px	pixel
bin	several pixels read together
″	arc seconds
′	arc minute
e^-	electron
e	Euler's natural number
ADU	analog-digital unit
ASL	above sea level
PSF	Point Spread Function
ω	FWHM of the turbulence contribution to the long exposure star spot
ω_s	FWHM of the turbulence contribution to the short exposure star spot
ω_d	FWHM of the diffraction contribution to the star spot
r_0	length parameter of the turbulence
λ	wavelength
k_c	conversion factor radians to arc-seconds
k_t	turbulence parametrization constant
v	wind speed
n	refraction index
k	absorption index
dn	atmospheric layer contribution to n
cnt	counts, instrument measurement unit
θ	zenith angle
I_0, I	extra-atmospheric and attenuated star irradiances in absolute units
M_0, M	absolute extra-atmospheric and attenuated magnitudes
F_0, F	extra-atmospheric and attenuated star flux measurement
S_0, S	instrumental extra-atmospheric and attenuated magnitudes
$I_{0,c}$, $I_{0,s}$	exoatmospheric absolute irradiance of the catalog & instrument references
$F_{0,c}$, $F_{0,s}$	exoatmospheric instrument measurement of the catalog & instrument references
$M_{0,c}$,$M_{0,s}$	exoatmospheric catalog magnitude of the catalog & instrument references
$S_{0,c}$, $S_{0,s}$	exoatmospheric instrument magnitude of the catalog & instrument references
m	airmass
x	$m/0.921$
τ	atmospheric optical depth
OD	atmospheric optical depth
OSM	One-Star Method of observation
TSM	Two-Star Method of observation
c	instrument specific photometric conversion factor
c_r	ratio of photometric system references
C	instrument specific photometric calibration parameter
ϵ	observation error
δ_ϵ, δ_τ	systematic observation and τ errors
δ_{M_0}, δ_x	systematic errors on M_0 and x
δ_S, δ_C	systematic errors on S and C
δ_t	systematic error on time
R	instrument measurement of the star irradiance
B	instrument measurement of the sky background
δ_F	systematic errors on F
δ_R, δ_B	systematic errors on R and B
g	ADU conversion factor
h	observatory altitude ASL
t	duration of an exposure
δ_c	star centering tolerance
V	M_0 over the standard (visual) V filter
U, B, J	as V, but for U, B, J filters
px	pixel
ZP	zero-point of photometric system
z, z_t	apparent and true zenith angles
P	scattering phase function
Ω	FOV/2

$\Delta\Omega$	solid FOV angle
$P\Delta\Omega$	normalised P over $\Delta\Omega$
$\overline{\omega}$	Single Scattering Albedo
SSA	Single Scattering Albedo
IBC1–4	aurora brightness classes
R	Rayleigh unit
s	star spot off-axis or off-focus position
F_e	expected star signal when measured at standard stabilised temperature
AERONET	AErosol RObotic NETwork of Cimel sunphotometers
WMO	World Meteorological Organization
Sp	spectral class of stars
A,B,F,G	spectral class of stars
Lum	luminosity class of stars
HR	Harvard Revised Photometry star catalog
HIP	Hipparcos star catalog
RA(2000)	Right Ascension at epoch 2000
DEC(2000)	DEClination at epoch 2000
σ	standard deviation
θ, θ_L	one-axis star spot jitter, low frequency jitter
σ_{θ_L}	standard deviation of low frequency jitter
ω_{θ_L}	FWHM of low frequency jitter
σ_θ	one-axis standard deviation of the total jitter
rad	radians
DU	Dobson Unit
TEC	Thermo-Electric Cooler

Author contributions. L. Ivănescu and K. Baibakov developed the observing facilities in Eureka and Sherbrooke, respectively. L. Ivănescu performed the data acquisition in Eureka, while K. Baibakov did it in Sherbrooke, Barrow and Izaña. K.-H. Schulz built the starphotometer instruments and participated in the Eureka SPST09/C11 commissioning. L. Ivănescu developed the post-processing and plotting code. L. Ivănescu prepared the manuscript with contributions from the other authors. N. O'Neill performed an in depth text proofing. N. O'Neill and J.-P. Blanchet supported financially this work from various founding organisms.

Competing interests. No competing interests are present.

Acknowledgements. This work was supported logistically and financially by CANDAC (the Canadian Network for the Detection of Atmospheric Change) through PAHA (Probing the Atmosphere of the High Arctic) funding, by the NSERC CREATE Training Program in Arctic Atmospheric Science, by the FAST programs of the CSA (Canadian Space Agency) and by NETCARE (Network on Climate and Aerosols: Addressing Key Uncertainties in Remote Canadian Environments).

References

AiryLab: Measurement Report for Celestron C11 Telescope, Tech. rep., AiryLab, https://www.airylab.com/contenu/mesures/astro/rapport2012-10002-a.pdf, 2012.

Alekseeva, G. A.: The determination of atmospheric extinction by the stellar magnitude differences method in stellar spectrophotometry, Izvestiya Glavnoj Astronomicheskoj Observatorii v Pulkove, 198, 18–21, http://adsabs.harvard.edu/abs/1980IzPul.198...18A, 1980.

Alekseeva, G. A., Galkin, V. D., Nikanorova, I. N., and Novikov, V. V.: A Spectrophotometric Catalogue of 60 Selected Southern Stars, Baltic Astronomy, 3, 361, https://doi.org/10.1515/astro-1994-0405, 1994.

Alekseeva, G. A., Arkharov, A. A., Galkin, V. D., Hagen-Thorn, E., Nikanorova, I., Novikov, V. V., Novopashenny, V., Pakhomov, V., Ruban, E., and Shchegolev, D.: The Pulkovo Spectrophotometric Catalog of Bright Stars in the Range from 320 TO 1080 NM, Baltic Astronomy, 5, 603–838, http://adsabs.harvard.edu/abs/1997BaltA...6..481A, 1996.

ASTM-G173-03: Standard Tables for Reference Solar Spectral Irradiances: Direct Normal and Hemispherical on 37° Tilted Surface, https://doi.org/10.1520/G0173-03R12, 2012.

Baibakov, K., O'Neill, N. T., Firanski, B., and Strawbridge, K.: Preliminary Analysis of Night-time Aerosol Optical Depth Retrievals at a Rural, Near-urban Site in Southern Canada, AIP Conference Proceedings, 3–8 August 2008, Foz do Iguaçu, Brazil, 1100, 443, https://doi.org/10.1063/1.3117015, 2009.

Baibakov, K., O'Neill, N. T., Ivănescu, L., Duck, T. J., Perro, C., Herber, A., Schulz, K.-H., and Schrems, O.: Synchronous polar winter starphotometry and lidar measurements at a High Arctic station, Atmospheric Measurement Techniques, 8, 3789–3809, https://doi.org/10.5194/amt-8-3789-2015, 2015.

Baker, D. J.: Rayleigh, the Unit for Light Radiance, Applied Optics, 13, 2160, https://doi.org/10.1364/AO.13.002160, 1974.

Baudat, G.: Full Frame Guiding and Focusing, in: Northeast Astro-Imaging Conference, 2017.

Baum, B. A., Yang, P., Heymsfield, A. J., Bansemer, A., Cole, B. H., Merrelli, A., Schmitt, C., and Wang, C.: Ice cloud single-scattering property models with the full phase matrix at wavelengths from 0.2 to 100μm, Journal of Quantitative Spectroscopy and Radiative Transfer, 146, 123–139, https://doi.org/10.1016/j.jqsrt.2014.02.029, 2014.

Bessell, M. S.: Standard Photometric Systems, Annual Review of Astronomy and Astrophysics, 43, 293–336, https://doi.org/10.1146/annurev.astro.41.082801.100251, 2005.

Bohlin, R. C.: Hubble Space Telescope CALSPEC Flux Standards: Sirius (and Vega), The Astronomical Journal, 147, 127, https://doi.org/10.1088/0004-6256/147/6/127, 2014.

Bohlin, R. C., Dickinson, M. E., and Calzetti, D.: Spectrophotometric Standards from the Far-Ultraviolet to the Near-Infrared: STIS and NICMOS Fluxes, The Astronomical Journal, 122, 2118–2128, https://doi.org/10.1086/323137, 2001.

Bohlin, R. C., Gordon, K. D., and Tremblay, P.-E.: Techniques and Review of Absolute Flux Calibration from the Ultraviolet to the Mid-Infrared, Publications of the Astronomical Society of the Pacific, 126, 711–732, https://doi.org/10.1086/677655, 2014.

Brown, A. G. A., Vallenari, A., and Prust, T.: Gaia Data Release 2, Astronomy and Astrophysics, 616, A1, https://doi.org/10.1051/0004-6361/201833051, 2018.

Bucholtz, A.: Rayleigh-scattering calculations for the terrestrial atmosphere, Appl. Opt., 34, 2765–2773, https://doi.org/10.1364/AO.34.002765, 1995.

Burki, G., Rufener, F., Burnet, M., Richard, C., Blecha, A., and Bratschi, P.: The atmospheric extinction at the E.S.O. La Silla observatory., Astronomy and Astrophysics Supplement, 112, 383, http://adsabs.harvard.edu/abs/1995A%26AS..112..383B, 1995.

Cachorro, V. E., Romero, P. M., Toledano, C., Cuevas, E., and de Frutos, A. M.: The fictitious diurnal cycle of aerosol optical depth: A new approach for "in situ" calibration and correction of AOD data series, Geophysical Research Letters, 31, https://doi.org/10.1029/2004GL019651, 2004.

Carlund, T., Landelius, T., and Josefsson, W.: Comparison and Uncertainty of Aerosol Optical Depth Estimates Derived from Spectral and Broadband Measurements, https://doi.org/10.2307/26185872, 2003.

Carroll, B. W. and Ostlie, D. A.: An Introduction to Modern Astrophysics, Pearson Education, Inc., Addison Wesley, 2nd edn., www.worldcat.org/oclc/69020924, 2007.

Cede, A., Herman, J., Richter, A., Krotkov, N., and Burrows, J.: Measurements of nitrogen dioxide total column amounts using a Brewer double spectrophotometer in direct Sun mode, Journal of Geophysical Research, 111, D05 304, https://doi.org/10.1029/2005JD006585, http://doi.wiley.com/10.1029/2005JD006585, 2006.

Chamberlain, J. W.: Physics of the Aurora and Airglow, AGU, Washington D.C., 2nd edn., www.worldcat.org/oclc/7322577597, 1995.

Chattopadhyay, R. and Midya, S. K.: Airglow emissions : fundamentals of theory and experiment, Indian Journal of Physics, 80, 115–166, http://arxiv.iacs.res.in:8080/jspui/handle/10821/204, 2006.

Dempsey, J. T., Storey, J. W. V., and Phillips, A.: Auroral Contribution to Sky Brightness for Optical Astronomy on the Antarctic Plateau, Publications of the Astronomical Society of Australia, 22, 91–104, https://doi.org/10.1071/AS04036, 2005.

Deustua, S., Kent, S., and Smith, J. A.: Absolute Calibration of Astronomical Flux Standards, in: Planets, Stars and Stellar Systems, pp. 375–402, Springer Netherlands, Dordrecht, https://doi.org/10.1007/978-94-007-5618-2_8, 2013.

Dubovik, O., Smirnov, A., Holben, B. N., King, M. D., Kaufman, Y. J., Eck, T. F., and Slutsker, I.: Accuracy assessments of aerosol optical properties retrieved from Aerosol Robotic Network (AERONET) Sun and sky radiance measurements, Journal of Geophysical Research: Atmospheres, 105, 9791–9806, https://doi.org/10.1029/2000JD900040, http://doi.wiley.com/10.1029/2000JD900040, 2000.

Eyer, L. and Grenon, M.: Photometric Variability in the HR Diagram, in: Hipparcos - Venice '97, edited by Bonnet, R., Høg, E., Bernacca, P., Emiliani, L., Blaauw, A., Turon, C., Kovalevsky, J., Lindegren, L., Hassan, H., Bouffard, M., Strim, B., Heger, D., Perryman, M., and Woltjer, L., vol. 402, pp. 467–472, ui.adsabs.harvard.edu/abs/1997ESASP.402..467E/abstract, 1997.

Forgan, B. W.: General method for calibrating Sun photometers, Applied Optics, 33, 4841–4850, https://doi.org/10.1364/AO.33.004841, 1994.

Fried, D. L.: Limiting Resolution Looking Down Through Atmosphere, J. Opt. Soc. Am., 56, 1380–1384, https://doi.org/10.1364/JOSA.56.001380, 1966.

Galkin, V. D. and Arkharov, A. A.: Determination of Extra Atmospheric Monochromatic Stellar Magnitudes in the Region of Telluric Bands, Soviet Astronomy, 25, 361, http://adsabs.harvard.edu/abs/1981SvA....25..361G, 1981.

Galkin, V. D., Immler, F., Alekseeva, G. A., Berger, F. H., Leiterer, U., Naebert, T., Nikanorova, I. N., Novikov, V. V., Pakhomov, V. P., and Sal'nikov, I. B.: Analysis of the application of the optical method to the measurements of the water vapor content in the atmosphere - Part 1: Basic concepts of the measurement technique, Atmospheric Measurement Techniques, 4, 28, http://arxiv.org/abs/1010.5711, 2010a.

Galkin, V. D., Leiterer, U., Alekseeva, G. A., Novikov, V. V., and Pakhomov, V. P.: Accuracy of the Water Vapour Content Measurements in the Atmosphere Using Optical Methods, ArXiv e-prints, http://arxiv.org/abs/1010.3669, 2010b.

Gattinger, R. L. and Jones, A. V.: Quantitative Spectroscopy of the Aurora. II. The Spectrum of Medium Intensity Aurora Between 4500 and 8900 Å, Canadian Journal of Physics, 52, 2343–2356, https://doi.org/10.1139/p74-305, 1974.

Giles, D. M., Sinyuk, A., Sorokin, M. G., Schafer, J. S., Smirnov, A., Slutsker, I., Eck, T. F., Holben, B. N., Lewis, J. R., Campbell, J. R., Welton, E. J., Korkin, S. V., and Lyapustin, A. I.: Advancements in the Aerosol Robotic Network (AERONET) Version 3 database – automated near-real-time quality control algorithm with improved cloud screening for Sun photometer aerosol optical depth (AOD) measurements, Atmospheric Measurement Techniques, 12, 169–209, https://doi.org/10.5194/amt-12-169-2019, 2019.

Glindemann, A.: Relevant Parameters for Tip-Tilt Systems of Large Telescopes, Publications of the Astronomical Society of the Pacific, 109, 682, https://doi.org/10.1086/133932, 1997.

Golay, M.: Introduction to Astronomical Photometry, vol. 41 of *Astrophysics and Space Science Library*, D. Reidel Publishing Company, https://doi.org/10.1007/978-94-010-2169-2, 1974.

Gueymard, C. A.: Parameterized transmittance model for direct beam and circumsolar spectral irradiance, Solar Energy, 71, 325–346, https://doi.org/dx.doi.org/10.1016/S0038-092X(01)00054-8, 2001.

Halthore, R. N., Eck, T. F., Holben, B. N., and Markham, B. L.: Sun photometric measurements of atmospheric water vapor column abundance in the 940-nm band, Journal of Geophysical Research: Atmospheres, 102, 4343–4352, https://doi.org/10.1029/96JD03247, http://dx.doi.org/10.1029/96JD03247, 1997.

Hanuschik, R. W.: A flux-calibrated, high-resolution atlas of optical sky emission from UVES, Astronomy and Astrophysics, 407, 1157–1164, https://doi.org/10.1051/0004-6361:20030885, http://www.aanda.org/10.1051/0004-6361:20030885, 2003.

Hardie, R.: Photoelectric Reductions, in: Stars and Stellar Systems, edited by Hiltner, W., vol. 2, chap. Astronomic, p. 180, The University of Chicago Press, Chicago, http://www.worldcat.org/oclc/534975, 1962.

Herber, A., Thomason, L. W., Gernandt, H., Leiterer, U., Nagel, D., Schulz, K.-H., Kaptur, J., Albrecht, T., and Notholt, J.: Continuous day and night aerosol optical depth observations in the Arctic between 1991 and 1999, Journal of Geophysical Research: Atmospheres, 107, AAC 6–1–AAC 6–13, https://doi.org/10.1029/2001JD000536, 2002.

Hill, C., Yurchenko, S. N., and Tennyson, J.: Temperature-dependent molecular absorption cross sections for exoplanets and other atmospheres, Icarus, 226, 1673–1677, https://doi.org/https://doi.org/10.1016/j.icarus.2012.07.028, 2013.

Holben, B. N., Tanré, D., Smirnov, A., Eck, T. F., Slutsker, I., Abuhassan, N., Newcomb, W. W., Schafer, J. S., Chatenet, B., Lavenu, F., Kaufman, Y. J., Castle, J. V., Setzer, A., Markham, B., Clark, D., Frouin, R., Halthore, R., Karneli, A., O'Neill, N. T., Pietras, C., Pinker, R. T., Voss, K., and Zibordi, G.: An emerging ground-based aerosol climatology: Aerosol optical depth from AERONET, Journal of Geophysical Research: Atmospheres, 106, 12 067–12 097, https://doi.org/10.1029/2001JD900014, 2001.

Ivanescu, L., O'Neill, N. T., and Blanchet, J. P.: Spectrophotometric Catalog for Atmospheric Remote Sensing Through Starphotometry, in: American Geophysical Union, Fall Meeting 2017, abstract A23H-05, vol. 2017, pp. A23H–05, https://ui.adsabs.harvard.edu/#abs/2017AGUFM.A23H..05I, 2017.

Ivănescu, L.: Une application de la photométrie stellaire à l'observation de nuages optiquement minces à Eureka, NU, Master in science thesis, UQAM, www.archipel.uqam.ca/id/eprint/8417, 2015.

Ivănescu, L., Baibakov, K., O'Neill, N. T., Blanchet, J.-P., Blanchard, Y., Saha, A., Rietze, M., and Schulz, K.-H.: Challenges in operating an Arctic telescope, in: Proc. of SPIE, vol. 9145, pp. 21 – 49, https://doi.org/10.1117/12.2071000, 2014.

Johnson, H. and Morgan, W.: Fundamental stellar photometry for standards of spectral type on the revised system of the Yerkes spectral atlas, Astrophysical Journal, 117, 313, https://doi.org/10.1086/145697, 1953.

Jones, A. V. and Gattinger, R. L.: Quantitative Spectroscopy of the Aurora. I. The Spectrum of Bright Aurora between 7000 and 9000 Å at 7.5 Å Resolution, Canadian Journal of Physics, 50, 1833–1841, https://doi.org/10.1139/p72-249, http://www.nrcresearchpress.com/doi/10.1139/p72-249, 1972.

Jones, A. V. and Gattinger, R. L.: Quantitative Spectroscopy of the Aurora. III. The Spectrum of Medium Intensity Aurora Between 3100 Å and 4700 Å, Canadian Journal of Physics, 53, 1806–1813, https://doi.org/10.1139/p75-231, 1975.

Jones, A. V. and Gattinger, R. L.: Quantitative spectroscopy of the aurora. IV. The spectrum of medium intensity aurora between 8800 Å and 11 400 Å, Canadian Journal of Physics, 54, 2128–2133, https://doi.org/10.1139/p76-251, http://www.nrcresearchpress.com/doi/10.1139/p76-251, 1976.

Kaiser, M. and Access Team: ACCESS: Design, Calibration Strategy, and Status, in: The Science of Calibration, edited by Deustua, S., Allam, S., Tucker, D., and Smith, J., vol. 503 of *Astronomical Society of the Pacific Conference Series*, p. 221, http://aspbooks.org/custom/publications/paper/503-0221.html, 2016.

Kent, S., Kaiser, M. E., Deustua, S. E., Smith, J. A., Adelman, S., Allam, S., Baptista, B., Bohlin, R. C., Clem, J. L., Conley, A., Edelstein, J., Elias, J., Glass, I., Henden, A., Howell, S., Kimble, R. A., Kruk, J. W., Lampton, M., Magnier, E. A., McCandliss, S. R., Moos, W., Mostek, N., Mufson, S., Oswalt, T. D., Perlmutter, S., Prieto, C. A., Rauscher, B. J., Riess, A., Saha, A., Sullivan, M., Suntzeff, N., Tokunaga, A., Tucker, D., Wing, R., Woodgate, B., and Wright, E. L.: Photometric Calibrations for 21st Century Science, Astro2010: The Astronomy and Astrophysics Decadal Survey, p. 8, http://arxiv.org/abs/0903.2799, 2009.

Kharitonov, A., Tereshchenko, V., and Kniazeva, L.: A spectrophotometric catalog of stars, Izdatel'stvo Nauka, www.worldcat.org/oclc/904840420, 1978.

King, I.: Effective extinction values in wide-band photometry, The Astronomical Journal, 57, 253, https://doi.org/10.1086/106766, 1952.

Kippenhahn, R., Weigert, A., and Weiss, A.: Stellar Structure and Evolution, Springer Berlin Heidelberg, https://doi.org/10.1007/978-3-642-30304-3, www.worldcat.org/oclc/817913300, 2012.

Knyazeva, L. and Kharitonov, A.: Standard Stars for the Alma-Ata Catalog - Energy Distribution in the Spectrum of VEGA, Soviet Astronomy, 34, 626, 1990.

Krassovsky, V., Shefov, N., and Yarin, V.: Atlas of the airglow spectrum 3000–12400 Å, Planetary and Space Science, 9, 883–915, https://doi.org/10.1016/0032-0633(62)90008-9, 1962.

Kyrölä, E., Tamminen, J., Leppelmeier, G., Sofieva, V., Hassinen, S., Bertaux, J., Hauchecorne, A., Dalaudier, F., Cot, C., Korablev, O., Fanton d'Andon, O., Barrot, G., Mangin, A., Théodore, B., Guirlet, M., Etanchaud, F., Snoeij, P., Koopman, R., Saavedra, L., Fraisse, R., Fussen, D., and Vanhellemont, F.: GOMOS on Envisat: an overview, Advances in Space Research, 33, 1020–1028, https://doi.org/10.1016/S0273-1177(03)00590-8, 2004.

Le Borgne, J.-F., Bruzual, G., Pelló, R., Lançon, A., Rocca-Volmerange, B., Sanahuja, B., Schaerer, D., Soubiran, C., and Vílchez-Gómez, R.: STELIB: A library of stellar spectra at R=2000, Astronomy and Astrophysics, 402, 433–442, https://doi.org/10.1051/0004-6361:20030243, 2003.

Leiterer, U., Naebert, A., Naebert, T., and Alekseeva, G. A.: A new star photometer developed for spectral aerosol optical thickness measurements in Lindenberg, Contributions to atmospheric physics, 68, 133–141, http://www.worldcat.org/oclc/3416825, 1995.

Leiterer, U., Alekseeva, G. A., Galkin, V. D., Dier, D., Güldner, J., Naebert, A., Naebert, T., Novikov, V. V., Rentsch, H., and Sakunov, G.: Water vapor column content and optical depths measurements by a sun- and starphotometer, Contributions to atmospheric physics, 71, 401–420, http://www.worldcat.org/oclc/3416825, 1998.

Lindenmaier, R., Strong, K., Batchelor, R. L., Bernath, P. F., Chabrillat, S., Chipperfield, M. P., Daffer, W. H., Drummond, J. R., Feng, W., Jonsson, A. I., Kolonjari, F., Manney, G. L., McLinden, C., Menard, R., and Walker, K. A.: A study of the Arctic NOy budget above Eureka, Canada, J. Geophys. Res., 116, D23 302, https://doi.org/10.1029/2011JD016207, http://dx.doi.org/10.1029/2011JD016207, 2011.

Liou, K.-N. N.: An introduction to atmospheric radiation, Academic Press, 2nd edn., http://www.worldcat.org/oclc/156781712, 2002.

Marouani, H. and Dagenais, M. R.: Internal Clock Drift Estimation in Computer Clusters, Journal of Computer Systems, Networks, and Communications, 2008, 1–7, https://doi.org/10.1155/2008/583162, 2008.

Mitchell, R. M. and Forgan, B. W.: Aerosol Measurement in the Australian Outback: Intercomparison of Sun Photometers, Journal of Atmospheric and Oceanic Technology, 20, 54–66, https://doi.org/10.1175/1520-0426(2003)020<0054:AMITAO>2.0.CO;2, 2003.

Nijegorodov, N. and Luhanga, P. V.: Air mass : Analytical and empirical treatment; an improved formula for air mass, Renewable Energy, 7, 57–65, https://doi.org/10.1016/0960-1481(95)00111-5, 1996.

Nyassor, P. K., Buriti, R. A., Paulino, I., Medeiros, A. F., Takahashi, H., Wrasse, C. M., and Gobbi, D.: Determination of gravity wave parameters in the airglow combining photometer and imager data, Annales Geophysicae, 36, 705–715, https://doi.org/10.5194/angeo-36-705-2018, 2018.

Ochsenbein, F., Bauer, P., and Marcout, J.: The VizieR database of astronomical catalogues, Astronomy and Astrophysics Supplement Series, 143, 23–32, https://doi.org/10.1051/aas:2000169, 2000.

Oke, J. and Schild, R. E.: The absolute spectral energy distribution of Alpha Lyrae, Astrophysical Journal, 161, 1015, https://doi.org/10.1086/150603, 1970.

O'Neill, N. T., Dubovik, O., and Eck, T. F.: Modified Ångström exponent for the characterization of submicrometer aerosols, Applied Optics, 40, 2368–2375, https://doi.org/10.1364/AO.40.002368, 2001a.

O'Neill, N. T., Eck, T., Holben, B. N., Smirnov, A., Dubovik, O., and Royer, A.: Bimodal size distribution influences on the variation of Angstrom derivatives in spectral and optical depth space, Journal of Geophysical Research: Atmospheres, 106, 9787–9806, https://doi.org/10.1029/2000JD900245, 2001b.

Orphal, J. and Chance, K.: Ultraviolet and visible absorption cross-sections for HITRAN, Journal of Quantitative Spectroscopy and Radiative Transfer, 82, 491–504, https://doi.org/10.1016/S0022-4073(03)00173-0, https://www.sciencedirect.com/science/article/pii/S0022407303001730, 2003.

Orphal, J., Fellows, C. E., and Flaud, P.-M.: The visible absorption spectrum of NO 3 measured by high-resolution Fourier transform spectroscopy, Journal of Geophysical Research: Atmospheres, 108, n/a–n/a, https://doi.org/10.1029/2002JD002489, http://doi.wiley.com/10.1029/2002JD002489, 2003.

Osborn, J.: Profiling the turbulent atmosphere and novel correction techniques for imaging and photometry in astronomy, Ph.D. thesis, Durham University, http://etheses.dur.ac.uk/513/, 2010.

Owens, J. C.: Optical Refractive Index of Air: Dependence on Pressure, Temperature and Composition, Applied Optics, 6, 51, https://doi.org/10.1364/AO.6.000051, 1967.

Paraskeva, V., Norton, M., Hadjipanayi, M., and Georghiou, G. E.: Calibration of Spectroradiometers for Outdoor Direct Solar Spectral Irradiance Measurements, 28th European Photovoltaic Solar Energy Conference and Exhibition, pp. 3466–3471, https://doi.org/10.4229/28THEUPVSEC2013-4AV.6.35, 2013.

Pérez-Ramírez, D., Aceituno, J., Ruiz, B., Olmo, F. J., and Alados-Arboledas, L.: Development and calibration of a star photometer to measure the aerosol optical depth: Smoke observations at a high mountain site, Atmospheric Environment, 42, 2733–2738, https://doi.org/10.1016/j.atmosenv.2007.06.009, 2008a.

Pérez-Ramírez, D., Ruiz, B., Aceituno, J., Olmo, F. J., and Alados-Arboledas, L.: Application of Sun/star photometry to derive the aerosol optical depth, International Journal of Remote Sensing, 29, 5113–5132, https://doi.org/10.1080/01431160802036425, 2008b.

Pérez-Ramírez, D., Lyamani, H., Olmo, F. J., and Alados-Arboledas, L.: Improvements in star photometry for aerosol characterizations, Journal of Aerosol Science, 42, 737–745, https://doi.org/10.1016/j.jaerosci.2011.06.010, 2011.

Pickles, A. J.: A Stellar Spectral Flux Library: 1150–25000 Å, Publications of the Astronomical Society of the Pacific, 110, 863–878, https://doi.org/10.1086/316197, 1998.

Qie, L., Li, Z., Goloub, P., Li, L., Li, D., Li, K., Zhang, Y., and Xu, H.: Retrieval of the aerosol asymmetry factor from Sun–sky radiometer measurements: application to almucantar geometry and accuracy assessment, Applied Optics, 56, 9932, https://doi.org/10.1364/ao.56.009932, https://www.osapublishing.org/abstract.cfm?URI=ao-56-36-9932, 2017.

Racine, R.: The Telescope Point Spread Function, Publications of the Astronomical Society of the Pacific, 108, 699, https://doi.org/10.1086/133788, 1996.

Rapp-Arrarás, Í. and Domingo-Santos, J. M.: Functional forms for approximating the relative optical air mass, Journal of Geophysical Research: Atmospheres, 116, n/a–n/a, https://doi.org/10.1029/2011JD016706, http://doi.wiley.com/10.1029/2011JD016706, 2011.

Rauch, T., Werner, K., Bohlin, R. C., and Kruk, J. W.: The virtual observatory service TheoSSA: Establishing a database of synthetic stellar flux standards, Astronomy and Astrophysics, 560, A106, https://doi.org/10.1051/0004-6361/201322336, 2013.

Robertson, J. G.: Detector Sampling of Optical/IR Spectra: How Many Pixels per FWHM?, Publications of the Astronomical Society of Australia, 34, e035, https://doi.org/10.1017/pasa.2017.29, 2017.

Roddier, F.: The Effects of Atmospheric Turbulence in Optical Astronomy, in: Progress in Optics, chap. V, pp. 281–376, Elsevier, https://doi.org/10.1016/S0079-6638(08)70204-X, 1981.

Roscoe, H. K., Jones, R. L., Freshwater, R. A., Fish, D., Wolfenden, R., Harries, J. E., and Oldham, D. J.: A star-pointing UV-visible spectrometer for remote sensing of the stratosphere, in: Proceedings of SPIE, Optical Methods in Atmospheric Chemistry, vol. 1715, pp. 374–380, https://doi.org/10.1117/12.140226, 1993.

Rothman, L., Gordon, I., Barbe, A., Benner, D., Bernath, P., Birk, M., Boudon, V., Brown, L., Campargue, A., Champion, J.-P., Chance, K., Coudert, L., Dana, V., Devi, V., Fally, S., Flaud, J.-M., Gamache, R., Goldman, A., Jacquemart, D., Kleiner, I., Lacome, N., Lafferty, W., Mandin, J.-Y., Massie, S., Mikhailenko, S., Miller, C., Moazzen-Ahmadi, N., Naumenko, O., Nikitin, A., Orphal, J., Perevalov, V., Perrin, A., Predoi-Cross, A., Rinsland, C., Rotger, M., Šimečková, M., Smith, M., Sung, K., Tashkun, S., Tennyson, J., Toth, R., Vandaele, A., and Vander Auwera, J.: The HITRAN 2008 molecular spectroscopic database, Journal of Quantitative Spectroscopy and Radiative Transfer, 110, 533–572, https://doi.org/10.1016/j.jqsrt.2009.02.013, http://www.sciencedirect.com/science/article/pii/S0022407309000727, 2009.

Rufener, F.: Technique et réduction des mesures dans un nouveau système de photométrie stellaire, Archives des Sciences, Genève, 16, 30, http://www.worldcat.org/oclc/491819702, 1963.

Rufener, F.: Technique et réduction des mesures dans un nouveau système de photométrie stellaire, Publications de l'Observatoire de Genève, Série A: Astronomie, chronométrie, géophysique, 66, 413–464, http://www.worldcat.org/oclc/491819702, 1964.

Rufener, F.: The evolution of atmospheric extinction at La Silla, Astronomy and Astrophysics, 165, 275–286, http://adsabs.harvard.edu/abs/1986A&A...165..275R, 1986.

Shannon, C. E.: A Mathematical Theory of Communication, Bell System Technical Journal, 27, 379–423, https://doi.org/10.1002/j.1538-7305.1948.tb01338.x, 1948.

Shaw, G. E.: Error analysis of multi-wavelength sun photometry, pure and applied geophysics, 114, 1–14, https://doi.org/10.1007/BF00875487, 1976.

Shiobara, M., Asano, S., Shiobara, M., and Asano, S.: Estimation of Cirrus Optical Thickness from Sun Photometer Measurements, Journal of Applied Meteorology, 33, 672–681, https://doi.org/10.1175/1520-0450(1994)033<0672:EOCOTF>2.0.CO;2, 1994.

Silva, D. R. and Cornell, M. E.: A new library of stellar optical spectra, The Astrophysical Journal Supplement Series, 81, 865, https://doi.org/10.1086/191706, 1992.

Sivanandam, S., Graham, J. R., Abraham, R., Tekatch, A., Steinbring, E., Ngan, W., Welch, D. L., and Law, N. M.: Characterizing near-infrared sky brightness in the Canadian high arctic, in: Proceedings of SPIE, vol. 8446, pp. 844 612–844 643, http://dx.doi.org/10.1117/12.926251, 2012.

Steinbring, E., Millar-Blanchaer, M., Ngan, W., Murowinski, R., Leckie, B., and Carlberg, R.: Preliminary DIMM and MASS Nighttime Seeing Measurements at PEARL in the Canadian High Arctic, Publications of the Astronomical Society of the Pacific, 125, 866–877, https://doi.org/10.1086/671482, 2013.

Stone, R. C.: An Accurate Method for Computing Atmospheric Refraction, Publications of the Astronomical Society of the Pacific, 108, 1051, https://doi.org/10.1086/133831, http://iopscience.iop.org/article/10.1086/133831, 1996.

Tomasi, C. and Petkov, B. H.: Calculations of relative optical air masses for various aerosol types and minor gases in Arctic and Antarctic atmospheres, Journal of Geophysical Research: Atmospheres, 119, 1363–1385, https://doi.org/10.1002/2013JD020600, 2014.

Tomasi, C., Vitale, V., and De Santis, L. V.: Relative optical mass functions for air, water vapour, ozone and nitrogen dioxide in atmospheric models presenting different latitudinal and seasonal conditions, Meteorology and Atmospheric Physics, 65, 11–30, https://doi.org/10.1007/BF01030266, 1998.

Tyler, G. A.: Bandwidth considerations for tracking through turbulence, Journal of the Optical Society of America A, 11, 358–367, https://doi.org/10.1364/JOSAA.11.000358, 1994.

Vestine, E. H.: The Geographic Incidence of Aurora and Magnetic Disturbance, Northern Hemisphere, Journal of Geophysical Research, 49, 77, https://doi.org/10.1029/TE049i002p00077, http://doi.wiley.com/10.1029/TE049i002p00077, 1944.

Voigt, S., Orphal, J., Bogumil, K., and Burrows, J.: The temperature dependence (203–293 K) of the absorption cross sections of O3 in the 230–850 nm region measured by Fourier-transform spectroscopy, Journal of Photochemistry and Photobiology A: Chemistry, 143, 1–9, https://doi.org/10.1016/S1010-6030(01)00480-4, http://www.sciencedirect.com/science/article/pii/S1010603001004804, 2001.

Volz, F. E.: Depth and Shape of the 0.94-μm Water Vapor Absorption Band for Clear and Cloudy Skies, Applied Optics, 8, 2261, https://doi.org/10.1364/AO.8.002261, 1969.

Wagner, T., von Friedeburg, C., Wenig, M., Otten, C., and Platt, U.: UV-visible observations of atmospheric O4 absorptions using direct moonlight and zenith-scattered sunlight for clear-sky and cloudy sky conditions, Journal of Geophysical Research, 107, 4424, https://doi.org/10.1029/2001JD001026, 2002.

Wenger, M., Ochsenbein, F., Egret, D., Dubois, P., Bonnarel, F., Borde, S., Genova, F., Jasniewicz, G., Laloë, S., Lesteven, S., and Monier, R.: The SIMBAD astronomical database, Astronomy and Astrophysics Supplement Series, 143, 9–22, https://doi.org/10.1051/aas:2000332, http://aas.aanda.org/10.1051/aas:2000332, 2000.

Witze, A.: Earth's magnetic field is acting up and geologists don't know why, Nature, 565, 143–144, https://doi.org/10.1038/d41586-019-00007-1, 2019.

WMO: WMO/GAW Aerosol Measurement Procedures, Guidelines and Recommendations, Tech. Rep. WMO- No. 1177; GAW Report- No. 227, https://library.wmo.int/doc_num.php?explnum_id=3073, 2016.

Young, A. T.: Observational Technique and Data Reduction, in: Methods in Experimental Physics, vol. 12, chap. 3, pp. 123–192, Elsevier, https://doi.org/10.1016/S0076-695X(08)60495-0, 1974.

Young, A. T.: High-Precision Photometry, in: Automated Telescopes for Photometry and Imaging, vol. 28, p. 73, ASP Conference Series, https://ui.adsabs.harvard.edu/abs/1992ASPC...28...73Y, 1992.

Young, A. T.: Air mass and refraction, Applied Optics, 33, 1108, https://doi.org/10.1364/AO.33.001108, 1994.

Young, A. T. and Irvine, W. M.: Multicolor photoelectric photometry of the brighter planets. I. Program and Procedure, Astronomical Journal, 72, 945, https://doi.org/10.1086/110366, 1967.

Zhao, G., Zhao, Y.-H., Chu, Y.-Q., Jing, Y.-P., and Deng, L.-C.: LAMOST spectral survey — An overview, Research in Astronomy and Astrophysics, 12, 723–734, http://www.raa-journal.org/raa/index.php/raa/article/view/1171, 2012.

Zhao, G., Zhao, C., Kuang, Y., Bian, Y., Tao, J., Shen, C., and Yu, Y.: Calculating the aerosol asymmetry factor based on measurements from the humidified nephelometer system, Atmospheric Chemistry and Physics, 18, 9049–9060, https://doi.org/10.5194/acp-18-9049-2018, https://www.atmos-chem-phys.net/18/9049/2018/, 2018.

Zimmer, P., McGraw, J., Zirzow, D., Cramer, C., Lykke, K., and Woodward IV, J.: A Path to NIST Calibrated Stars over the Dome of the Sky, in: The Science of Calibration, edited by Deustua, S., Allam, S., Tucker, D., and Smith, J., vol. 503 of *Astronomical Society of the Pacific Conference Series*, p. 145, http://aspbooks.org/custom/publications/paper/503-0145.html, 2016.

Chapter 3

Multi-star calibration in starphotometry

Foreword

Letter to be submitted to Atmospheric Environment Journal of Elsevier!

Multi-star calibration in starphotometry

Liviu Ivănescu[a,*], Norman T. O'Neill[a] and Jean-Pierre Blanchet[b]

[a]Centre d'applications et de recherches en télédétection (CARTEL), Université de Sherbrooke, Sherbrooke, QC, Canada
[b]Department of Earth and Atmospheric Sciences, Université du Québec à Montréal (UQÀM)

ARTICLE INFO

Keywords:
starphotometry
calibration
Langley
Arctic
Eureka

ABSTRACT

In this study we explored the improvement of starphotometry accuracy by using a multi-star calibration, as opposed to the more traditional one-star (sunphotometry-type) approach. The aim is to obtain 0.01 repeatability accuracy, even at our operational sea-level Arctic facility in Eureka, NU, Canada. We show that such a calibration can be completed in about 2.5 h. By limiting the airmass range to 1–5 (which can only be achieved using a multi-star approach) and by taking advantage of, what we call, the reverse calibration method, the multi-star calibration repeatability approaches the 0.01 target.

1. Introduction

A comprehensive analysis of the starphotometry errors and their calibration effects was first detailed in Young [14]. Calibration strategies for retrieving accurate photometric observations in variable optical depth conditions were proposed by Rufener [12, 13]. Curiously, those fundamental studies went mostly unnoticed in the starphotometry literature dealing with aerosol remote sensing. Those studies, were updated and complemented using measurements from a High Arctic, sea-level observatory at Eureka, NU, Canada (Ivănescu et al. [3, 4]).

The singular advantages of performing starphotometer calibrations at a high altitude mountainous observatory were noted in those papers. However, the remoteness of the Eureka site and the significant infrastructure requirements of the starphotometer facility (instrument, telescope, mount and dome), render a temporary calibration campaign at such a site a very difficult task. It was therefore decided to perform on-site calibrations, despite the relatively large optical depth variability that can occur in the atmospheric boundary layer of a sea-level Arctic location (c.f. O'Neill et al. [8], Baibakov et al. [1], for example).

Star-dependent (one-star) calibration is the current standard procedure in starphotometry [9, 10]. However, in the high Arctic, stars do not go through large elevation (airmass) changes (in the extreme case of a site at the pole, there are no elevation changes) and, at best, one can only hope for moderate elevation changes of few low stars. This severely hampers the availability of acceptable calibration stars. Our goal in this communication is to demonstrate that an optical depth accuracy of 0.01 due to calibration errors can be achieved by performing the type of instrument-dependent, star-independent calibration referred to in Ivănescu et al. [4].

*Corresponding author
Liviu.Ivanescu@usherbrooke.ca (L. Ivănescu)
ORCID(s): 0000-0001-5658-0647 (L. Ivănescu)

2. Calibration methodology

2.1. Langley calibration

The starphotometer retrieval algorithm is based on extraterrestrial and atmospherically attenuated magnitudes of non variable bright stars, denoted by M_0 (usually provided by a catalog) and M, respectively (see Ivănescu et al. [4] for the nomenclature details). Their corresponding (instrument) signals, expressed as magnitudes, are S_0 and S, respectively. The star-independent conversion factor between the catalog and instrument magnitudes is (ibid)

$$C = M - S \tag{1}$$

$$C = M_0 - S_0 \tag{2}$$

This factor accounts for the optical and electronic throughput of the starphotometer as well as the photometric system transformation between the instrument and the extraterrestrial catalog. The Beer-Bouguer-Lambert atmospheric attenuation law in terms of magnitudes is

$$M = M_0 + (m/0.921)\tau \tag{3}$$

where m is the observed airmass and τ is the total optical depth. Inserting equation (1) yields

$$M_0 - S = -\tau x + C \tag{4}$$

where $x = m/0.921$. This expression can be used to retrieve C from a linear regression of S versus x, if M_0 is known and τ is approximately constant. Such a procedure is referred to as the Langley calibration technique, or Langley plot. In the absence of an accurate M_0 spectrum, equation (2) can be used to transform equation (4) to

$$S = \tau x + S_0 \tag{5}$$

and a catalog is no longer required. This linear regression enables the retrieval of S_0 instead of C, and represents a star-dependent calibration that has to be performed on every star. With respect to equation (5), the introduction of the instrument-dependent parameter C in equation (4) represents the transfer of the star-specific component M_0 of S_0, into the ordinate values. This led to a star-independent linear regression, effectively opening the way for a multi-star calibration.

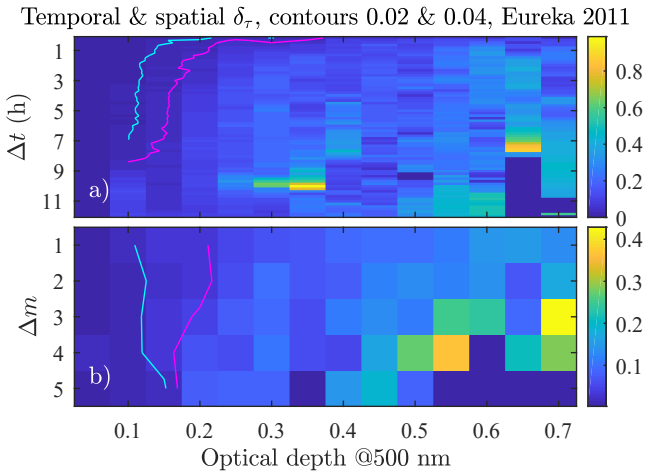

Figure 1: a) Optical depth variability as a function of the observing time delay and optical depth (color code on the right). b) Optical depth variability as a function of the airmass difference and optical depth. Data acquired from Eureka during January and February 2011.

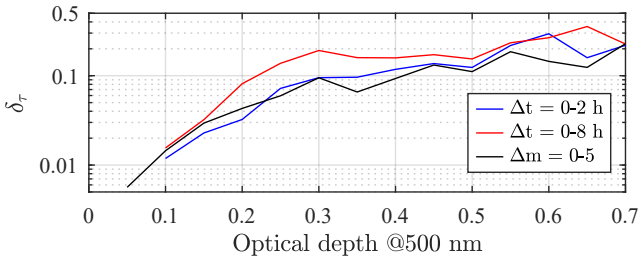

Figure 2: Optical depth variability as a function of observing optical depth.

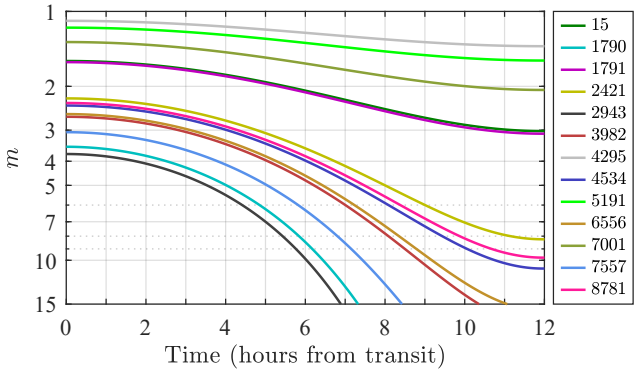

Figure 3: Airmass versus time past the transit for all bright stars observable at Eureka (identified by their HR index in the Bright Star catalog). The transit of a given star is when it crosses the local meridian (minimum airmass). High stars never go below airmass 4.

2.2. Reversed calibration

Rufener [12] and Young and Irvine [15], proposed to partially compensate for the heteroscedasticity errors (observational errors that increase with airmass) by dividing measurements by the airmass. Dividing our star-independent calibration equation (4) by x, leads to C and τ swapping their statuses as slope and intercept, respectively:

$$(M_0 - S)\frac{1}{x} = C\frac{1}{x} - \tau \tag{6}$$

We call this approach the "Reversed" Langley calibration. It was applied in the sunphotometry analyses of Mitchell and Forgan [5], and subsequently in the one-star calibration studies of Pérez-Ramírez et al. [10] and Oh [7].

3. Observing conditions

The assumption of constant τ in time (t) and observational direction (x) may be problematic over long observation periods and over large airmass changes. It is accordingly a useful exercise to assess the average time period and airmass range over which a degree of τ constancy is maintained. Figure 1 shows the particulate optical depth variability (in term of median absolute variation) as a function of the optical depth on the abscissa axis, for various bins of (a) time delay and (b) airmass difference on the ordinate axis. The magenta and cyan curves in Figure 1 show the 0.02 and 0.04 level of optical depth variation, respectively, delimiting the corresponding zones of stability. This confirms the expected low optical depth variability in clear sky conditions. In addition, it indicates that this happens at $\tau < 0.15$, providing up to 7–8 h of data for which $\delta\tau < 0.02$.

The variability of τ across typical calibration ranges (extracted from the data of Figure 1) is shown in Figure 2 for three situations: a 2 hour fast calibration, an 8 hour night-long calibration and a calibration extending across an airmass range of 1 to 5. We note their similar $\delta\tau$ behaviour and that, on average, there is not much distinction on a clear night (optical depth $\lesssim 0.1$) between the 2 and 8 h cases. However, if the $\delta\tau$ target variability is < 0.01 then, by extrapolating the curves of Figure 2 (not shown), one expects that an acceptable calibration measurement period must be 2 h or less.

Most stars are circumpolar in the Arctic (i.e. they never set). Their airmass range should accordingly be limited. Figure 3 shows the airmass variation as a function of time past the transit for each of the 13 bright stars observable at Eureka. This shows a very well defined segregation between the high stars (m is always < 3.1) and the low stars (m is always > 2.2, with a maximum that is always > 8.2). A large airmass range is accordingly only available for about 2/3 of the bright Eureka stars (mostly the low stars). Ivănescu et al. [4] showed that, if $m > 5$, some star vignetting (i.e. flux loss outside the Field of View - FOV) may affect the optical throughput of the Eureka system. Figure 3 shows that the constraints of $m = 1$–5 in less than 2 h can never be fulfilled by using a single star. A multi-star calibration would appear to be a natural potential solution.

4. Calibration errors

4.1. Accuracy error

The calibration accuracy error is the (rearranged) differential of equation (4)

$$\delta_C = (\delta_x \tau + x\delta_\tau) - \delta_S + \delta_{M_0} \tag{7}$$

The error $(\delta_x \tau + x\delta_\tau)$ accounts, respectively, for the sky transparency and stability during the calibration. It underscores the rationale for performing calibrations at a high altitude site (where τ, δ_τ and $\delta_x \tau$ are smaller) and the advantage of keeping x small in order to minimize the $x\delta_\tau$ contribution to δ_C. The δ_S error component accounts for any throughput degradation (optics degradation, misalignment error, star spot vignetting, etc.) during the calibration. The δ_{M_0} component accounts for the bias of the bright star catalog (i.e. the average of all catalog errors associated with each star). However, since δ_{M_0} is constant, the optical depth accuracy will not be affected as long as one consistently employs the same catalog (i.e. the error is compensated by calibration).

4.2. Precision error

Non-systematic, zero-mean, random errors account for precision errors. In the Langley plot form of equation (4), the ordinate is $M_0 - S$ and the abscissa is x. The standard deviation of the ordinate, given that errors in S and M_0 are clearly uncorrelated, is

$$\sigma_{M_0 - S} = \sqrt{\sigma_S^2 + \sigma_{M_0}^2} \tag{8}$$

where σ_S is the random observation error, while σ_{M_0} corresponds to the random M_0 errors of each star about the catalog bias (a parameter that only has relevance in the case of a multi-star calibration). The corresponding standard error of the mean $\overline{M_0 - S}$ is then

$$\sigma_{\overline{M_0 - S}} = \sqrt{\frac{\sigma_S^2}{n} + \frac{\sigma_{M_0}^2}{N}} \tag{9}$$

with n being the number of observations, N the number of stars employed in the calibration and the overscore denoting the average. When n and N are large (i.e. > 10), the regression slope and intercept errors are (see, for example, Montgomery and Runger [6])

$$\sigma_\tau = \frac{\sigma_{\overline{M_0 - S}}}{\sigma_x}, \qquad \sigma_C = \sigma_\tau \bar{x} \tag{10}$$

The Reverse calibration takes advantage of the fact that the slope and intercept behave differently with respect to observation errors

$$\sigma_C = \frac{\sigma_{\overline{(M_0 - S)/x}}}{\sigma_{1/x}}, \qquad \sigma_\tau = \sigma_C \overline{1/x} \tag{11}$$

with

$$\sigma_{\overline{(M_0 - S)/x}} = \sqrt{\frac{\sigma_{S/x}^2}{n} + \frac{\sigma_{M_0/x}^2}{N}} \tag{12}$$

Assuming σ_S heteroscedasticity in x, $\sigma_{S/x}$ is reduced to a constant with respect to x, while $\sigma_{M_0/x}$ is greatly reduced since M_0 and x are not correlated. σ_C is not only reduced by large values of n and N, but also by large values $1/x$ range. The latter can be principally increased by employing stars with moderately low x values (at $x > 5$ one gets only small range extensions). In any case, going beyond an airmass constraint may add accuracy errors associated with throughput degradation due to star vignetting. The only way to use this optimum x range of 1–5 is by performing the multi-star calibration using high and low stars near their transit position. One should note that, while n can be increased indefinitely, N is limited by star availability and may become the limiting factor in calibration repeatability.

5. Multi-star calibration

This type of calibration exploits a unique and major advantage of starphotometry over moonphotometry and sunphotometry: the capability of employing multiple and independent, attenuated light sources in a relatively short period of time. In comparison to a star-independent, single-star calibration, the multi-star approach enables consistent calibration for several stars at once. One-star and multi-star Langley calibrations derived for high spectral resolution measurements (i.e. 0.7 nm resolution and about 8.5 nm bandwidth) are shown in Figure 4. These measurements, acquired at Eureka on 2019/12/07 and 2020/01/10, are the averages of five 6 s exposures. In this case data can be acquired up to $x = 10$ (for a one-star calibration) and up to $x = 8$ (for a multi-star calibration) in order to verify any non-linear effects due to vignetting at $x > 5$ and to allow the use of all of our star data set. The one-star calibration (red colored little dots and pink fit) is based on the low Procyon star (2943). It undergoes the most rapid airmass variation (c.f. Figure 3) and, due to its cold temperature, exhibits higher near infrared brightness temperature (a generally low signal to noise spectral region for most stars). Figure 5 shows the corresponding one-star and multi-star Reverse calibrations. The apparently superior linear fit is mainly an effect of error heteroscedasticity removal associated with the division by x.

The resulting τ value representing, respectively, the slope and intercept of the linear regression in Langley and Reversed calibration space for the one-star and multi-star approaches, are shown in Figure 6a (specifically the particulate and absorption components of τ, after subtraction of the molecular scattering optical depth). Their associated precision errors are shown in Figure 6b. While the multi-star error is generally much smaller than that of the one-star, there is no obvious improvement in τ precision when applying the Reverse calibration. We note that the optical depths in Figure 6a are consistently larger in the multi-star case. The relatively narrow one-star airmass range, limited to large x values which are more prone to systematic errors, may well explain the differences in slope and is an inevitable consequence of having to rely on low stars for one-star Langley calibrations.

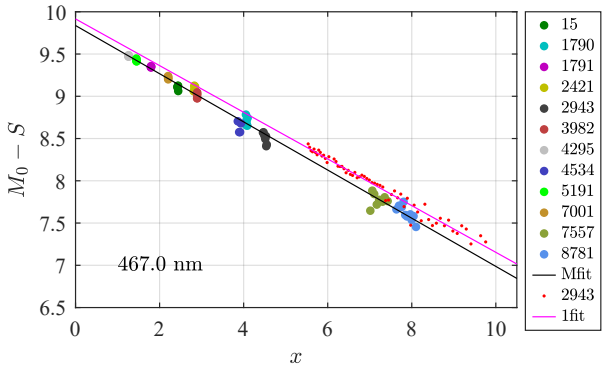

Figure 4: One-star and multi-star Langley calibrations (both lasted about 2.5 h). The one-star calibration is based on HR 2943 (small red dots), having the solid pink regression line (1fit). The stars (other than HR 2943) that were employed for the multi-star calibration are also labelled with their HR IDs, while their linear fit is a solid black line (Mfit).

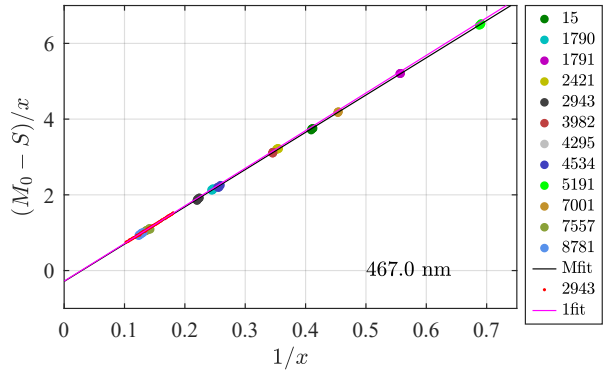

Figure 5: One-star and multi-star Reversed calibrations. Same legend as Figure 4

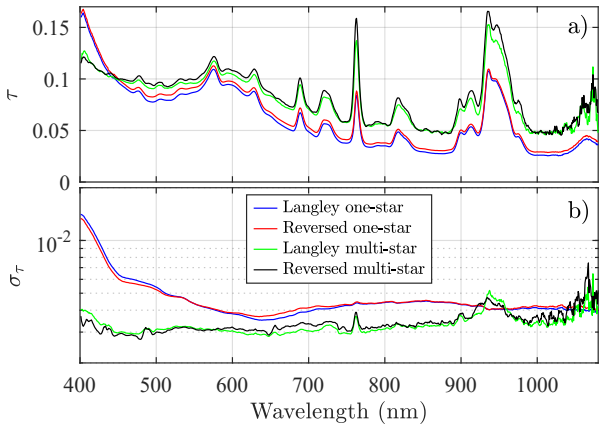

Figure 6: a) Optical depth retrieval (less the molecular optical depth) using the one-star and multi-star methods for Langley and Reversed calibrations. b) Optical depth precision errors using the σ_τ expressions of equations (10) and (11).

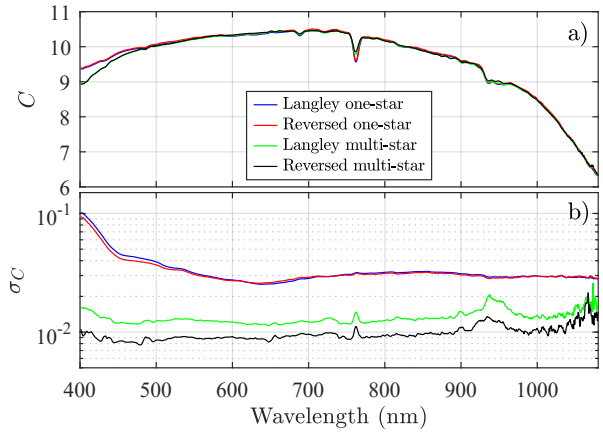

Figure 7: a) Calibration parameter retrieval from the one-star and multi-star methods, for Langley and Reversed calibrations. b) Calibration parameter precision errors computed using the σ_C expressions of equations (10) and (11).

The derived C values representing, respectively, the slope and intercept of the Langley and Reversed calibration regressions (for one-star and multi-star approaches), are shown in Figure 7a. The associated precision errors are shown in Figure 7b. The multi-star error is significantly smaller than the one-star error and shows about a factor of 2 systematic improvement for the Reverse calibration. In contrast, the one-star calibration, given its limitation at high x, only shows a limited improvement by applying Reverse calibration.

6. Repeatability

The cumulative effect of the accuracy and precision errors can be assessed through repeatability experiments. This is shown in Figure 8 as the standard deviation of 3 calibration parameters (C) retrieved in significantly different sky conditions. The one-star errors are prohibitively large, much larger than their precision estimation and thus dominated by accuracy errors. The sky stability during a given Langley calibration can be confirmed by retrieving τ from equation (4) using the retrieved C for that same calibration. However, even if δ_τ is limited to values less than 0.01 (the best conditions of Figure 2), $x\delta_\tau$ may become significant at the large x specific to the one-star calibration. In addition, accuracy errors may also come from δ_S, most probably due to star spot vignetting at large x. The multi-star errors are, on the other hand, generally near the 0.01 error target. However, the calibration errors are larger in the near infrared-end part of the spectrum (typically characterized by noisy signals due to generally lower star brightness), particularly in the region of strong water vapor absorption bands (due to their non-linear dependency on airmass, as shown in Galkin et al. [2]) and at the blue-end of the spectrum. One reason for the latter may again be related to the throughput degradation effects of star spot vignetting. Since the star spot size varies as $\lambda^{-1/5}$ [11], it will be 20% larger in the blue (400 nm) than at 1000 nm. Another reason for the higher errors is that the total optical depth (including that of the molecular scatter-

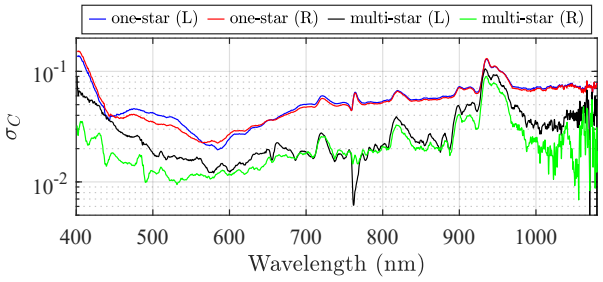

Figure 8: Repeatability calculations based on measurements performed on 2019/12/07, 2020/01/05 and 2020/01/16 at Eureka, for one-star Langley (blue, L) and Reversed (red, R) calibration parameter retrieval. A similar exercised was carried out on 2018/03/10, 2019/12/07 and 2020/01/10 at Eureka, for multi-star Langley (black, L) and Reversed (green, R) calibration parameter retrieval.

ing) is also higher in the blue. It is interesting to note the resemblance between the spectral shape of this repeatability error (particularly the multi-star version) and the bias found in our extraterrestrial star magnitude catalog (see Figure 4 of Ivănescu et al. [4]). This suggests that the calibration repeatability is limited by the catalog errors. As emphasised in section 4.2, the Reverse calibration reduces σ_{M_0} influence, which is confirmed by its lower repeatability errors in Figure 8, particularly in blue and infra-red. The only way to improve this further is to improve the catalog accuracy.

7. Conclusions

In this study we compared the performances of the one-star and multi-star approaches to retrieve a star-independent calibration parameter. In limiting the airmass range to 1–5 we found that there was no unique Eureka star that covered this range. The solution to this intrinsic shortcoming of a high Arctic site is to use a multi-star approach. It has the fundamental advantage of limiting the calibration period and thus limiting the chances of sky variability. This approach is, by its very nature, a star-independent calibration that enables the retrieval of a star independent calibration parameter.

The Reversed calibration acts to reduce calibration errors with increasing airmass, and those related to the extraterrestrial magnitude catalog accuracy. Our results showed that it had a moderate effect on reducing the calibration parameter error to values near or below 0.01. In order to fulfill our calibration repeatability requirement, a more accurate catalog is required. That will open up the possibility of obtaining accurate on-site calibrations, even at a sea-level site such as Eureka. However, in order to confirm the benefits of the calibration approaches reported here, it would be advisable to validate them at a high elevation observatory.

Acknowledgements

This work was supported logistically and financially by CANDAC (the Canadian Network for the Detection of Atmospheric Change) through PAHA (Probing the Atmosphere of the High Arctic) funding, by the NSERC CREATE Training Program in Arctic Atmospheric Science, by the FAST programs of the CSA (Canadian Space Agency) and by NETCARE (Network on Climate and Aerosols: Addressing Key Uncertainties in Remote Canadian Environments). We gratefully acknowledge the support of the operations staff at Eureka for numerous troubleshooting interventions

References

[1] Baibakov, K., O'Neill, N.T., Ivănescu, L., Duck, T.J., Perro, C., Herber, A., Schulz, K.H., Schrems, O., 2015. Synchronous starphotometry and lidar measurements at Eureka in High Canadian Arctic. Atmos. Meas. Tech. Discuss. 8, 2013–2065. doi:10.5194/amtd-8-2013-2015.

[2] Galkin, V.D., Leiterer, U., Alekseeva, G.A., Novikov, V.V., Pakhomov, V.P., 2010. Accuracy of the Water Vapour Content Measurements in the Atmosphere Using Optical Methods. ArXiv e-prints URL: http://arxiv.org/abs/1010.3669, arXiv:1010.3669.

[3] Ivănescu, L., Baibakov, K., O'Neill, N.T., Blanchet, J.P., Blanchard, Y., Saha, A., Rietze, M., Schulz, K.H., 2014. Challenges in operating an Arctic telescope, in: Proc. of SPIE, pp. 21 – 49. doi:10.1117/12.2071000.

[4] Ivănescu, L., O'Neill, N.T., Blanchet, J.P., 2020. Accuracy in starphotometry. Atmos. Meas. Tech. Discuss. in work.

[5] Mitchell, R.M., Forgan, B.W., 2003. Aerosol Measurement in the Australian Outback: Intercomparison of Sun Photometers. Journal of Atmospheric and Oceanic Technology 20, 54–66. doi:10.1175/1520-0426(2003)020<0054:AMITAO>2.0.CO;2.

[6] Montgomery, D.C., Runger, G.C., 2011. Applied Statistics and Probability for Engineers. 5 ed., John Wiley and Sons, Inc. URL: http://www.worldcat.org/oclc/28632932.

[7] Oh, Y.L., 2015. Retrieval of Nighttime Aerosol Optical Thickness from Star Photometry. Atmosphere 25, 521–528. doi:10.14191/Atmos.2015.25.3.521.

[8] O'Neill, N.T., Baibakov, K., Hesaraki, S., Ivănescu, L., Martin, R.V., Perro, C., Chaubey, J.P., Herber, A., Duck, T.J., 2016. Temporal and spectral cloud screening of polar winter aerosol optical depth (AOD): impact of homogeneous and inhomogeneous clouds and crystal layers on climatological-scale AODs. Atmospheric Chemistry and Physics 16, 12753–12765. doi:10.5194/acp-16-12753-2016.

[9] Pérez-Ramírez, D., Aceituno, J., Ruiz, B., Olmo, F.J., Alados-Arboledas, L., 2008. Development and calibration of a star photometer to measure the aerosol optical depth: Smoke observations at a high mountain site. Atmospheric Environment 42, 2733–2738. doi:10.1016/j.atmosenv.2007.06.009.

[10] Pérez-Ramírez, D., Lyamani, H., Olmo, F.J., Alados-Arboledas, L., 2011. Improvements in star photometry for aerosol characterizations. Journal of Aerosol Science 42, 737–745. doi:10.1016/j.jaerosci.2011.06.010.

[11] Roddier, F., 1981. The Effects of Atmospheric Turbulence in Optical Astronomy, in: Progress in Optics. Elsevier. chapter V, pp. 281–376. doi:10.1016/S0079-6638(08)70204-X.

[12] Rufener, F., 1964. Technique et réduction des mesures dans un nouveau système de photométrie stellaire. Publications de l'Observatoire de Genève, Série A: Astronomie, chronométrie, géophysique 66, 413–464. URL: http://www.worldcat.org/oclc/491819702.

[13] Rufener, F., 1986. The evolution of atmospheric extinction at La Silla. Astronomy and Astrophysics 165, 275–286. URL: http://adsabs.harvard.edu/abs/1986A&A...165..275R.

[14] Young, A.T., 1974. Observational Technique and Data Reduction, in: Methods in Experimental Physics. Elsevier. volume 12. chapter 3, pp. 123–192. doi:10.1016/S0076-695X(08)60495-0.

[15] Young, A.T., Irvine, W.M., 1967. Multicolor photoelectric photometry of the brighter planets. I. Program and Procedure. Astronomical Journal 72, 945. doi:10.1086/110366.

Bibliography

[1] G. A. Alekseeva, "The determination of atmospheric extinction by the stellar magnitude differences method in stellar spectrophotometry," *Izvestiya Glavnoj Astronomicheskoj Observatorii v Pulkove*, vol. 198, pp. 18–21, 1980. Disponible à http://adsabs.harvard.edu/abs/1980IzPul.198...18A

[2] R. C. Bohlin, K. D. Gordon, et P.-E. Tremblay, "Techniques and Review of Absolute Flux Calibration from the Ultraviolet to the Mid-Infrared," *Publications of the Astronomical Society of the Pacific*, vol. 126, no. 942, pp. 711–732, jul 2014.

[3] K. Baibakov, N. T. O'Neill, L. Ivănescu, T. J. Duck, C. Perro, A. Herber, K.-H. Schulz, et O. Schrems, "Synchronous starphotometry and lidar measurements at Eureka in High Canadian Arctic," *Atmos. Meas. Tech. Discuss.*, vol. 8, no. 2, pp. 2013–2065, feb 2015.

[4] A. Barreto, R. Román, E. Cuevas, D. Pérez-Ramírez, A. Berjón, N. Kouremeti, S. Kazadzis, J. Gröbner, M. Mazzola, C. Toledano, J. Benavent-Oltra, L. Doppler, J. Juryšek, A. Almansa, S. Victori, F. Maupin, C. Guirado-Fuentes, R. González, V. Vitale, P. Goloub, L. Blarel, L. Alados-Arboledas, E. Woolliams, S. Taylor, J. Antuña, et M. Yela, "Evaluation of night-time aerosols measurements and lunar irradiance models in the frame of the first multi-instrument nocturnal intercomparison campaign," *Atmospheric Environment*, vol. 202, pp. 190–211, apr 2019.

[5] S. Deustua, S. Kent, et J. A. Smith, "Absolute Calibration of Astronomical Flux Standards," dans *Planets, Stars and Stellar Systems*. Dordrecht: Springer Netherlands, 2013, pp. 375–402.

[6] D. M. Giles, A. Sinyuk, M. G. Sorokin, J. S. Schafer, A. Smirnov, I. Slutsker, T. F. Eck, B. N. Holben, J. R. Lewis, J. R. Campbell, E. J. Welton, S. V. Korkin, et A. I. Lyapustin, "Advancements in the Aerosol Robotic Network (AERONET) Version 3 database – automated near-real-time quality control algorithm with improved cloud screening for Sun photometer aerosol optical depth (AOD) measurements," *Atmospheric Measurement Techniques*, vol. 12, no. 1, pp. 169–209, jan 2019.

[7] F. Hemmer, L. C.-Labonnote, F. Parol, G. Brogniez, B. Damiri, et T. Podvin, "An algorithm to retrieve ice water content profiles in cirrus clouds from the synergy of ground-based lidar and thermal infrared radiometer measurements," *Atmospheric Measurement Techniques*, vol. 12, no. 3, pp. 1545–1568, mar 2019. Disponible à https://www.atmos-meas-tech.net/12/1545/2019/

[8] L. Ivănescu, "Une application de la photométrie stellaire à l'observation de nuages optiquement minces à Eureka, NU," Master in Science thesis, UQAM, 2015. Disponible à www.archipel.uqam.ca/id/eprint/8417

[9] Q. Libois, L. Ivănescu, J.-P. Blanchet, H. Schulz, H. Bozem, W. R. Leaitch, J. Burkart, J. P. D. Abbatt, A. B. Herber, A. A. Aliabadi, et É. Girard, "Airborne observations of far-infrared upwelling radiance in the Arctic," *Atmospheric Chemistry and Physics*, vol. 16, no. 24, pp. 15 689–15 707, 2016.

[10] Q. Libois, C. Proulx, L. Ivănescu, L. Coursol, L. S. Pelletier, Y. Bouzid, F. Barbero, É. Girard, et J.-P. Blanchet, "A microbolometer-based far infrared radiometer to study thin ice clouds in the Arctic," *Atmospheric Measurement Techniques*, vol. 9, no. 4, pp. 1817–1832, apr 2016. Disponible à http://www.atmos-meas-tech.net/9/1817/2016/

[11] Z. Liu, M. Vaughan, D. Winker, C. Kittaka, B. Getzewich, R. Kuehn, A. Omar, K. Powell, C. Trepte, et C. Hostetler, "The CALIPSO Lidar Cloud and Aerosol Discrimination: Version 2 Algorithm and Initial Assessment of Performance," *Journal of Atmospheric and Oceanic Technology*, vol. 26, no. 7, pp. 1198–1213, jul 2009. Disponible à http://dx.doi.org/10.1175/2009JTECHA1229.1

[12] Q. Min et M. Duan, "Simultaneously retrieving cloud optical depth and effective radius for optically thin clouds," *Journal of Geophysical*

Research, vol. 110, no. D21, p. D21201, 2005. Disponible à http://doi.wiley.com/10.1029/2005JD006136

[13] N. T. O'Neill, K. Baibakov, S. Hesaraki, L. Ivănescu, R. V. Martin, C. Perro, J. P. Chaubey, A. Herber, et T. J. Duck, "Temporal and spectral cloud screening of polar winter aerosol optical depth (AOD): impact of homogeneous and inhomogeneous clouds and crystal layers on climatological-scale AODs," *Atmospheric Chemistry and Physics*, vol. 16, no. 19, pp. 12 753–12 765, oct 2016.

[14] N. T. O'Neill, O. Dubovik, et T. F. Eck, "Modified Ångström exponent for the characterization of submicrometer aerosols," *Applied Optics*, vol. 40, no. 15, pp. 2368–2375, 2001.

[15] D. Pérez-Ramírez, J. Aceituno, B. Ruiz, F. J. Olmo, et L. Alados-Arboledas, "Development and calibration of a star photometer to measure the aerosol optical depth: Smoke observations at a high mountain site," *Atmospheric Environment*, vol. 42, no. 11, pp. 2733–2738, apr 2008.

[16] D. Pérez-Ramírez, B. Ruiz, J. Aceituno, F. J. Olmo, et L. Alados-Arboledas, "Application of Sun/star photometry to derive the aerosol optical depth," *International Journal of Remote Sensing*, vol. 29, no. 17-18, pp. 5113–5132, sep 2008.

[17] F. Roddier, "The Effects of Atmospheric Turbulence in Optical Astronomy," dans *Progress in Optics*. Elsevier, 1981, ch. V, pp. 281–376.

[18] A. Sinyuk, B. N. Holben, A. Smirnov, T. F. Eck, I. Slutsker, J. S. Schafer, D. M. Giles, et M. Sorokin, "Assessment of error in aerosol optical depth measured by AERONET due to aerosol forward scattering," *Geophysical Research Letters*, vol. 39, no. 23, dec 2012. Disponible à https://doi.org/10.1029/2012GL053894

[19] A. T. Young, "Observational Technique and Data Reduction," dans *Methods in Experimental Physics*. Elsevier, 1974, vol. 12, ch. 3, pp. 123–192.